

Thermo-Mechanical Studies for the Experimental Investigation of Cryogenic Mirror Suspensions for Third Generation Gravitational- Wave Detectors

Master's Thesis of

Enes Turkic

Department of Chemical and Process Engineering Karlsruhe Institute of
Technology (KIT)
Institute of Technical Thermodynamics and Refrigeration, Organizational
Unit: ITTK-KKT

Reviewer: Prof. Dr.-Ing. Steffen Grohmann
Second reviewer: Prof. Dr.-Ing. Thomas Meurer
Supervisor: Xhesika Koroveshi M.Sc.

15. April 2024 – 21. October 2024

Karlsruher Institut für Technologie
Fakultät für Chemieingenieurwesen und Verfahrenstechnik
Postfach 6980
76128 Karlsruhe

Master thesis

for Mr. B.Sc. Enes Turkic

THERMO-MECHANICAL STUDIES FOR THE EXPERIMENTAL
INVESTIGATION OF CRYOGENIC MIRROR SUSPENSIONS FOR THIRD
GENERATION GRAVITATIONAL-WAVE DETECTORS

THERMO-MECHANISCHE STUDIEN ZUR EXPERIMENTELLEN
UNTERSUCHUNG KRYOGENER SPIEGELAUFHÄNGUNGEN FÜR
GRAVITATIONSWELLENDTEKTOREN DER DRITTEN GENERATION

Background:

The Einstein Telescope (ET) is the third-generation gravitational-wave detector planned in Europe. Its low-frequency interferometer requires cryogenic operation of the core optics to suppress the suspension thermal noise (STN) that limits the sensitivity at 3 Hz to 10 Hz. The baseline design of the so-called payload includes both mono-crystalline suspension fibers and a novel concept developed at [TTK-KKT](#), where cryogenic cooling is provided via a thin-wall suspension tube filled with superfluid helium (He-II). The suspensions are crucial parts of the overall payload structure, affecting the achievement of the extremely challenging sensitivity goals. Its modeling and design requires experimental data on loss mechanisms in full-scale cryogenic mirror suspensions. For this purpose, the new test facility GRAVITHELIUM is being planned.

The loss mechanisms in suspensions are determined by measurement of the quality factor Q , where exponential decay amplitudes are analyzed after the samples have been excited to resonance. The experiments are planned in a temperature range from 300 K down to 2 K. Within this thesis, mechanical dynamic analyses shall be carried out on the samples and the cryostat internal structures, in order to advance the mechanical cryostat design.

Scope of work:

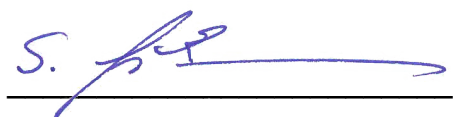
The Master's thesis shall include the following main work packages:

- Familiarization with the experimental concept and the conceptual design
- Literature study on numerical modeling of dynamic analyses for the application
- Set-up of a test model and verification with existing modeling results
- Integration of geometries and material data in the required temperature range
- Dynamic analyses of the samples, the sample support and the surrounding geometries in the cryostat, including design optimization

The Master's thesis shall be conducted at TTK-KKT. It shall be written in English language. The results shall be presented in the ITTK Institute seminar at KIT. The rules for safeguarding good scientific practice at KIT shall be applied.

Start of work: 15.04.2024

Supervisor: M.Sc. Xhesika Korovesi



Prof. Dr.-Ing. Steffen Grohmann

I declare that I have developed and written the enclosed thesis completely by myself, and have not used sources or means without declaration in the text.

Karlsruhe, 21.10.2024

.....
(Enes Turkic)

Contents

Symbol and Abbreviations List	iii
1 Introduction	1
2 Theoretical Background	5
2.1 Physical Solid Properties and Temperature Dependency	5
2.2 Energy Dissipation in Vibrating Systems	8
2.3 Analytical Analysis	10
2.4 Numerical Analysis	13
2.5 Vibrating Signals	15
2.5.1 Frequency Response Analysis	16
2.5.2 Random Vibration Analysis	17
3 Setup and Boundary Conditions	19
3.1 Design Limitations	21
3.2 Sample Analysis	22
3.2.1 FEM implementation of Sample	23
3.2.2 Modal Analysis	27
3.2.3 Frequency Response	29
4 Sample Support Structure Design Phase-I	31
4.1 Setup Design for Unloaded Samples	31
4.1.1 General Boundary Condition	33
4.1.2 Dimensioning of Sample Support System	33
4.1.3 Modal Analysis	37
4.1.4 Frequency Response Analysis	39
4.1.5 Energetic Evaluation	41
4.1.6 Improving Extrinsic Loss Angle for Low Frequency Measurements	47
4.2 Setup Design for Loaded Sample Case	49
5 Adaption of an Existing Setup Design	55
5.1 Geometry Adaption	55
5.2 Modal Analysis and Frequency Response Analysis	58
5.3 Energetic Evaluation and Loss estimation	60
5.3.1 Comparison of Adapted and GRAVITHELIUM Sample Support Structures	62
6 Sample Support Structure Design Phase-II	63
6.1 Modal analysis and Frequency Response Analysis	66

6.2	Energetic Evaluation and Loss Estimation	68
7	Impact of Cryocooler Vibration on the Test Setup Design	71
8	Conclusion and Outlook	77
	Bibliography	81
A	Appendix	91
A.1	Appendix equations	91
A.2	Additional Tables	91
A.3	Additional figures	97

Symbol and Abbreviations List

Greek Symbol List

α	Linear expansion coefficient
$\hat{\beta}$	Basis function
β	Thermal elastic coefficient
Δ	Difference
ϵ	Normalised change in length
θ	Angle
λ	Thermal conductivity
ρ	Density
Σ	Sum
σ	Tension
σ_y	Yield strength
σ_u	Ultimate strength
τ_{decay}	Decay time
τ_{therm}	Thermal diffusion time
Φ	Phase angle
ϕ	loss angle
$\hat{\phi}$	Strain weighted loss angle
ψ	Displacement function
ω	Angular frequency

Latin Symbol List

A	Surface area
\hat{A}	Amplitude
c_p	Specific heat capacity
d	Diameter
D	Dilution factor
E	Young's modulus
f	Frequency
F	Force
g	Gravitational acceleration
h	Height
I	Area moment of inertia
k	Spring constant
l	Length
m	Mass
p	Load
Q	Quality factor
s	Wall thickness
∇	Laplace operator
S_{xx}	Power spectral density
SF	Safety factor
t	Time
T	Temperature
U	Integral strain
\hat{U}	Displacement
u	Strain density
V	Voltage
x	Displacement response

Abbreviation List

BC	Boundary condition
ET	Einstein Telescope
FC	Fixed constraint
FEM	Finite Element Method
FRA	Frequency response analysis
H	Head
HF	High frequency
HT	Helium tube
HV	Head variant
IT	Inner tube
LB	Lower block
LF	Low frequency
MA	Modal analysis
OT	Outer tube
PDE	Partial differential equation
PSD	Power spectral density
PT	Pulse tube
RI	Return interface
RMS	Root mean square value
SA	Sample
SH	Sample holder
SHS	Sample holder suspension
SI	Supply interface
SSS	Sample support structure
SUS	Sample support system
UB	Upper block
VA	Vibration attenuator

1 Introduction

In 1916 Albert Einstein predicted the existence of gravitational waves (GW) [1]. These ripples in space are caused by movements of large masses in space [2]. Since the first prediction of GW, the aim existed to develop a measurement system, capable of measuring GW. LASER interferometers of the first generation LIGO and Virgo have been developed which were theoretically sensible enough to measure GW [3]. Updating the existing LASER interferometers, have improved the sensitivity to about ca. 100 Hz. In 2015 the second generation of LASER interferometers LIGO and Virgo successfully detected GW for the first time [2].

The Einstein Telescope (ET) is a third generation GW detector, which is currently undergoing research and development [4]. ET combines a high frequency (HF) and low frequency (LF) LASER interferometer. Where the sensitivity ranges are 30 Hz to 10 kHz for ET-HF and 3 Hz to 30 Hz for ET-LF [5]. To reach the sensitivity requirements of ET-LF, the thermal noise introduced by the Brownian motion of the ET-LF payload needs to be minimised. This is accomplished by operating the mirrors at cryogenic temperatures, in the range of 10 K to 20 K [4].

The sensitivity within the ET-LF in the frequency range below 10 Hz is limited by the suspension thermal noise, therefore the cryogenic operation of the system indispensable [6]. The use of suspension material which has low dissipation characteristics have to be used. Additionally these suspensions have to have a high thermal conductivity at the target temperatures. A baseline design for the cryogenic ET-LF payload has been conducted in [6]. The designs include two possible concepts in [6]. One concept is based on the use of monolithic silicon or sapphire suspension and the other concept involves the use of a titanium suspension tube, filled with super fluid helium (He-II) [6]. The mechanical dissipation properties of the monolithic suspensions cannot be modelled sufficiently, to the required sensitivity and thus have to be measured. Furthermore the mechanical dissipation properties of He-II are unknown and therefore require intricate measurement as well [7]. A conceptual design of a cryostat called GRAVITHELIUM has been presented in [7]. GRAVITHELIUM enables the investigation of full scale monolithic suspension and suspension tubes. The conceptual design of the GRAVITHELIUM cryostat is presented in figure 1.1.

The cryostat dimensions include a stainless steel vacuum vessel, with a diameter of 1.5 m and a height of 3 m [7]. The internal components are cooled via a pulse tube cryocooler [7]. A radiation shield is connected to the cryocooler first stage. To the colder second stage of the cryocooler, a helium tight test chamber is connected, which serves as a second radiation shield [7]. The test chamber has a diameter of 1.2 m and a height of 2 m. This allows for the measurement of full scale suspensions deployed in the ET-LF payload. The marionette suspensions have a length of 1 m and the mirror suspensions have a length of

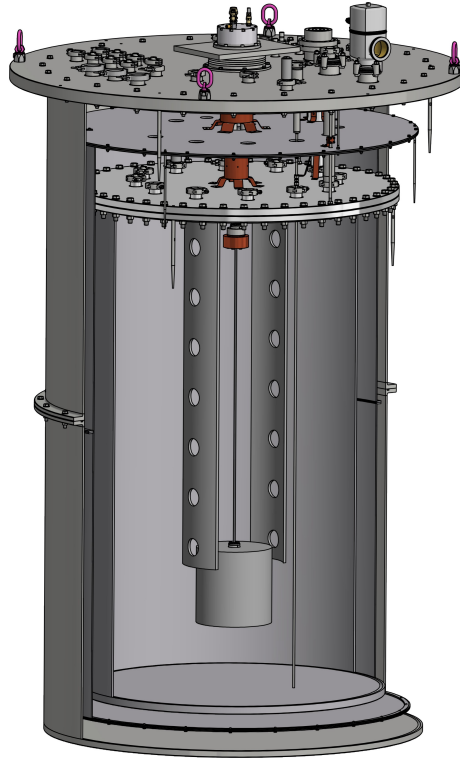


Figure 1.1: Conceptual design of the GRAVITHELIUM cryostat for the first experimental campaign, with a sample under mechanical load courtesy of X. Korovesi

1.2 m [6, 7]. The helium tight test chamber allows the setup to be cooled via helium as a contact gas.

The measurements will be conducted in two separate measurement campaigns. The first phase involves the investigation of mechanical dissipation of monolithic suspension fibres and empty suspension tubes in a temperature range of 3 K to 300 K. These experiments will be conducted with and without mechanical loads applied to the investigated suspension [7]. The second involves the investigation of mechanical dissipation of He-II filled suspension tubes in a temperature range below 2.17 K. With a He-supply system introduced, providing the He-II to the suspension tubes. This system is mechanically isolated from the measurement cryostat.

The mechanical dissipation is a characteristic of a system. Hence the system supporting the investigated suspensions has to be designed in way to not be a limiting factor to the low mechanical dissipation properties of the suspensions [7, 8, 9, 10].

In the scope of this work a generalised design approach has been developed, implemented as finite element method tool, which allows for the investigation of complex geometries. The developed generalised design approach, to the sample support structure capable of conducting dissipation measurements, includes the definition of key parameters which can be adjusted and resulting parameters can be assessed. The outline of the general design approach is a modal analysis of the sample types, which conclude the relevant natural frequencies for the dissipation measurements. A design of a sample support system is

designed. Based on previous designs, which have been published in literature, certain aspects of existing sample support structures have been taken into account and were adjusted to be suitable for the investigated suspension fibres in GRAVITHELIUM. The system is adapted to support the various sample types included in this work. And a subsequent estimation on the dissipative behaviour of the sample support structure is modelled. With this systematised approach, it can be validated, that the sample support structure does not limit the dissipation mechanism of the suspension under investigation.

2 Theoretical Background

In this section the theoretical groundwork to model and understand the physical relations of pendulum and continuous systems is presented. Furthermore numerical approaches to model the presented system and their analytical counterparts are presented to both model and validate their results.

2.1 Physical Solid Properties and Temperature Dependency

Mechanical properties of materials depend to varying degrees on the temperature which have to be assessed before dimensioning the components experiencing cryogenic temperatures [11]. The figure 2.1 shows a typical stress strain curve for an arbitrary ductile material which is typically measured applying a tensile force [11]. Stress σ is defined as the axial force F normalised to the cross sectional area A [11]:

$$\sigma = F/A \quad (2.1)$$

Strain ϵ is defined as the change in length ΔL normalised to the initial length L [11]

$$\epsilon = \Delta L/L \quad (2.2)$$

Multiple relevant material properties can be deduced from the stress strain relation used to dimension mechanical components. The linear region in figure 2.1 is the so called *elastic*

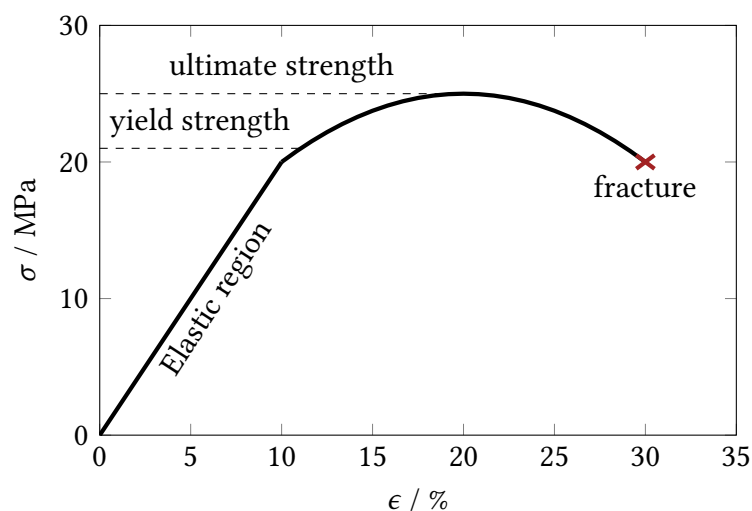


Figure 2.1: Arbitrary stress strain curve, based on [11]

region meaning the deformation goes back to its origin after releasing the tensile force. Further applying the tensile force causes plastic deformation. The transition between elastic and plastic regime is not a specified point but rather a zone. Hence the *yield strength* σ_y is typically given as the stress at which the remaining permanent plastic deformation is 0.2 % after realising the tensile force. Further applying tensile force leads the material to its *ultimate strength* σ_u . After which necking, meaning the cross sectional area decreases and subsequently fracture occur [11]. For brittle materials such as sapphire and silicon relevant to this work σ_y and σ_u are approximately the same value.

The *slope* of the elastic region yields the *Young's modulus* E :

$$\sigma = E\epsilon \quad (2.3)$$

The Young's modulus is determined by the forces between atoms in a crystal lattice [12]. As these forces vary mildly with respect to temperature in solids, the Young's modulus increasing mildly towards the higher values at lower temperatures. This effect can be seen in the figure 2.2.

Figure 2.2 shows the behaviour of the Young's modulus for titanium [11] and for monolithic silicon in the crystallographic $\langle 100 \rangle$ direction [12]. Monocrystalline materials such as silicon and sapphire are anisotropic, meaning material properties such as the Young's modulus, are dependent on the orientation of the crystallographic plane. Thus the Young's modulus is expressed as a fourth order tensor [14] and the stress strain relation ship is expressed as shown in eq. 2.4 [14].

$$\sigma_{ij} = E_{ijkl}\epsilon_{kl} \quad (2.4)$$

Due to the symmetry of silicon cubic crystal of the elasticity tensor reduces to [14]

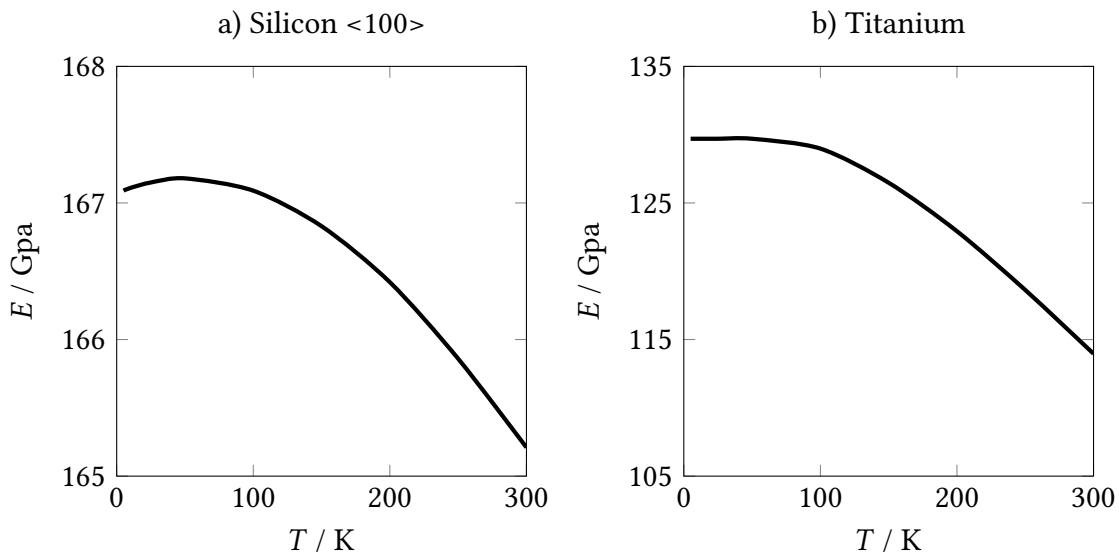


Figure 2.2: Temperature dependency of $\langle \text{Si}100 \rangle$ [12] and Titanium [13]

$$E_{ijkl} = \begin{matrix} C_{11} & C_{12} & C_{12} & 0 & 0 & 0 \\ C_{12} & C_{11} & C_{12} & 0 & 0 & 0 \\ C_{12} & C_{12} & C_{11} & 0 & 0 & 0 \\ 0 & 0 & 0 & C_{44} & 0 & 0 \\ 0 & 0 & 0 & 0 & C_{44} & 0 \\ 0 & 0 & 0 & 0 & 0 & C_{44} \end{matrix} \quad (2.5)$$

The components within matrix C_{ij} are called elasticity coefficients which are dependant on temperature but not on orientation of the crystal. Due to the crystal being symmetrical and cubic the elasticity matrix is fully described by the three temperature dependent elasticity coefficients C_{11} , C_{12} and C_{44} . The temperature dependant elasticity coefficients for silicon are given by [15]. For sapphire which has a symmetric hexagonal crystal structure the elasticity matrix is shown eq. A.2 and the elasticity coefficients are given by [13].

As seen in figure 2.1 applying a tensile force beyond the elastic limit of a material leads to plastic deformation. As plastic deformation is typically unwanted in a system, the yield strength σ_y is used as a physical limitation, dimension components. The yield strength is dependent on both the material deployed and additionally the manufacturing method (eg. if the material was annealed, alloyed, hardened etc.) [11]. The yield strength generally increases at lower temperatures [11]. To dimension the diameter d of a circular suspension, to which a mechanical load is applied the equation is given by:

$$d = SF \sqrt{\frac{4mg}{\sigma_y \pi}} \quad (2.6)$$

As σ_y is temperature dependent, the components are dimensioned for the temperature at which σ_y is at its minimum. In order to provide a conservative engineering design of the system, a safety factor of $SF = 3$ is applied [6].

The table below shows explicit values for E , σ_y and density ρ at 300 K and 20 K for selected materials relevant to this work. It can be seen that the Young's modulus varies $\sim 10\%$ within the temperature span increasing at lower temperatures for all materials. Whereas it can be seen that the temperature dependency of σ_y depends strongly on the material deployed.

Table 2.1: Young's modulus, yield strength and density of sample material.

Quantity	Silicon		Sapphire		Titanium	
	300 K	3 K	300 K	3 K	300 K	3 K
E / GPa	127 [12]	130 [12]	460[16]	506 [16]	115 [11]	127[11]
σ_y / MPa	200 [17]	230 [17]	360 [16]	400 [16]	400 [11]	1200 [11]
ρ / kgm^{-3}	2330 [6]		3980[6]		4540[6]	

2.2 Energy Dissipation in Vibrating Systems

In order to account for damping in a vibrating system, the Young's modulus can be regarded as a complex quantity by introducing an imaginary restoring property [18]. The ratio between real and imaginary part of E is called the loss angle ϕ [18]. The Young's modulus can be expressed as [19]:

$$E = E_0[1 + i\phi(f)] \quad (2.7)$$

Where E_0 is the materials Young's modulus, i is the complex unit and f is the frequency. Each material is associated with its loss angle. The vibration characteristics of a system is characterised by a single loss angle ϕ_{system} [19]. Thus a multiple of factors influence the loss angle of a system, which can be categorised as *intrinsic* and *extrinsic* factors. Intrinsic factors are mostly dependent on material and geometry, whilst extrinsic factors depend on the external factors. These factors are summed and form the total loss angle ϕ_{system} . For a suspension system, which are discussed in the scope of this work, ϕ_{system} is given as [7]:

$$\phi_{\text{system}}(f) = \phi_{\text{bulk}} + \phi_{\text{thermoelastic}} + \phi_{\text{surface}} + \phi_{\text{extrinsic}} \quad (2.8)$$

Where ϕ_{bulk} are losses associated with the bulk material. These losses are mainly dependent on the structural composition and defects in the material lattice, as well as temperature [18]. The thermoelastic losses $\phi_{\text{thermoelastic}}$ arise from local temperature gradients due to local compression and expansion in the material, inducing a heat flux associated with entropy production [20]. The thermoelastic loss can be calculated by:

$$\phi_{\text{thermoelastic}} = \frac{ET}{\rho c_p} \left(\alpha - \sigma \frac{\beta}{E} \right)^2 \left(\frac{2\pi f \tau}{1 + (2\pi f)^2} \right) \quad (2.9)$$

where α is the linear expansion coefficient, β is the thermal elastic coefficient, c_p is the specific heat capacity and τ_{therm} is the thermal diffusion time and is given as:

$$\tau_{\text{therm}} = \frac{d^2 \rho c_p}{13.55 \lambda} \quad (2.10)$$

for circular suspension, where λ is the thermal conductivity of the suspension material [21]. The surface losses ϕ_{surface} are associated with energy dissipation, mainly attributed to the surface quality of the material [9]. The extrinsic losses $\phi_{\text{extrinsic}}$ for suspensions are mainly associated with the energy dissipation, due to the system in which they are suspended, e.g. stress due to a suspended mass, clamping or recoil. The extrinsic losses, bulk and surface losses cannot be modelled. However the loss angle of the system ϕ_{system} , can be defined via a measurement of the so called *Quality factor*. The Q -factor is defined as the inverse of the loss angle at resonance frequency f_0 of vibrating systems [22].

$$Q = \phi(f_0)^{-1} \quad (2.11)$$

For suspension in GW applications the $\phi_{\text{suspension}}$ is typically assumed, to not be dependent on frequency, within the sensitivity bandwidth of the GW-detector [23]. However it is highly dependent on temperature [24].

Table 2.2: Q -factors for silicon, sapphire and Titanium at two different temperatures

	silicon	sapphire	Titanium
$Q(300\text{ K})$	1×10^5 [25]	5×10^4 [8]	2×10^1 [26]
$Q(3\text{ K})$	1×10^8 [9]	1×10^8 [6]	1×10^6 [26]

Measuring the Q -factor is conducted by actuating the suspension at its resonance frequency, by a sinusoidal force [22]. Once the suspension reaches a sufficiently large starting amplitude a_0 the actuating is stopped and the suspension continues to vibrate on its own. The sum of $\phi_{\text{intrinsic}}$ and $\phi_{\text{extrinsic}}$ will cause the amplitude of the vibration to decrease and an exponential *ring down* of the free decaying amplitude $a(t)$ over time t is detected[24]

$$a(t) = a_0 e^{-\frac{t}{\tau_{\text{decay}}}} \quad (2.12)$$

Once the measured amplitude reaches $\frac{a_0}{e}$ the value of the decay time τ_{decay} can be determined and used to calculate the Q -factor. [24].

$$Q = \pi f_0 \tau_{\text{decay}} \quad (2.13)$$

From eq. 2.13 the temperature dependency is given via the temperature dependency of the natural frequency and decay time τ_{decay} .

The table 2.2 shows typically measured Q -factors for suspensions considered in GW-detector applications.

From table 2.2 the general trend of the Q factor rising at lower temperatures can be seen. Furthermore all the above listed material are known as high Q -factor materials, having low intrinsic dissipation properties. Hence designing a system capable of measuring intrinsic low dissipative behaviour, has to be conducted with minimising the extrinsic dissipation $\phi_{\text{extrinsic}}$.

As described above the extrinsic contribution of the loss angle cannot be modelled. Therefore a method is defined, with which the total systems energy dissipation can be estimated. For the Q - measurements the the suspension is vibrating freely at its natural frequency. The deformation of the suspension causes elastic energy within the material, which is also called strain energy. The strain energy density is denoted by u [J/m³][23]. Energy dissipation is assumed to occur at maximal deflection. At the maximal deflection of the suspension, the strain density becomes maximal and is denoted as u_{max} . Integrating u_{max} and the loss angle of the suspension yields the dissipated energy per unit time W_{diss} [23]:

$$W_{\text{diss}} = 2\pi f U_{\text{suspension}} \phi_{\text{suspension}(f)} = 2\pi f \int u_{\text{max}}(r, f) \phi(r, f) d^3 r \quad (2.14)$$

Eq. 2.14 shows the energy dissipation is dependent on the integral strain $U_{\text{suspension}}$ of the suspension and the integral loss angle of the suspension $\phi_{\text{suspension}}$. Eq. 2.14 can be formulated for each component of an assembly. By integrating $u_{\text{max},j}$ of each component yields U_j and integrating the the strain density of the entire system $u_{\text{max,system}}$ over the entire system yields U_{system} . The energetic contribution of each component to the total

strain energy is the integral strain ratio which is defined as: U_j/U_{system} . Multiplying the integral strain ratio to the anticipated loss angle, defines the strain weighted loss angle. The system loss angle ϕ_{system} can be calculated by summation of strain weighted loss angles of each component shown in eq. 2.15 [17, 8, 27].

$$\phi_{\text{system}} = \sum_j \phi_j \frac{U_j}{U_{\text{system}}} = \phi_{\text{suspension}} \frac{U_{\text{suspension}}}{U_{\text{system}}} + \phi_{\text{clamping}} \frac{U_{\text{clamping}}}{U_{\text{system}}} + \dots \quad (2.15)$$

Where j represents a component of the assembly. As a consequence of Q relating to the energy dissipation of a suspension. Eq. 2.15 the strain weighted loss angle is to be optimised in an assembly, when measuring energy dissipation mechanisms of low dissipative materials. As certain loss angle contributions cannot be modeled beforehand, such as surface losses or bulk losses, the values for ϕ_j , have to be taken from literature.

2.3 Analytical Analysis

Pendulum systems are characterised by a mass suspended from a fixed point oscillating due to the effect of gravity or other forces. To analytically calculate the natural frequency of pendulum systems, the elasticity of the suspension can be assumed to have no effect and the suspended mass being assumed a point mass. The natural frequency can be then calculated by applying Newton's laws governing the equation of motion of a simple pendulum, given by [28]:

$$\ddot{\theta} + (g/L)\sin(\theta) = 0 \quad (2.16)$$

where θ is the angular displacement, g is the gravitational acceleration and L is the length of the pendulum.

For small angular displacements the small angle approximation $\sin(\theta) \approx \theta$ can be applied [28]. The natural frequency f can then be calculated by the following equation.

$$f = \frac{1}{2\pi} \sqrt{g/L} \quad (2.17)$$

Accounting for elasticity of the suspension and moment of inertia of the suspended mass, the system cannot be analytically described as shown in [29]. The mathematical equations for a pendulum system then becomes an elaborate differential equation, with multiple resulting natural frequencies as shown in [29]. Figure 2.3 shows the existing characteristic mode shapes for a pendulum system as defined in [29].

Figure 2.3 shows the mode shapes occurring in pendulum systems when elasticity and moment of inertia are regarded and presents their nomenclature used in this work. Notably the pendulum mode depicted is the mode calculated by eq. 2.17 all other modes occur due to the moment of inertia and elasticity of the suspension [29]. As presented in [19] the energy of a vibrating pendulum is split in a elastic energy, which is associated with losses and a potential energy, which is not associated with losses [19]. The elastic energy E_{elastic} due to the deformation in the pendulum suspension is given by

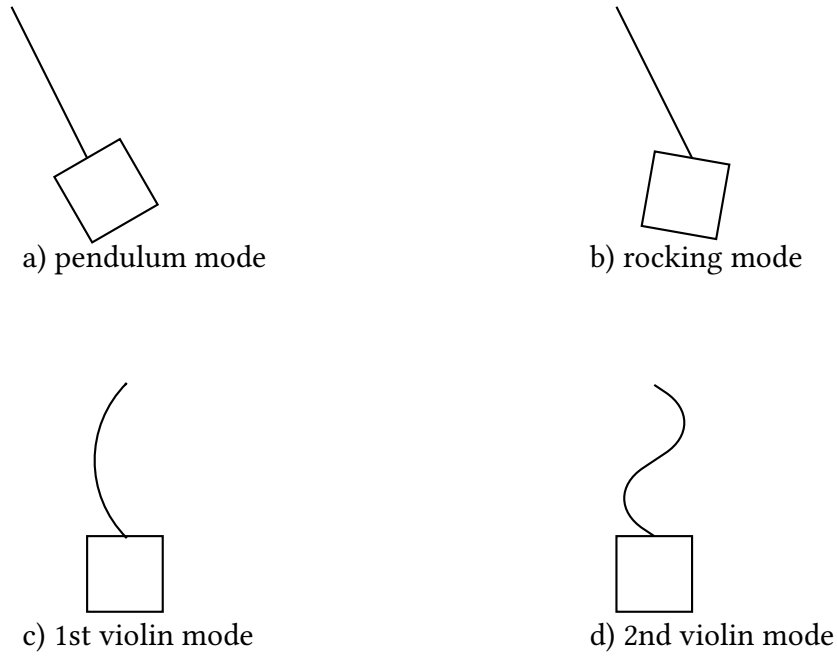


Figure 2.3: Pendulum system mode shapes adapted from [29]

$$E_{\text{elastic}} = \frac{1}{2} \left(\frac{mg}{2L} \sqrt{\frac{EI}{mgL^2}} \right) u^2 \quad (2.18)$$

Where m is the suspended mass, E represents the Young's modulus and I is the moment of inertia of the suspension. The potential energy E_{pot} for a pendulum system is given by [19]

$$E_{\text{pot}} = \frac{1}{2} \frac{mg}{L} u^2 \quad (2.19)$$

The ratio between the potential and elastic energy is represented in the *dilution factor* D [19]. For a cylindrical cross section for the suspension the dilution factor is given by

$$D = \frac{E_{\text{el}}}{E_{\text{pot}}} = \frac{d^2}{16L} \sqrt{\frac{E\pi}{mg}} \quad (2.20)$$

Where d represents the diameter of the suspension, L is the suspension length, E being the Young's modulus of the suspension material, m representing the suspended mass and g being the gravitational acceleration.

Using the dilution factor the loss angle of a pendulum system can be calculated as presented in [6] as

$$\phi_{\text{pend}} = \phi_{\text{suspension}} D \quad (2.21)$$

The dissipative behaviour of a suspension is therefore reduced when configured as a pendulum system. Thus the dilution factor serves as an estimation tool for a loss amplitude of a pendulum system. A dilution factor of $D \ll 1$ suggests the majority of the systems

energy is stored as lossless potential energy, meaning the resulting loss of a suspension system can be greatly lowered when designed as a pendulum system [19].

Analytically describing the vibration behaviour of beams contrasts the method of analytically describing pendulum systems. In order to analytically evaluate the natural frequencies and mode shapes of continuous media, such as beams, the Bernoulli Euler beam theory can be ascribed to vibrating structures [30].

Using the associated sets of assumptions of the Euler-Bernoulli beam theory yields the differential equation of motion [30]:

$$\frac{\partial^4 \hat{U}(x)}{\partial x^4} - \omega^2 \frac{\rho A}{EI} \hat{U}(x) = p \quad (2.22)$$

Where E represents the Young's modulus, I represents the area moment of inertia, \hat{U} represents the transversal displacement of the beam, ω is the angular frequency, ρ is the material density, A represents the cross sectional surface area and p represents the load applied to the beam.

As there is no load applied when calculating the natural frequencies and mode shapes $p = 0$, yielding an ordinary fourth order differential equation which can be solved by a characteristic function with the eigenvalue λ [30]. Solving the characteristic equation yields the eigenvalue with which in turn the natural frequency can be determined by:

$$\omega = \lambda^2 \sqrt{\frac{\rho A}{EI}} \quad (2.23)$$

In order to determine the characteristic function describing the motion of the beam the appropriate boundary conditions (BC) for the beams need to be applied to the following equation which can be derived from eq. 2.22 as shown in [30]:

$$\hat{U}(x) = D_1 \exp -\lambda(L - x) + D_2 \exp -\lambda x + D_3 \cos(\lambda x) + D_4 \cos(\lambda x) \quad (2.24)$$

As there are multiple options to physically support the beam at the ends x_e possible BC are [30]:

- *Free-end* where transversely shear and the bending moments vanish

$$\frac{\partial^2 \hat{U}(x_e)}{\partial x} = 0; \frac{\partial^4 \hat{U}(x_e)}{\partial x} = 0 \quad (2.25)$$

- *Simple-end* where displacement and bending moment vanish

$$\hat{U}(x_e) = 0; \frac{\partial^2 \hat{U}(x_e)}{\partial x} = 0 \quad (2.26)$$

- *Fixed-end* where the displacement and its spatial variant vanish

$$\hat{U}(x_e) = 0; \frac{\partial \hat{U}(x_e)}{\partial x} = 0 \quad (2.27)$$

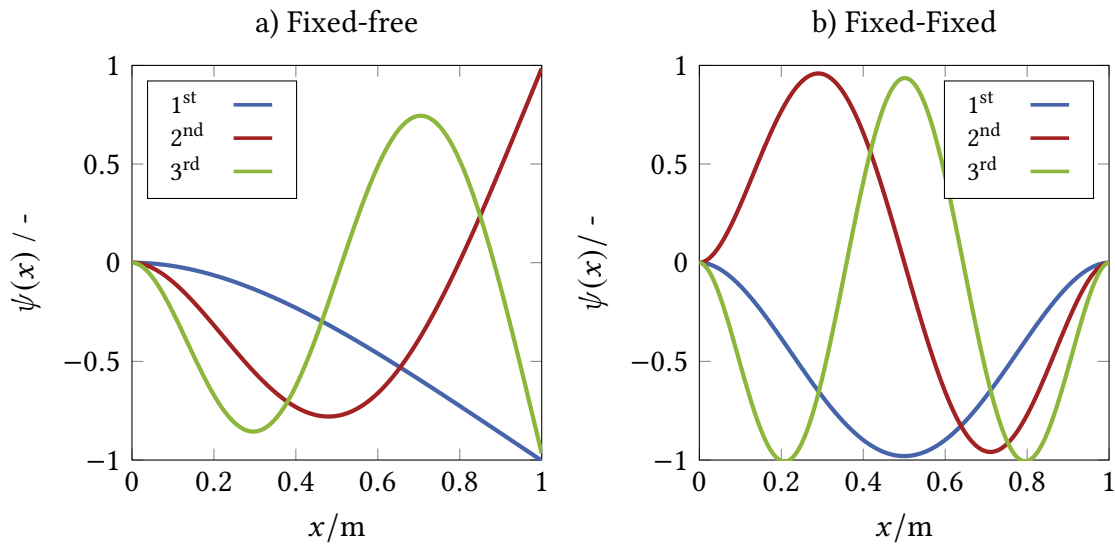


Figure 2.4: Beam mode shapes for arbitrary frequencies and lengths for both boundary condition cases

Two of these BCs are relevant in this work. Namely the fixed-free boundary conditions and fixed-fixed BC. For the BC set of fixed- free the characteristic equation ψ :

$$\psi(x) = (1 + e^{-2\lambda x})\cos(\lambda x) + 2e^{-\lambda x} \quad (2.28)$$

Setting $x = L$ and $\psi = 0$ in eq. 2.28 the eigenvalues λ_n can be computed as eq. 2.28 has multiple solutions which can be computed by solving the equation with standard numerical methods e.g. the Newton-Raphson-method [30]. These eigenvalues λ can in turn yield the natural frequencies using eq. 2.23. The mode shapes $U(x)$ when applying this set of BC are determined by calculating the factors $D_1 - D_4$ from eq. 2.24.

For the BC set of a fixed-fixed beam the characteristic equation resulting from this is:

$$\psi(x) = (1 + e^{-2\lambda x})\cos(\lambda x) - 2e^{-\lambda x} \quad (2.29)$$

By Setting $x = L$ and $\psi = 0$ in eq. 2.29 the eigenvalues for λ can be acquired and consequently used in eq. 2.24 to find the associated mode shapes. The following figure shows the mode shapes for an arbitrary first natural frequency for the relevant sets of boundary conditions used in this work.

Figure 2.4 shows the first three mode shapes for both sets of BC presented. The plots were normalised to yield an arbitrary maximum displacement of 1 m however this is only done to represent their shape. In order to calculate the magnitude with which a beam system would react to a given load a so called frequency response analysis needs to be conducted which is shown in section.

2.4 Numerical Analysis

In real world applications often geometries are more complex than a beam or pendulum system and the equations of motion cannot be solved by the methods described in section

2.3. In order to model complex geometries, the Finite Element Method (FEM) is applied where the complex geometric domain is divided, in sub domains called elements. The elements are connected at nodes for which the equation of motions are solved. FEM is the principal computational tool for structural dynamics. In general the FEM is a way to numerically approximate the solution of partial differential equations (PDE). The geometric domain is divided up in a number of elements simplifying the geometry, over which the state quantities have to be computed. This is done by introducing so called base functions [30]. Where for example a function \hat{u} being the state quantity of a PDE can be approximated by using a linear combination of basis functions $\hat{\beta}_i$, there fore resulting in:

$$\hat{u} \approx \sum_i \hat{u}_i \hat{\beta}_i \quad (2.30)$$

where \hat{u}_i is the coefficient of the basis functions $\hat{\beta}_i$ which can be any type of function suitable for the regarded case. Gaining the numerical solution to a PDE via the FEM can be divided into four major steps [31]:

1. *Spatial discretisation:* The complex geometric domain is divided up in a finite number of elements together make up the so called mesh. For 3-D analysis the most common element shapes is cuboid or tetrahedral. These elements are connected at nodes. The mesh represents the geometry of the problem. The mesh refinement is of importance when the detailed solution need to be known locally.
2. *Element equations:* The algebraic equations for the physical problem are defined which can in turn be solved for the known shape of an element. The quantities are calculated at the node points and basis functions in eq. 2.30 are deployed to interpolate in between nodes.
3. *Assembly of element equations and solution:* The algebraic equations are assembled in matrix form. Boundary and/or initial conditions are applied to the domain and the solutions are obtained iteratively. As these matrices can become quite large special algorithms are deployed in order to solve the equations.
4. *Convergence and error estimate:* With each iteration the solution of the numerical approximation converges to the true solution of the PDE. However errors remain due to spatial approximation of the domain, approximation of the solution and numerical computation such as round-off errors [31].

Assembling the algebraic equations for each node of the mesh yields a matrix operation. For structural dynamic analysis performed in this work the equation of motion in matrix form is given by:

$$\mathbf{M}\ddot{\mathbf{U}} + \mathbf{C}\dot{\mathbf{U}} + \mathbf{K}\hat{\mathbf{U}} = \mathbf{F} \quad (2.31)$$

Where \mathbf{M} is the mass matrix, \mathbf{C} is the damping matrix, \mathbf{K} is the stiffness matrix, \mathbf{F} is the known applied force vector to the system and $\hat{\mathbf{U}}$ is the displacement vector at the nodal points. The matrices \mathbf{M} , \mathbf{C} , \mathbf{K} are determined by the basis functions as shown in [30]. As described earlier the number of elements in these matrices can become large as they correspond to the number of degrees of freedom at each node of the mesh. The

commercial FEM software COMSOL[®] uses the ARPACK package in order to solve for large scale eigenvalue problems [32].

To solve eq. 2.31 a set of boundary conditions (BC) have to be imposed. A Dirichlet condition, meaning the value of quantity is fixed at the boundary:

$$\hat{U} = C_{BC1} \tag{2.32}$$

A Neumann condition, where the derivative of a quantity is constant in the normal direction.

$$\frac{\partial \hat{U}}{\partial n} \hat{U} = C_{BC2} \tag{2.33}$$

Applying these BC to the domain and setting $\mathbf{F} = 0$, eq. 2.31 can be solved for the natural frequencies of the domain [22]. This is done under the assumption of no damping ($C = 0$). The resulting matrix formulation of the PDE eq. 2.31 can be solved by an eigenvalue formulation leading to the equation:

$$\det(\mathbf{M}^{-1}\mathbf{K} - \lambda\mathbf{I}) = 0 \tag{2.34}$$

Where \mathbf{I} denotes the identity matrix. Solving for the eigenvalues λ in eq. 2.34 yield the natural frequencies and their mode shape in analogue fashion to the analytical method shown in section [22]. However the mode shapes do not contain sufficient information on reaction of the system to a given vibrating load. There are multiple types of vibrating loads, the response of a system is calculated according to the type of vibration. These relations are further explained in the following section.

2.5 Vibrating Signals

Vibrating signals can be categorised in three different types. Periodic signals, which repeat themselves with a period $1/f$, random signals, which at each time instant are independent of values at other instants and transient signals, which have a limited duration [22]. Figure 2.5 shows this visualised.

To this work only the periodic and random vibration signals are relevant. Periodic signals are characterised by sinusoidal functions. [22].

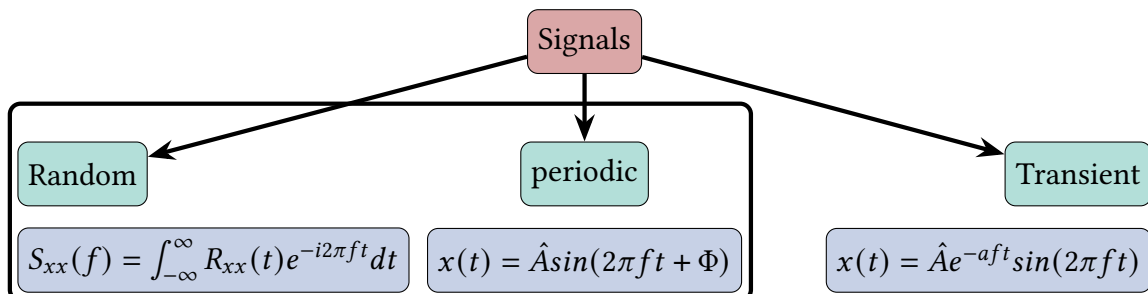


Figure 2.5: Signal types with the respective mathematical description of the signals, highlighted are the signal types relevant to this work

2.5.1 Frequency Response Analysis

Assuming a sinusoidal load actuates the system in eq. 2.31, the force is given as brandt2023noise:

$$F(t) = \hat{A}\sin(2\pi ft + \Phi) \quad (2.35)$$

Where $F(t)$ is a load, Φ denotes the phase shift and \hat{A} represents the amplitude of the signal. Such a sinusoidal signal can be used to actuate the system at a set frequency f , which forces the system to respond. The response of a system to a sinusoidal in the frequency domain can be modeled with the so called frequency response analysis [22].

To analyse the response of a Laplace transformation in the time domain is applied to eq. 2.31 [22]

$$[s^2\mathbf{M} + s\mathbf{C} + \mathbf{K}]\hat{U}(s) = F(s) \quad (2.36)$$

where s is the Laplace operator. All matrices in eq. 2.36 are known. The only unknown quantity in this equation is the displacement vector $\hat{U}(s)$, thus a relationship between the input signal and the output signal can be established as [22]:

$$H(s) = \frac{\hat{U}(s)}{F(s)} = [s^2\mathbf{M} + s\mathbf{C} + \mathbf{K}] \quad (2.37)$$

Hence the transfer function of a system is only dependent on the known quantities: mass matrix \mathbf{M} , elasticity matrix \mathbf{K} and damping matrix \mathbf{C} . The displacement of a system as a reaction to a known force can therefore be computed by rearranging eq. 2.37 to yield the displacement vector $\hat{U}(s)$. Applying a Fourier transformation to the transfer function, which is in the time domain, the frequency response which is in the frequency domain can be acquired [22]. The frequency response is defined as:

$$H(f) = \frac{\hat{U}(f)}{F(f)} \quad (2.38)$$

Formulating the frequency response has the advantage over the transfer function, to calculate the systems response to sinusoidal loads for a set frequency range.

When applying the equation of motion eq. 2.31 to a pendulum system the frequency response is given as [22]:

$$H(f) = \frac{1/k}{1 - (f/f_n)^2 + i2c(f/f_n)} \quad (2.39)$$

Where k is the spring constant of the suspension and c is the relative damping factor. The eq. 2.39 is normalised to the natural frequency f_0 . Further examining eq. 2.39 it becomes evident that the frequency response of the system would approach infinity, if the relative damping factor is set to zero. To prevent this, damping is set a damping factor to 0.02 [28]. The figure below shows an arbitrary frequency response of a pendulum system of eq. 2.39 with $c = 0.02$ in a graph:

The system shown in fig. 2.6 has a nearly constant response at low frequencies scaling with $1/k$. Only close to the natural frequency the response becomes significant and reaches a maximum at f_0 , beyond the natural frequency the displacement will reach very small

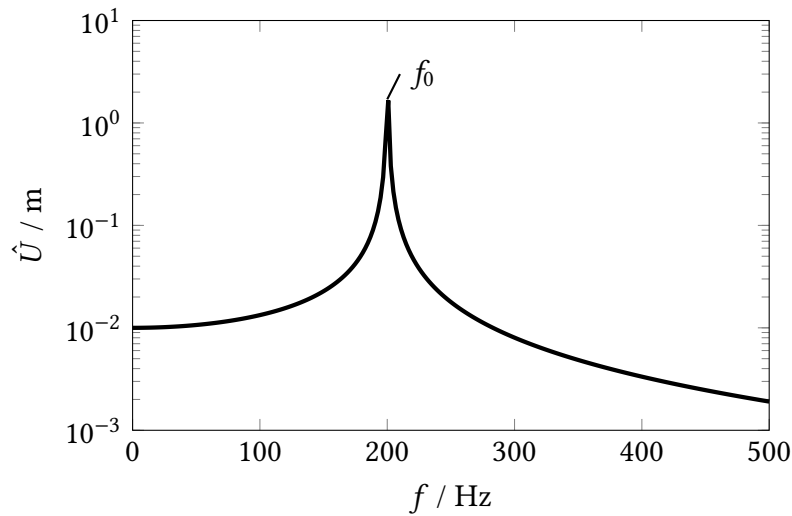


Figure 2.6: Arbitrary Frequency response of a single degree of freedom system

displacements, due to the denominator of eq. 2.39 increasing. Evident from both eq. 2.39 and fig. 2.6 the frequency of a system only depends on intrinsic characteristics such as the mass matrix \mathbf{M} , damping matrix \mathbf{C} and elasticity matrix \mathbf{K} . When the amplitude a of the sinusoidal load from eq. 2.35 is known the explicit displacement of the system can be computed.

2.5.2 Random Vibration Analysis

Figure 2.5 shows the second type of vibrations relevant to this work are random vibrations. A random signal contains all its characteristic frequencies statistically, opposed to periodic signals, which oscillate at a set period $1/f$. This means a random signal contains all frequencies simultaneously and has to be defined in a spectrum. The so called power spectral density (PSD) is introduced, which enables the extraction of relevant oscillating quantities, e.g., displacement, force, pressure, etc. at discrete frequencies [22]. The PSD is extracted from a time series of a measured time series.

On the basis of a measured time series of a signal, detailed time related information, can be extracted via the so called auto correlation function $R_{xx}(t)$. The auto correlation relates a measured quantity at a given time to the same measured quantity at a shifted time [33]. To convert the time related information to the frequency domain a Fourier transformation is performed on the auto correlation function, which yields the PSD:

$$S_{xx}(f) = \int_{-\infty}^{\infty} R_{xx}(t) e^{-i2\pi ft} dt \quad (2.40)$$

where $S_{xx}(f)$ is the PSD, i is the imaginary unit and f is the frequency.

In vibration analysis the most popular type of PSD is the displacement PSD, where the state quantity is the displacement having the units (m^2/Hz) depicted in a spectrum shown in figure is the square root of the displacement PSD 2.7.

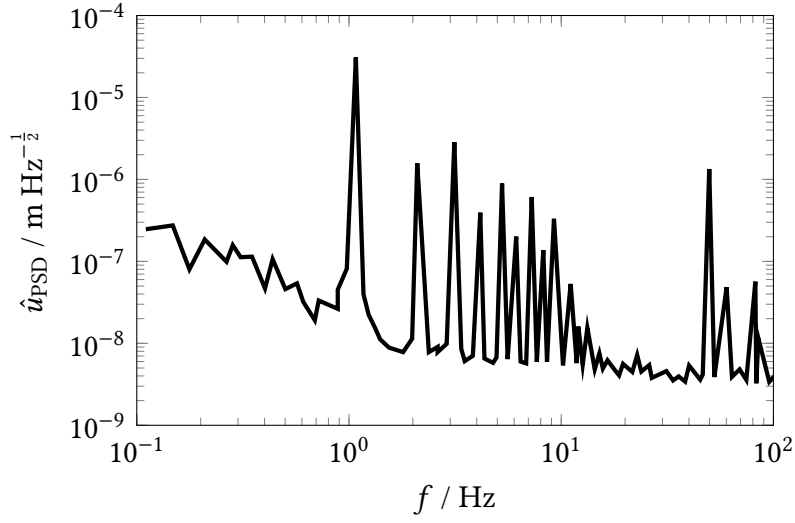


Figure 2.7: Displacement PSD, where $\sqrt{S_{xx}(f)} = \hat{u}_{\text{PSD}}$, of a Sumitomo cryocooler [34]

As the signal is of statistical nature, the root mean square (RMS) values is given to describe a state quantity within a specific frequency range. In order to calculate the root mean square (RMS) value of the state quantity, such as \hat{u}_{RMS} is given by the area under the PSD in the frequency interval [33]:

$$\hat{u}_{\text{RMS}} = \sqrt{\int_{f_1}^{f_2} S_{xx}(f) df} \quad (2.41)$$

The response of a system actuated with a random input signal is calculated analogue as described for the case of sinusoidal actuation with the difference the amplitude of the actuating force being variable with frequency and due to the statistical nature of the signal input, the response is given as an RMS value.

3 Setup and Boundary Conditions

GRAVITHELIUM test facility will have two major experimental campaigns measuring the Q -factor. The first campaign involves monolithic suspension fibres and empty suspension tubes [7]. The second measurement campaign focuses on the He-II filled suspension tubes. The samples will have a length of ca. 1 m and a diameter in the range of 8 mm to 9 mm. The measurements will be conducted in a temperature range of 300 K to 2 K [7]. A cryostat design has been outlined by Korovesi et al. [7]. The design involves an outer vacuum chamber which is 3 m in height and 1.5 m in width. Within the vacuum vessel there is a radiation shield cooled to ~ 70 K by the first stage of a pulse tube PT-425 cryocooler from CRYOMECH[®]. Attached to the cryocooler's colder second stage is a helium tight test chamber functioning both as a radiation shield and a test chamber cooled down to ca. 3 K [7].

The test facility will conduct two major experimental campaigns, depicted in figures 3.1 and 3.2. The first experimental campaign involves the measurement of energy dissipation of monolithic suspension fibres and empty suspension tubes. These measurements will be conducted for mechanically unloaded and loaded samples [7]. The second measurement campaign involves the investigation of dissipation mechanisms in the He-II filled suspension tube. The experimental campaigns conducted of the test facility are summarised in two phases corresponding to experimental campaigns: [7]

- Phase-I: loss angles measurement of unloaded and loaded samples. The samples in this phase are monolithic suspension fibres and empty suspension tubes. The measurements are conducted in the temperature range of 3 K to 300 K.
- Phase-II: loss angle measurements of He-II filled suspension tubes. The heat flux is varied investigating the influence on dissipation. Measuring loss angles in a temperature range below 2.17 K.

The mechanical loss measured is a characteristic of a system. Hence to measure the dissipative mechanisms within the sample, the extrinsic losses of the measurement setup need to be minimised. Extrinsic losses include, gas damping losses, eddy current losses, recoil losses and clamping losses [25, 24]. Gas damping losses, are caused by aerodynamic friction and are mitigated by conducting the measurements in an ultra high vacuum environment (1×10^{-7} mbar to 1×10^{-12} mbar) [7]. Eddy current losses are caused by electromagnetic interference and are minimised by an adequate actuation and detection system. Recoil and clamping losses are caused by the sample support structure (SSS). Figure 3.1 depicts the SSS in the test chamber. The SSS is comprised of the key components: Support block, cage, sample holder suspension (SHS), sample holder (SH), sample (SA) and load mass. Highlighted are the most relevant components to the scope of this work.

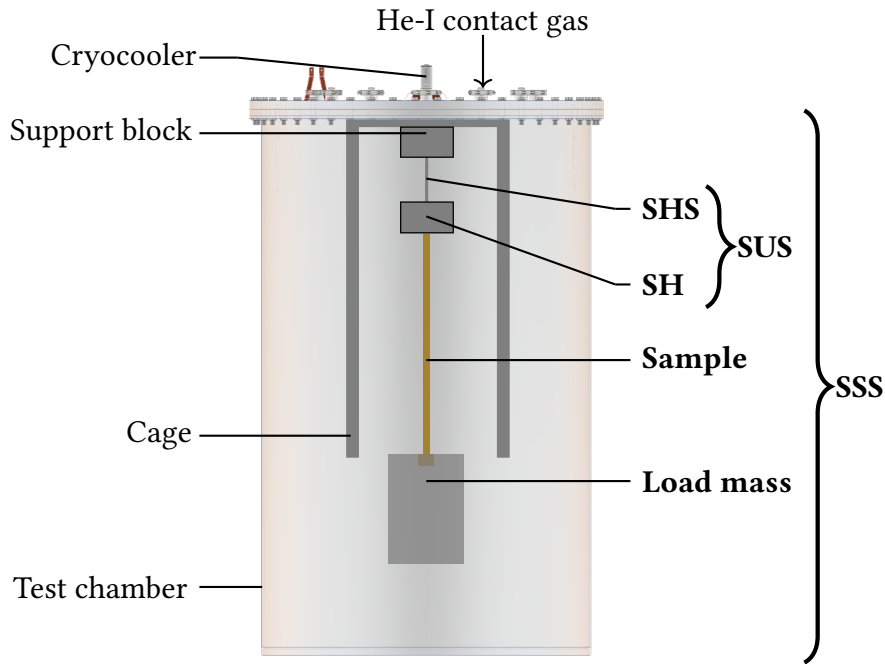


Figure 3.1: Helium test chamber in Phase-I, adapted from [7]

The support block attaches the entire SSS to the top flange of the test chamber. The cage houses relevant instrumentation such as actuator, optical detection sensor and temperature sensors [7]. The SH clamps the sample in place and needs to be designed for reducing the clamping losses. The SHS suspends the SH from the support block. The SHS and SH together form a pendulum system, which is called the sample support system (SUS). The SUS forms a crucial subsystem of the SSS, with the aim of reducing recoil losses. Therefore minimising the redistribution of energy from the SA to the residual SSS [7]. This requires the design of SH and SHS together.

In phase-I the measurements will be conducted in a cryogenfree cryostat [7]. The cooling for this phase will be provided by a CRYOMECH[®] PT-425 pulse tube cryocooler [7]. He-I gas can be deployed as a contact gas, aiding the cool-down phase of the experimental set up via convection. The system can be cooled down to a temperature of 3 K [7].

In phase-II the dissipative mechanisms of a He-II filled suspension tube is investigated. The application of He-II in cryogenic suspensions provides a potentially low dissipation medium and constitutes a new field of research [6]. This application requires experimental investigation. A laboratory scaled He-II supply cryostat has been developed in [35] achieving temperatures below 2.17 K. The test cryostat and He-supply cryostat are connected via a helium supply transfer line. In phase-II no mechanical loads will be applied to the SA [7].

Figure 3.2 shows SSS in the test chamber setup for phase-II. The SSS design for phase-II aims to maximised comparability of phase-I and phase-II. The SSS is comprised of the same key components as for phase-I, with the addition of He-II tubes.

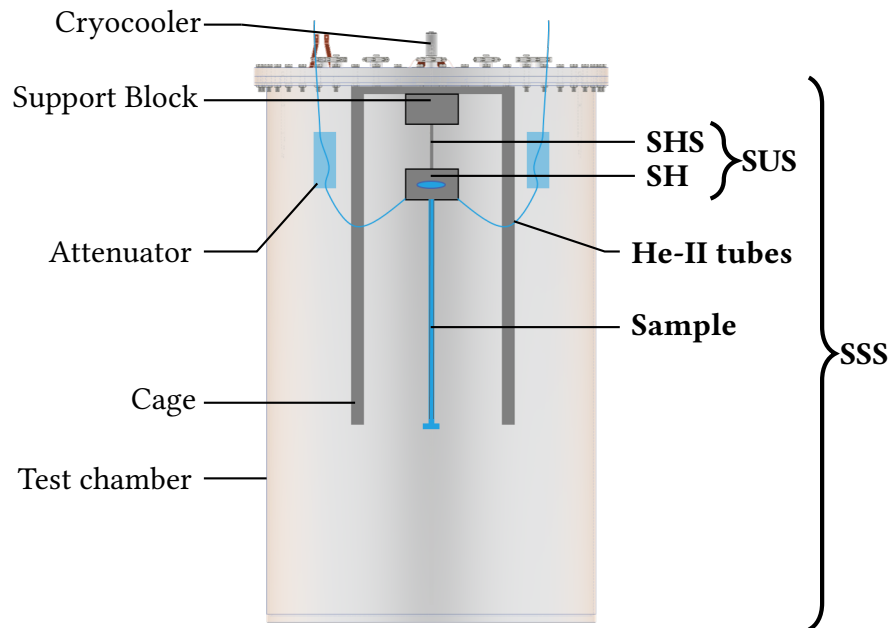


Figure 3.2: Helium test chamber in Phase-II adapted from [7]

The SSS for phase-II has the same components as in phase-I with the addition of the helium supply and return tubes. These transport the liquid He to the suspension tube. The He-tubes are isolated from the He-transfer line via a vibration attenuation system. This attenuation system reduces the vibrations stemming from the He-supply cryostat. These vibrations would interfere with the measurements and appear as noise in the measured signal. The design of such a system is beyond the scope of this work. The SH in phase-II functions as an interface between He-II supply and return tubes and a suspension tube. The design of the SH for phase-II is further explained in section 6. The suspension tube and SH of phase-II form a single body, in order to ensure He-tightness.

3.1 Design Limitations

A preliminary design of the SSS has been provided by Korovesi et al. However the parameters of each component of the SSS were not set. The dimensions of the outer vacuum chamber and test chamber were provided as set. The dimensions are presented in table 3.1. In order to design the SSS adequately, design limitations have to be defined. The obvious first limitation to the SSS is the spatial limitation. The SSS dimensions cannot exceed the test chamber dimension in height or diameter. The length of the investigated sample 1 m is taken from the ET-LF marionette suspension [6]. Additionally to the sample a conservative 0.5 m was assumed for additional setup components, including space needed for the mass suspended from the sample and a safety structure catching the sample in case of material failure. The remaining length for the SSS is 0.45 m.

Table 3.1: Dimensions of GRAVITHELIUM vacuum and test chamber

Quantity	d / m	h / m
Outer vacuum chamber	1.5	3.0
Inner test chamber	1.2	2.0
Additional setup	-	~ 0.5

Additionally to the spatial design limitation a second type of limitation arises from the natural frequency values of the samples. The Q -measurements are conducted at resonance frequencies of the sample. Overlapping of natural frequencies of the SUS and SA has to be avoided. This would cause a high response of the SUS. Due to a high response, the SUS will absorb a significant amount of energy. According to eq. 2.15 this effect results in an elevated loss angle of the overall system. Therefore a definition of natural frequencies, which are relevant to the Q -measurement need to be defined. Which limits the frequency range for which the SUS needs to be optimised for.

3.2 Sample Analysis

In this section the SA natural frequencies, relevant to the Q -measurement are defined. The natural frequencies of the sample are calculated via FEM modal analysis (MA). As described in section 2.3, the MA does not yield a displacement to a given sinusoidal load. Hence a subsequent frequency response analysis (FRA) shows the displacement response, of a SA to a given sinusoidal load. The detection sensors sensitivity is taken as a limitation to minimal acceptable displacement response of the SA. The natural frequencies relevant to the Q -measurement have larger a displacement response than the minimal value, given by the detection system limitation.

Figure 3.3 shows the generalised steps taken to conclude which natural frequencies are relevant to the Q -measurement. First a SA geometry is defined and meshed. The SA is taken as a subsystem of the SSS. Meaning the SUS is excluded from the model and is implemented in form of BC. Specifically one of the SA heads is implemented as a fixed constraint (FC) Dirichlet type BC. This boundary condition assumes the SUS does not experience displacement. This is only a first approximation of and the total system will be investigated in chapter 4.

The MA conducted in the FEM model yields the natural frequencies and mode shape. On the basis of the mode shapes the ideal placement of the actuator can be decided on. The actuator should be placed at a point of the suspension fibre, resulting in a large local displacement. The actuator is integrated into the FEM modal via a boundary load (BL), Neuman type BC. The BL is a sinusoidal force applied to the SA and is relevant for the FRA. Placing the BL at the point of maximal displacement yields the largest response of the SA. The displacement response of the SA is compared to the sensitivity limit of the detection sensor. On this basis the measurable sample natural frequency are defined.

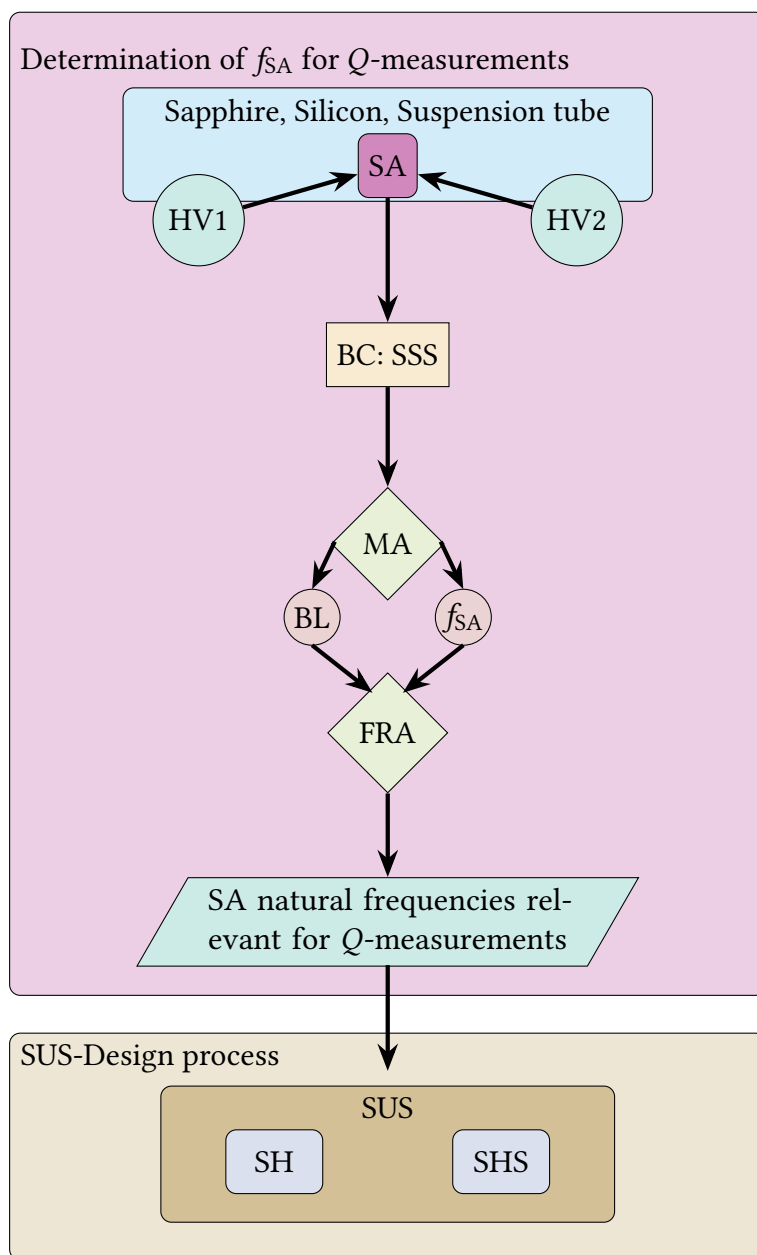


Figure 3.3: Flowchart of how the relevant natural frequencies are defined. This section is limited to the steps to determine f_{SA}

3.2.1 FEM implementation of Sample

Phase I will conduct Q -measurements of two different SA types, namely monolithic suspension fibres and suspension tubes. The test set up has to be adequate to both SA types. This is accomplished by designing a clamping system accommodating the different SA types. The basis for the clamping system was taken from the preliminary design given by Koroveshi et al., which is based on the clamping design presented in [8]. The clamping system of [8], is presented in chapter 5 figure 5.2.

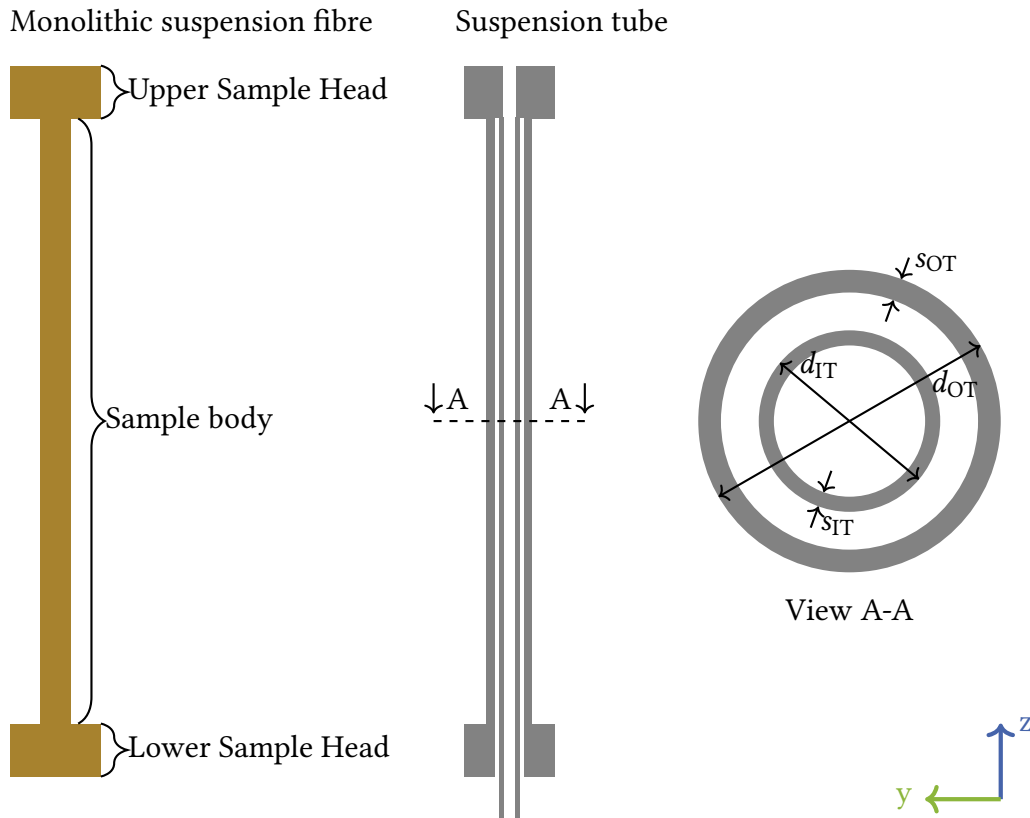


Figure 3.4: SA geometry nomenclature

The SA are designed with so called heads at each end. The heads are used as shoulders clamping the sample to the SH. Figure 3.4 shows the sample geometry. The sample geometry is based on a published work which measured Q factors of monolithic sapphire suspension fibres [8].

The SA geometric variation presented in this work, is limited to variation of the sample head geometry. Two head variants (HV) for both sample types, have been investigated. HV 1 represents the current state of the art for silicon suspension fibres. The largest head-to-body-diameter ratio currently manufacturable is limited to a factor of 2 [36]. HV 2 represents the case, where the head-to-body-diameter ratio is 4. This is realisable for titanium suspension tubes and mono crystalline sapphire [8]. The monolithic sapphire suspension fibres used in [8] have a head-to-body-diameter ratio of ~ 6 . Table 3.2 shows the dimensions deployed for the monolithic suspension fiber samples. The sample body dimensions were taken from the marionette suspensions of the ET-LF cryogenic payload design presented in [6].

The suspension tube is made of titanium and is designed as an annular gap heat exchanger from which the ET-LF marionette is suspended [6]. The suspension tube consists of an outer tube (OT) with an outer diameter $d_{OT} = 9.03$ mm and a narrow inner tube (IT) with an outer diameter of $d_{IT} = 5.8$ mm [6]. The IT functions as the He-supply and the OT functions as the He return. The IT is protruding out of one end of the suspension tube by 10 mm. Table 3.3 shows the dimensions of the suspension tube samples [6].

Table 3.2: Geometry variation of the monolithic suspension fibres

	l / mm	d / mm	m / g	
			sapphire	silicon
Sample body	1000	8	200	117
Head variant 1	5	16	4	2
Head variant 2	20	32	63	40

Table 3.3: Geometry variation of the Suspension Tube.

	s_i / mm	l / mm	d_o / mm	m / g
Sample body OT	0.36	1000	9.03	23
Sample body IT	0.05	1030	5.80	2
Head variant 1	-	5	16	2
Head variant 2	-	20	32	35

Boundary Conditions.

The MA is conducted with deployed BC. A fixed constraint (FC), Dirichlet type BC (eq. 2.32) is deployed to the upper sample head. With the assumption being, the SH is not experiencing any displacement. Gravity is activated in the model along the samples longitudinal axis, as gravity influences to natural frequency.

To perform a FRA the BL BC needs to be placed. Based on the results of the MA, the placement of the actuator is decided. Actuating the sample at resonance is done electrostatically, by a common contactless comb actuator [8]. This actuator functions as a capacitor, where the actuator plate acts as the first plate of the capacitor and the sample acts as the second plate of the capacitor [8]. The SA is attracted or repelled by a resulting, sinusoidal electrostatic force F_{el} .

Detecting the ring down can be done by a so called shadow meter, where a LASER is pointed on a photo diode. The sample is placed in the pathway of the LASER beam. The vibration of the sample, causes an oscillating signal at the photo diode. The decay of the signal is used to deduct the decay time τ_{decay} for the Q -measurements [24]. The detection system has an assumed sensitivity of measuring minimal displacements of $1 \mu\text{m}$. The electrostatic actuation and detection scheme of the sample is shown in figure 3.5.

The actuation force F_{el} can be calculated by eq. A.1. The actuator design was taken from [8], which is a square plate with aside length of 5 cm. As a supply voltage a constant voltage of 500 V was taken in this work adapted from [10]. The distance between the actuator to the sample was assumed as to be 1.15 cm, taken from [8].

Implementing the actuator to the FEM is accomplished via the BL BC. A 5 cm high area on the SA is defined, on which a resulting sinusoidal force is applied. The resulting electrostatic force by the actuation scheme is calculated by eq. A.1, actuating the sample in y-axis. The point chosen to plot the frequency response, is decided on by the mode

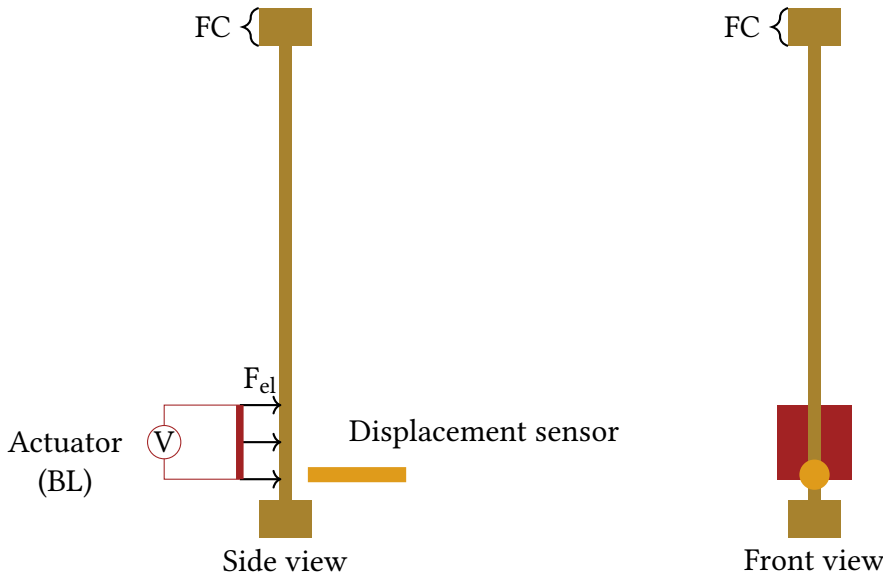


Figure 3.5: Schematic view of the sample Q -measurement actuation and detection set up. The actuator and sensor are fixed at the cage, adapted from [8]

Table 3.4: Set boundary conditions

Parameter	Value
Actuated surface area	$6.3 \times 10^{-4} \text{ m}^2$
Distance of actuator	$1.15 \times 10^{-2} \text{ m}$
Applied voltage	500 V
Direction for actuation	y-axis
Resulting force	$5 \times 10^{-4} \text{ N}$

shapes. The position of this point reflects the point of largest displacements on the SA. Table 3.4 summarises the boundary conditions applied for the FRA.

For the mono crystalline materials sapphire and silicon the elastic behavior is described by eq. 2.5. The temperature dependent elastic coefficients for mono crystalline materials have been taken from literature and were implemented in to the FEM model.

Depending on the crystallographic plane aligned with the cartesian z -axis, the model calculates an equivalent Young's modulus. For silicon simulating the $\langle 100 \rangle$ plane is accomplished by aligning the length geometry to the z -axis. In order to simulate the $\langle 110 \rangle$ plane the geometry is turned by 45° in the Cartesian x - y plane. In order to simulate the $\langle 111 \rangle$ plane the geometry is turned by 45° in both the Cartesian x - y and y - z planes. The modal analysis have been conducted for the three silicon main crystallographic orientations. For sapphire the modal analysis is restricted to the α plane [13].

For suspension tube samples the OT is actuated and Q measurements are conducted. However as the suspension tube consists of titanium, a metallic material, electrostatically actuating the OT might effect the IT due to its conductive behaviour. However investigations have been made in the scope of this work, showing that the displacement of

the IT at $f_{SA,OT}$ is in the order of ≈ 100 nm. Hence, IT displacement is negligible and the analysis conducted in this work are limited to the suspension tubes OT. In the measurement campaigns the displacement of the OT should not exceed 1.25 mm, which is the clearance between the OT and IT.

Meshing

The geometric domain was meshed according to mesh convergence, meaning further refinement of the mesh yields a difference of 1% in natural frequency value. A free tetrahedral mesh was implemented, the mesh parameters are given in the table 3.5.

Table 3.5: SA mesh parameters

Quantity	Setting
Maximum element size	6 mm
Minimum element size	4 mm
Maximum growth rate	1.15
Curvature rate	0.6
Resolution of narrow regions	0.7

The minimum element size of the mesh is defined as 4 mm, the maximal growth factor which determines the maximal size increment from one element to the next larger element is set to 1.15. The maximum element size is set to 6 mm. Both curvature rate and resolution factor of narrow regions were predefined by the solver and were not changed. The resulting mesh consists of $\sim 15,500$ elements with a total number of $\sim 140,000$ nodes.

3.2.2 Modal Analysis

Conducting a MA of the two sample types and utilising HV1 and HV2, with the stated BC relevant to the analysis, the natural frequencies, presented in table 3.6 can be deduced. The mode shapes for HV1 SA are depicted in figure 3.6. The mode shapes for HV2 SA are depicted in figure A.1. The natural frequency values for silicon SA are presented for different crystallographic orientations, as they are possible candidates for suspensions in ET-LF mirror/ marionette stage [10]. The frequencies presented for the sapphire SA are modelled using the α -plane of the crystallographic orientation [37].

Due to the slightly longer total length of the HV2 samples ($\Delta l = 4$ cm) and the heads larger moment of inertia, the natural frequencies for HV2 SA, are comparatively lower than for the samples using HV1 SA.

As described in section 2.3 a MA does not yield information on displacement of the sample to a given load. The mode shapes in figure show the dimensionless displacement shape of the SA at the respective resonance frequency. The displacement has been normalised to yield a maximal displacement of 1. From figure 3.6 it can be seen that for HV 1 SA the maximal displacement occurs at the free end of the SA. From figure A.1 it can be seen that for HV 2 SA the maximal displacement does not occur at the free end of the SA. For HV2 SA the point of highest displacement is dependent on the mode order. This is attributed to HV2 introducing an additional mass at the end of the sample. This creates tension in the sample, changing the mode shape.

Table 3.6: Natural frequency of SA for both HV

Mode number	Si <100>	Si <110>	Si<111>	Sapphire	Suspension tube
HV1					
1 st / Hz	8	9	10	12	8
2 nd / Hz	50	57	60	73	49
3 rd / Hz	140	161	167	203	138
4 th / Hz	275	315	329	400	272
HV2					
1 st / Hz	6	6	7	8	3
2 nd / Hz	41	46	48	60	38
3 rd / Hz	120	138	145	175	120
4 th / Hz	245	280	292	356	247

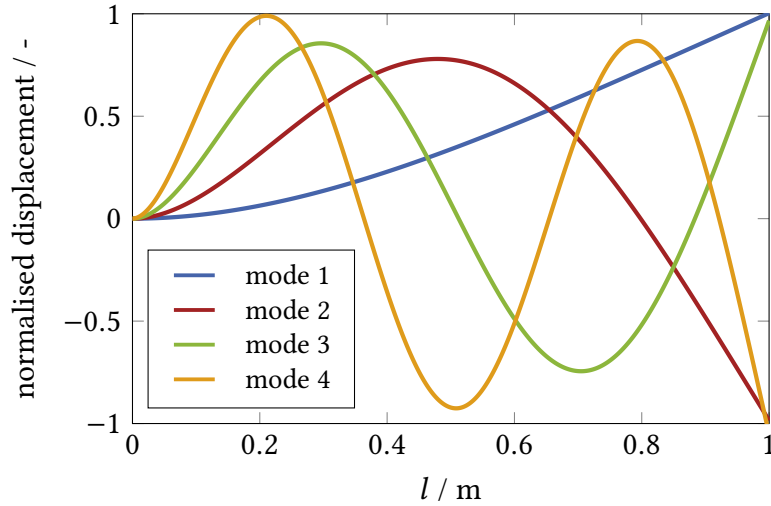


Figure 3.6: Mode shapes of the first four modes of HV1 SA

Validating the implemented material data is done by comparing the computed equivalent Young's modulus, which are a result of the FEM, to measured Young's moduli for the sapphire and silicon samples. This is done to ensure the elasticity coefficients from literature were correctly implemented to the model. The Si<100> plane has a simulated equivalent Young's modulus of $E_{Si} = 165$ GPa. For sapphire the simulated equivalent Young's modulus is $E_{sapphire} = 406$ GPa both values are within the range for measured values for Young's moduli found in literature [16, 12].

Validating the FEM result yields correct natural frequencies, a comparison with analytically calculated SA natural frequencies and mode shapes as shown in section 2.3. Assuming Bernoulli-Euler Beam theory for the sample the mode shapes can be calculated by eq. 2.24. The computed mode shapes via the FEM model can be validated by comparing figure 3.6 with figure 2.4 showing a qualitatively good agreement in mode shapes.

The analytically calculated natural frequencies, by eq. 2.23, are compared to the natural frequencies computed via the FEM simulations shown in table A.1. The largest deviation of the analytically calculated and FEM values have been found for sapphire. The deviation of analytically calculated to numerically calculated is 6% for this case and is attributed to deviation in measured and simulated Young's modulus.

In phase-I the Q -measurements will be conducted in a temperature range, of 3 K to 300 K. The temperature dependent natural frequencies of the sample types are shown in figure A.3 for HV1 SA and figure A.4 for HV2 SA. A MA has shown that the natural frequencies tend to increase by maximal 0.5 %, compared to their value at 300 K. The values for different temperatures, is presented in A.3 for HV1 samples and A.4 for HV2 samples.

3.2.3 Frequency Response

Concluding the MA the placement of the placement of the BL BC for the FRA can be decided. The boundary load is set to the part of the sample experiencing largest displacement. From figure 3.6 it can be seen, for HV1 samples the placement of the BL is ideal at the free end. The displacement response is evaluated at this point as well.

For the HV2 samples the placement of the BL BC is not as straight forward. Figure A.1 shows the point of largest displacement of the SA shifts with the order of mode. Therefore the BL BC is set to a point, which does not coincide with any nodal points. Nodal points are points in which no displacement occurs. The BL is placed to the 0.8 m mark of the sample, as the displacement is sufficiently large for all modes in that point.

Additionally deducting from the MA the SA are actuated in the frequency range of 0 Hz to 410 Hz. The BL force is the sinusoidal F_{el} . The force is calculated with the presented values of table 3.4. To prevent the frequency response diverging to infinity a constant damping factor of 2% is implemented, across the whole actuated frequency range. This value is typically assumed for FRA [22, 30]. Figure 3.7 shows the frequency response plot of the HV1 sample and the set sensitivity limitation of the detection system, assumed to be 1 μm .

The frequency response peaks at the samples natural frequencies as described in section 2.4. At low frequencies the energy needed to actuate the sample is small. The energy need to actuate the sample increases with frequency. Figure 3.7 shows this relation for the HV1 SA and figure A.2 shows the displacement response for HV2 samples. The SA displacement response for the first two modes are well above the assumed sensor sensitivity, for both sample types. The displacement of the first mode even exceeding 1 cm. Large sample displacements should be avoided, due to the risk of material fatigue. Reducing the displacement, can be accomplished by scaling the voltage down.

Investigating the HV1 SA third mode, it can be seen that the displacement of the suspension tube at 138 Hz is at 1.8 μm . The displacement for silicon sample at 141 Hz is at 1.6 μm . Investigating the HV2 SA third mode, the displacement response of the suspension tube is at 1.7 μm and for the silicon sample is at 1.0 μm . Concluding from the FRA, the first three modes of the suspension tube and silicon sample and the first two modes for the sapphire sample are within the sensitivity, conservatively assumed for the detection sensor. For sapphire the third mode becomes measurable when increasing the actuation

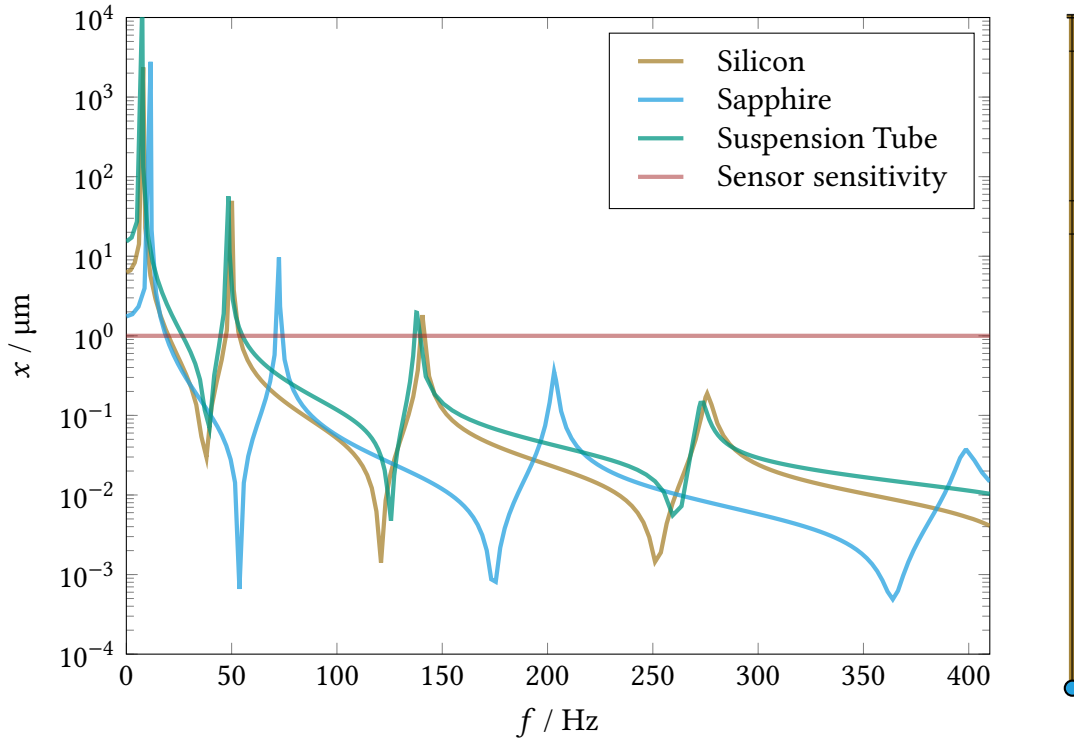


Figure 3.7: Frequency response of the HV1 SA. The cyan mark on the SA geometry represents the actuation and evaluation point for the displacement response.

voltage to 1 kV. Increasing the displacement from $0.3 \mu\text{m}$ to $1.3 \mu\text{m}$ for HV1 SA and from $0.2 \mu\text{m}$ to $1.1 \mu\text{m}$. Actuating with high voltages such as 1.5 kV is possible [38].

Concluding from the FRA at room and low temperatures of both SA types and HV, the sample modes can be actuated using a reasonably low voltage of up to 1 kV. Thus the modes relevant for the Q -measurements are in the range of 5 Hz to 205 Hz. The measurable modes therefore also limit the frequency for which the SSS needs to be optimised for. Particularly ensuring the natural frequencies of components making up the SSS, should not coincide within the frequency range 5 Hz to 205 Hz.

In the following sections the results of a comprehensive parameter study on feasible an SSS design to conduct the Q -measurements is presented. The parameters used for the SSS design in this work are categorised as *design parameters* and *evaluation parameters*. Design parameters are defined as parameters changed directly at the designed component these include diameter, length, height, width, angles, composition, etc. Evaluation parameters on the other hand are defined as parameters used to judge the quality of the set design parameters. The evaluation parameters include: dilution factor (eq. 2.20), natural frequencies, frequency response, strain density u_{max} (eq. 2.14) and integral strain energy ratio $\frac{U_j}{U_{total}}$ (eq. 2.15).

4 Sample Support Structure Design Phase-I

As described above in section 3 the scientific objectives for Phase I are: conducting Q -measurements of monolithic suspension fibres and empty suspension tube samples. Furthermore the Q -measurements are conducted without and with applied mechanical load to the sample. Investigating the effect of tension of the Q -factor. In this work a SSS was designed which is compatible with these objectives. [7]

This chapter presents the design process and the resulting design of the SSS, for phase-I. The design process was conducted in two sections. First the design for the SSS was performed for the case where no load is applied to the sample. In the second section the designed SSS for the case where no load is suspended from the sample is adapted to accommodate the applied load to the sample.

4.1 Setup Design for Unloaded Samples

General Geometry

Figure 4.1 shows the test setup of the test chamber.

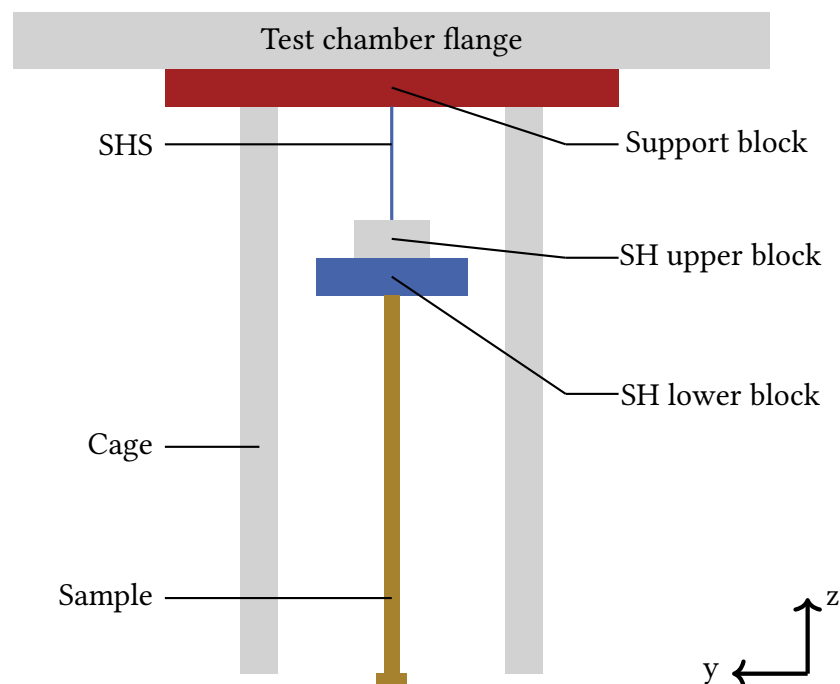


Figure 4.1: General SSS geometry, without load suspended from the sample

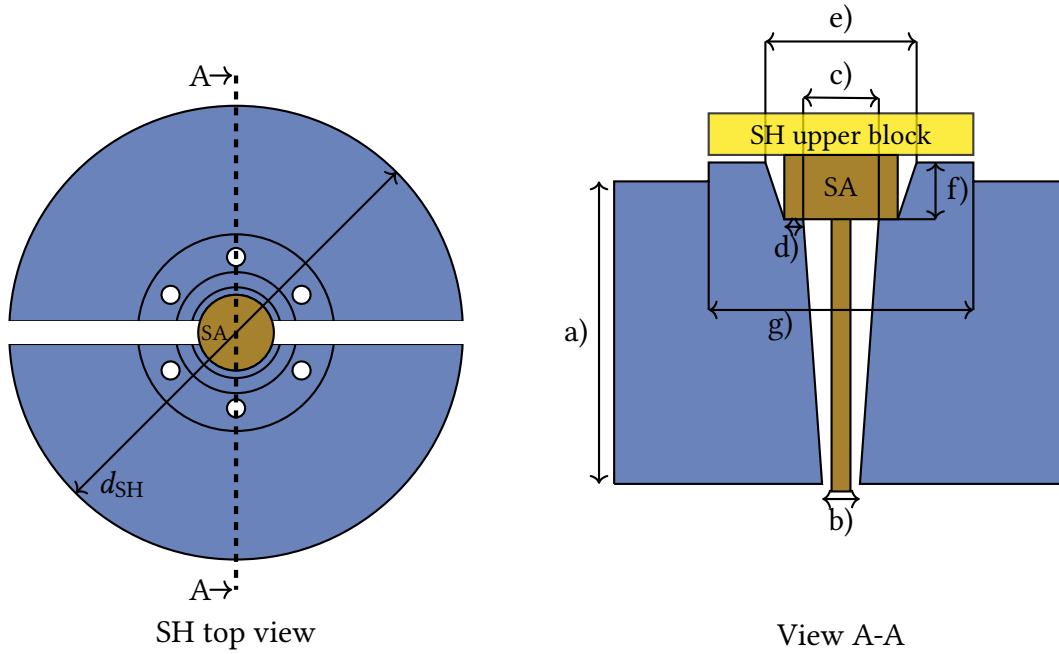


Figure 4.2: Detailed schematic of the SH geometry, with the according nomenclature presented in table 4.1

A conceptual design of the SSS has been conducted by Koroveshi et al. [7]. Table A.3 shows key features of this conceptual design.

The support block is a thick copper plate rigidly attached to the upper flange. The cage and SHS are rigidly connected to the support block. The SHS and SH comprise the SUS which is configured as a pendulum system. The goal of the SUS is minimising recoil losses, hence minimising the distribution of energy from the SA to the highly dissipative SSS. Additionally the SUS aims to suppress the transmission of vibrations from the environment to the SA, hence reducing noise and decreasing measurement uncertainty. The SHS is a fibre with heads at each end which serve as clamping bodies, clamped to the support block and SH. The SHS heads diameter is $d_{\text{Heads,SHS}} = 15 \text{ mm}$ with a height of $h_{\text{Heads,SHS}} = 5 \text{ mm}$. Material, SHS body diameter and length were open for selection and their final values are evaluated in the scope of this work.

The design of the SH for this set up is based on [8, 38], which is presented in chapter 5, in figure 5.2. The adapted SH design for GRAVITHELIUM, which is based on the design presented in [8]. The SA is fixed to a SH lower block, which has a cone shape cut out to put the SA inside. The SA head is seated in the so called saddle, which denoted as the letter d) in figure 4.2. The saddle support the SA from below. The SA head is clamped by a flat upper block from top. The SH lower block has an elevated section, which is polished. The SH upper block is polished as well. This allows the precision alignment of the SA.

Furthermore the SH lower block is designed in a symmetrical fashion, balancing the system suspended from the single SHS. The SHS is attached to the SH upper block.

The boltholes in the SH lower block are kept close to the sample head, aiding the alignment of the sample. The section view A-A in figure 4.2 shows the geometry of the

Table 4.1: SH geometry naming convention and values.

Letter	Name	Value/Variable
a)	Sample holder height	h_{SH}
b)	Lower cutout hole	10 mm
c)	Saddle inner diameter	d_H
d)	Saddle width	2 mm
e)	Sample head cutout diameter	$d_H + 4$ mm
f)	Sample head cutout height	$h_H - 1$ mm
g)	Sample holder contact	70 mm

saddle, in which the sample is seated. The table 4.1 shows the naming convention and values for the sample holder saddle geometry. Certain features of the cutout in the sample holder are dependent on the SA head geometry. Table 4.1 presents these features depending on head diameter d_H and head height h_H .

4.1.1 General Boundary Condition

As described above the support block serves as an anchor to the upper head of the SHS. Therefore the upper head of the SHS is implemented as a FC BC for the MA.

The FRA is conducted by actuating the samples with the values presented in table 3.4 for the electrostatic actuation. The placement of the boundary load depends on the HV deployed to the system and is extracted for the MA in section 3.2. The saddle geometry of the SH is also adjusted to the HV deployed to the SA.

The bolts clamping the SH lower and upper blocks together, were replaced by a rigid connector boundary condition. Gravitational pull is activated along the z -axis in the model as the natural frequencies strongly depend on the tension imposed by static load.

Modelling the SSS design in FEM has certain limitations. Friction between parts is not accounted for in the FEM model. As the parts are rigidly clamped together the main contributor to the clamping loss is the elastic deformation of the SH caused by the displacement experienced by the sample. Tension caused by the bolts cannot be modeled. As shown in eq. 2.14 the integral strain scales with the energy dissipation in a component. Creating a large tension within the SH by the bolts causes initial strain. Additional strain is caused by the elastic deformation due to the sample vibration. Therefore the sample should be clamped as lightly as possible ensuring it is held in place, but not to induce further strain.

4.1.2 Dimensioning of Sample Support System

The SUS is composed of SH and SHS with the aim to reduce recoil losses. The SH serves the purpose of SA clamp and suspended mass of the SUS pendulum system. steps taken to design the SUS is presented in figure 4.3.

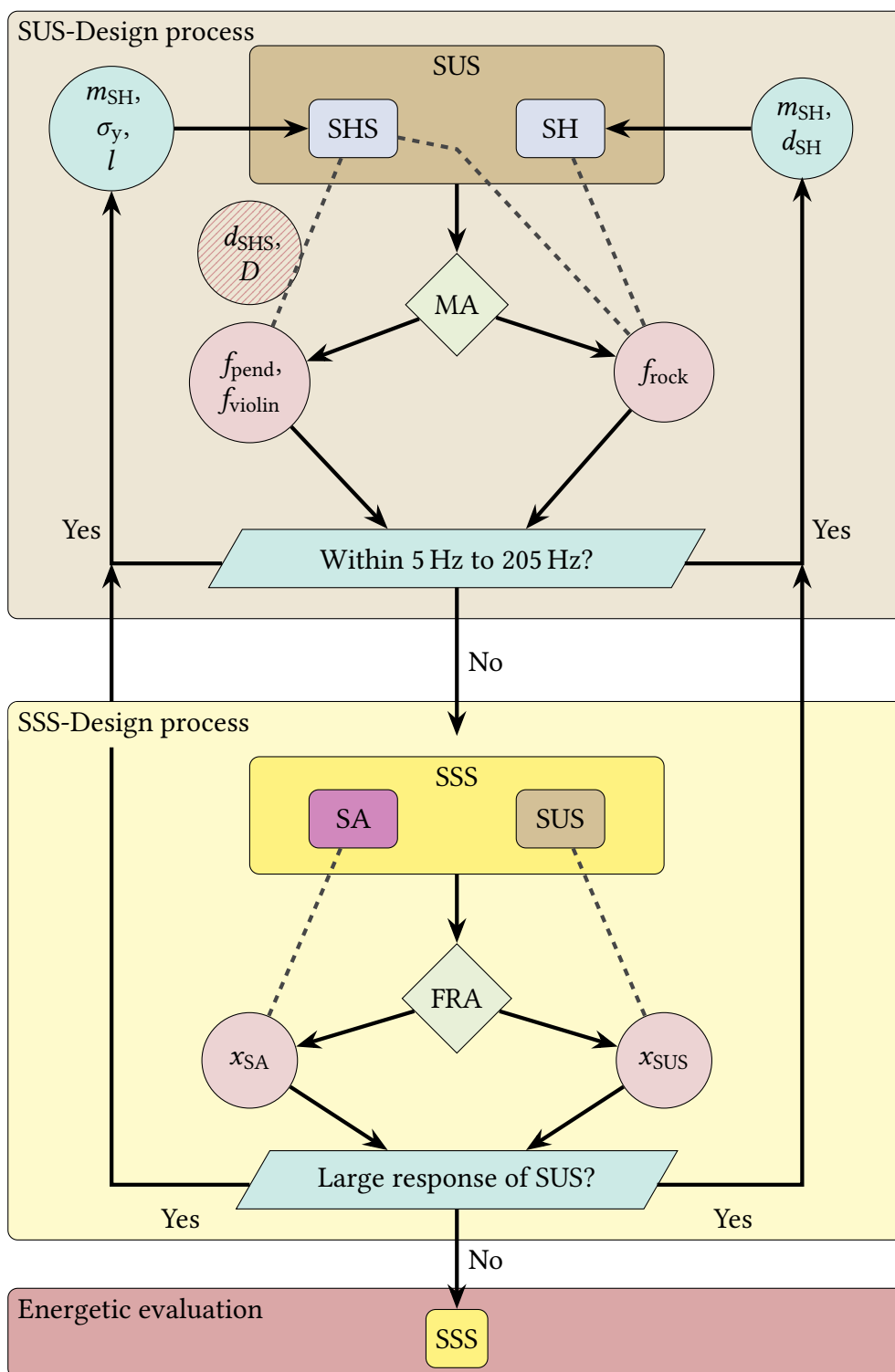


Figure 4.3: Flowchart of the design steps taken for SUS and SSS. Relevant design parameters to the SH and SHS components are depicted in the green circles. The red circles denote the evaluation parameters.

The steps presented in figure 4.3, are a continuation of the the in chapter 3 presented SA analysis in figure 3.3. The MA and FRA of the SA have shown, the SUS needs to be optimised in the frequency range of 5 Hz to 205 Hz. This is reflected in figure 4.3 as the decision criterion for iterating the design step.

In the scope of this work design and evaluation parameters have been defined for the SUS. Figure 4.3 shows the main design parameters of the SHS. These are the mass suspended from the SHS m_{SH} , in this case being the mass of the SH. The yield strength of the deployed material directly influences the diameter of the SHS d_{SHS} , which in turn influences pendulum and violin mode. Additionally the length of the SHS influences has been found influencing f_{pend} and f_{violin} . Additionally to the main evaluation parameters, the SHS design took in to account the dilution factor D presented in section 2.3. Eq. 2.21 shows, D can significantly reduce the loss angle of the pendulum system. Minimising D proposes a feasible starting point for the SHS design.

A potential SUS design candidate is combined with the SA, forming the SSS. A FRA is conducted of the SSS. The evaluation parameters for the FRA hereby are the displacement experienced by the SUS components, compared to the displacement experienced by the SA. In the next step an energetic evaluation of the system is conducted in which the systems loss angle ϕ_{System} is estimated and the performance of the design can be judged.

From eq. 2.20 the diameter d_{SHS} influences D quadratically. Therefore minimising D is accomplished by minimising d_{SHS} . Eq. 2.20 shows a linear dependency on length, hence keeping l_{SHS} as long as possible, reduces D . The d_{SH} can be dimensioned via eq. 2.6 appropriate for a specific loads represented by m_{SH} . Using a $SF = 3$ to eq. 2.6 ensures a sound engineering practice.

Many materials experience embrittlement at lower temperatures [11]. Therefore the ultimate strength at lower temperature is taken into account as well. The tension in the SHS, resulting from the SH, should be well bellow the ultimate strength of the material. Table 4.2 shows the yield strength and Young's moduli for possible candidate materials for the SHS. The aluminium alloy AL-6061 is included due to its low Young's modulus. Commercially pure titanium is included, due to its comparatively high ratio between σ_u and σ_y at low temperatures $\sigma_{u/y}(3\text{ K}) = 1.25$. The other material candidates Ti-6V-4Al ($\sigma_{u/y}(3\text{ K}) = 1.03$), SST 304 cold rolled (CR) ($\sigma_{u/y}(3\text{ K}) = 1.02$) and maraging steel ($\sigma_{u/y}(3\text{ K}) = 1.18$), are included, as candidate materials due to the high σ_y values at 300 K.

Table 4.2: Candidate material characteristics at two different temperatures for the SHS

Material	σ_y / MPa		σ_u / MPa		E / GPa	
	300 K	3 K	300 K	3 K	300 K	3 K
Al 6061	250 [11]	380 [11]	300 [39]	450[39]	72 [11]	75 [11]
Ti Grade 1	400 [11]	1200 [11]	510 [40]	1500 [40]	115 [11]	130 [11]
Ti-6V-4Al	900 [11]	1070 [11]	1010 [11]	1100 [11]	112 [11]	127 [11]
SST 304 (CR)	1000 [11]	1080 [11]	1040 [11]	1100 [11]	210 [11]	225 [11]
Maraging Steel	1000 [41]	1700 [41]	1020 [41]	2000 [41]	168 [42]	171 [42]

Table 4.3: Resulting SHS diameters and dilution factor for potential SH mass cases and SHS lengths for the SHS candidate materials.

Quantity	Al 6061	Ti Grade 1	Ti-6V-4Al	SST304 (CR)	Maraging Steel
5 kg					
d / mm	1.5	1.2	0.8	0.8	0.8
$D_{0.45}$	2.4×10^{-2}	1.9×10^{-2}	8.3×10^{-3}	1×10^{-2}	9.1×10^{-3}
$D_{0.15}$	6.4×10^{-2}	5.0×10^{-2}	2.2×10^{-2}	2.7×10^{-2}	2.4×10^{-2}
10 kg					
d / mm	2.1	1.7	1.1	1.1	1.1
$D_{0.45}$	3.4×10^{-2}	2.7×10^{-2}	1.2×10^{-2}	1.4×10^{-2}	1.3×10^{-2}
$D_{0.15}$	0.1	0.1	3.1×10^{-2}	3.8×10^{-2}	3.4×10^{-2}
15 kg					
d / mm	2.6	2.1	1.4	1.3	1.3
$D_{0.45}$	4.1×10^{-2}	3.3×10^{-2}	1.4×10^{-2}	1.8×10^{-2}	1.6×10^{-2}
$D_{0.15}$	0.1	8.7×10^{-2}	3.8×10^{-2}	4.7×10^{-2}	4.2×10^{-2}
20 kg					
d / mm	3	2.4	1.6	1.5	1.5
$D_{0.45}$	4.8×10^{-2}	3.8×10^{-2}	1.7×10^{-2}	2.0×10^{-2}	1.8×10^{-2}
$D_{0.15}$	0.1	0.1	4.4×10^{-2}	5.4×10^{-2}	4.9×10^{-2}

In order to conservatively dimension the SHS, to withstand the load imposed by the SH, the lower bound $\sigma_y(T = 300 \text{ K})$ are taken. Table 4.3 shows the diameters resulting from different loads: 5 kg, 10 kg, 15 kg and 20 kg, representing different m_{SHS} . Additionally the dilution factors at two different lengths 0.45 m, representing the longest l_{SHS} possible, as shown in section 3.1 and 0.15 m is presented in table 4.3.

D -factors in the order of magnitude 1×10^{-2} are presented in [43]. From table 4.3 it can be seen, the D -factors are within the order of magnitude, typical for suspensions in gravitational wave detector applications. For the application in this work, this scales with a high dilution of the losses caused in the SHS.

Due to their high σ_y -values Ti-6V-4Al, cold rolled SST 304 and maraging steel have the lowest D -factors among the the investigated materials. Maraging steel is not advised to be used in cryogenic applications, as it is highly susceptible to hydrogen embrittlement. Which has been reported to occur even at room temperature with an atmospheric source of the hydrogen [44].

The SHS material is set to be Ti-6V-4Al due to the higher ratio of ultimate to yield strength, compared to cold rolled SST 304, at low temperatures. This ensures a safe operation, when conducting the measurement at cryogenic temperature. The SHS is dimensioned at room temperature with a $SF(T = 300 \text{ K}) = 3$. The yield strength increases at lower temperatures. As the load to the SHS and the diameter sta constant, the resulting safety factor is $SF(T = 3 \text{ K}) = 11$.

4.1.3 Modal Analysis

Figure 4.3 shows, the pendulum and violin modes are the evaluation parameters for the SHS. These modes should not occur in the frequency range of 5 Hz to 205 Hz. A MA, is conducted with varying l_{SHS} , m_{SH} and $d_{\text{SHS}}(m_{\text{SH}})$. The values of f_{pend} and f_{violin} are the results. In the scope of this work, it has been found, that the rocking mode is highly dependent of the diameter of the SH. This is reflected in figure 4.3, which shows the design parameter to f_{rock} is d_{SH} , an additional MA is conducted once l_{SHS} and m_{SHS} have been defined.

The investigated masses are 5 kg, 10 kg, 15 kg and 20 kg. The d_{SHS} are taken from table 4.3 for the Ti-6Al-4V SHS, for each mass. The investigated lengths were 150 mm, 250 mm, 300 mm, 350 mm and 450 mm. Figure 4.4 shows the resulting f_{violin} of the system. Additionally the frequency range in which the SA frequencies are expected, is depicted in red. The f_{pend} value are presented in table 4.4 for different l_{SHS} and m_{SHS} .

Evident from table 4.4 it can be seen that a longer SHS shifts f_{pend} to frequencies. Additionally it can be seen that for heavier masses the pendulum mode decreases at constant l_{SHS} . This is due to the D -factor influencing the natural frequency as presented in [45]. The pendulum modes have been additionally analytically calculated via eq. 2.17. This serves to validate the FEM model and ensures boundary conditions have been set correctly. Eq. 2.17 only depends on the length of the pendulum system. Therefore presents a simplified approach, not taking into account influence of mass on f_{pend} . The differences of frequency between the analytically calculated $f_{\text{pend,ana}}$, vs the $f_{\text{pend,FEM}}$ computed via FEM, are very low at lighter mass $\Delta f_{\text{max}} = 0.3$ Hz. At higher masses these differences increase to $\Delta f_{\text{max}} = 0.5$ Hz.

Deploying a heavier mass is beneficial to shifting the pendulum mode towards lower frequencies. For masses above 10 kg the pendulum modes are within the range of 0.7 Hz to 0.8 Hz for all lengths of the SHS.

Figure 4.4 shows the first violin frequencies for the tested m_{SHS} and tested l_{SHS} . For the SHS lengths set at 350 mm and 450 mm the violin modes occur close to 205 Hz, representing the upper boundary, in which SA frequencies are expected. Therefore the length of the SHS is set to 300 mm for which the SHS violin mode occurs at 280 Hz. As the value of m_{SH}

Table 4.4: FEM and analytically calculated pendulum modes.

l / mm	150	250	300	350	450
	FEM				
$f_{\text{pend},5 \text{ kg}} / \text{Hz}$	1.1	0.9	0.9	0.8	0.7
$f_{\text{pend},10 \text{ kg}} / \text{Hz}$	0.9	0.8	0.8	0.7	0.7
$f_{\text{pend},15 \text{ kg}} / \text{Hz}$	0.8	0.7	0.7	0.7	0.7
$f_{\text{pend},20 \text{ kg}} / \text{Hz}$	0.8	0.7	0.7	0.7	0.6
	Analytical				
$f_{\text{pend,ana}} / \text{Hz}$	1.3	1.0	0.9	0.8	0.7

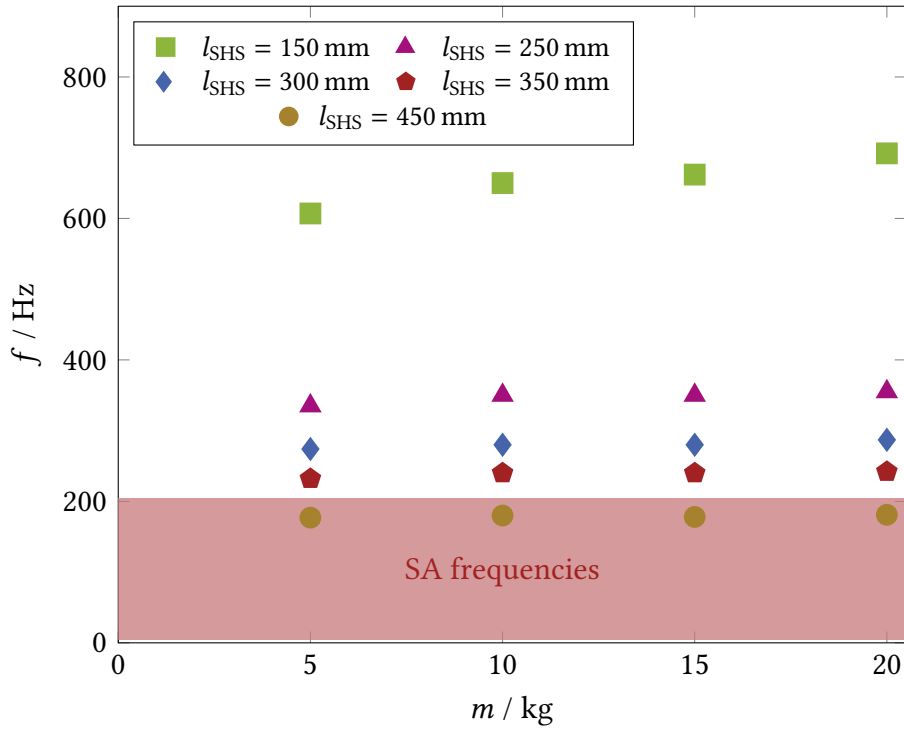


Figure 4.4: Parametric investigation on the violin frequency for various l_{SHS} and different m_{SHS}

does not have a significant influence on the violin mode the m_{SH} is set to 10 kg as a lighter mass keeps the D -factor minimal (see table 4.3). Thus concluding the design of the SHS.

The second component of the SUS is the SH. The SH is designed with regards to the rocking mode. It has been found, increasing the diameter of the SH, decreases the frequency of the rocking mode. Thus d_{SH} , is the design parameter, for reducing f_{rock} . The SH upper block is a tungsten cylinder with a diameter of 120 mm and a height of 20 mm. This results in a mass of $m_{\text{SH,UB}} = 4 \text{ kg}$. A MA with the aim to optimize the design with regards to f_{rock} is conducted. In which d_{SH} are varied to 120 mm, 200 mm and 250 mm. The height h_{SH} is adjusted to yield a $m_{\text{SH,LB}} = 6 \text{ kg}$. Table 4.5 shows resulting f_{rock} for the SH lower block diameters for copper and aluminium as material candidates.

The f_{rock} of copper SH lower block with a $d_{\text{SH}} = 120 \text{ mm}$ is at 7 Hz. This value is within the range 5 Hz to 205 Hz and is therefore excluded from further discussion. For the aluminium SH lower block with the same diameter, f_{rock} occurs at 2.2 Hz. The aluminium design has a larger inertial moment in its z-axis, due to its larger h_{SH} compared to the copper design. This shifts the f_{rock} to lower values as well. All other SH lower block parameter combination yield $f_{\text{rock}} < 3 \text{ Hz}$. And are therefore outside the range of 5 Hz to 205 Hz.

It has been found that the aluminium design, have a superior performance with regards to strain weighted loss angle. The design parameter $d_{\text{SH}} = 200 \text{ mm}$ with $ad_{\text{SH}} = 82 \text{ mm}$. The $d_{\text{SH}} = 250 \text{ mm}$ is omitted, due to a higher material height is beneficial, as it results in

Table 4.5: SUS f_{rock} , for various diameters for $m_{\text{SH}} = 10$ kg using Al and Cu as candidate materials

d / mm	120	200	250
Copper			
h / mm	71	28	19
$f_{\text{rock}} / \text{Hz}$	7.0	2.2	2.0
Aluminium			
h / mm	225	82	53
$f_{\text{rock}} / \text{Hz}$	2.2	2.1	2.0

a higher rigidity of the component. A higher rigidity is especially beneficial, when high mechanical loads are applied to the SA.

Investigating the effect of m_{SH} on the rocking frequency with a constant $d_{\text{SH}} = 200$ mm, has shown in table A.2 having no significant influence on the rocking frequency.

Concluding the MA of the SUS subsystem, a SUS design has been optimised for the frequency range 5 Hz to 205 Hz. The response of SA and SUS are evaluated in a FRA, of the SA and SUS (combined: SSS) together.

4.1.4 Frequency Response Analysis

For the frequency response of the SSS the SUS design, presented in section 4.1.3 and SA are combined. The SA is actuated in the frequency range of 0 Hz to 300 Hz. The SA is actuated by the BL with the same F_{el} used for the SA before in section 3.2.3. Figure 4.3 shows the resulting evaluation parameters of the FRA are the displacements of the SA and SUS.

Figure 4.5 shows the frequency response of the SSS for the HV2 silicon SA. The highlighted points on the geometry next the frequency response plot, shows the points evaluated on the geometries. For the SH the maximal displacement has been found to occur at the outer edge.

As described earlier, the peaks in the frequency response plot indicate the displacement of the system at the given natural frequency. Highlighted are the three sample modes relevant to the Q -measurement. It can be seen that for the second and third mode the displacement response of the SUS, highlighted in blue (SH) and yellow (SHS), is two orders of magnitude lower than the displacement response of the SA, highlighted in red. For the first SA mode the displacement response of the SA is $x_{\text{SA}} = 1.1 \mu\text{m}$. The displacement of the SUS is at $x_{\text{SA}} = 0.5 \mu\text{m}$. The displacement responses of the SUS and SA are close in proximity. This suggests a large response of the SUS at f_{SA} . Figure 4.6 shows the SSS displacement contours of the first three SA modes. A large displacement of the SUS can be seen, when actuating the samples first mode. This is attributed to, the rocking and sample mode overlapping. The frequencies are in close proximity $f_{\text{rock}} = 2$ Hz and $f_{\text{SA}} = 5$ Hz. The effect of overlapping of rocking and sample mode can be seen for all sample types and both HV geometries, presented in A.5 to A.9.

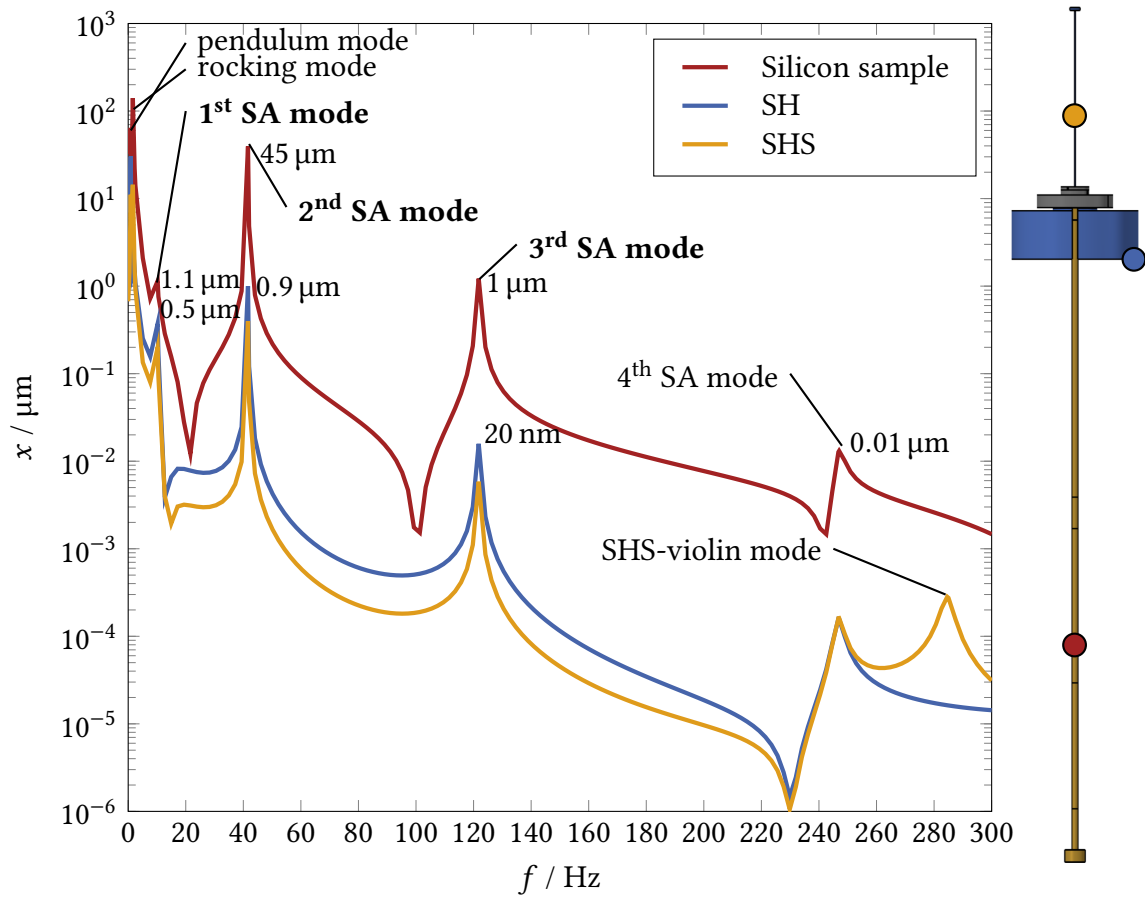


Figure 4.5: FRA of SSS with as HV2 silicon SA actuated at the highlighted red spot.

A large displacement of the SUS is to be avoided, as relatively large elastic deformation of the SUS cause the strain weighted loss to increase. For the second and third sample modes the response of the SUS can be seen to be two orders of magnitudes lower compared to the SA displacement.

Additionally to the highlighted first three sample modes, it can be seen figure 4.5 depicts the fourth sample mode occurring at ca. 250 Hz. Due to the small displacement of $0.01 \mu\text{m}$ the $f_{SA,4}$ is below the assumed sensitivity of the detection system, at $1 \mu\text{m}$. The SHS violin mode is represented by the peak of the yellow line at 285 Hz. This work has shown that, the SHS violin mode, does not overlap with any of the frequencies relevant to the Q -measurement. The third mode of the sapphire HV1 SA has the highest value for $f_{SA,sapphire,3}=205 \text{ Hz}$. The FRA of this SA is depicted in figure A.8, which shows the SUS displacement response is two orders of magnitude lower, compared to the displacement response of the SA.

The FRA of the merged subsystems SUS and SA, the SSS response plots can be used, to estimate for which modes the strain weighted loss angles of the SUS might be elevated. Due to the large displacement of the SUS at $f_{SA,1}$ the strain weighted loss angle is expected to be high. For $f_{SA,2}$ and $f_{SA,3}$, the displacement of the SUS is very low. Therefore the

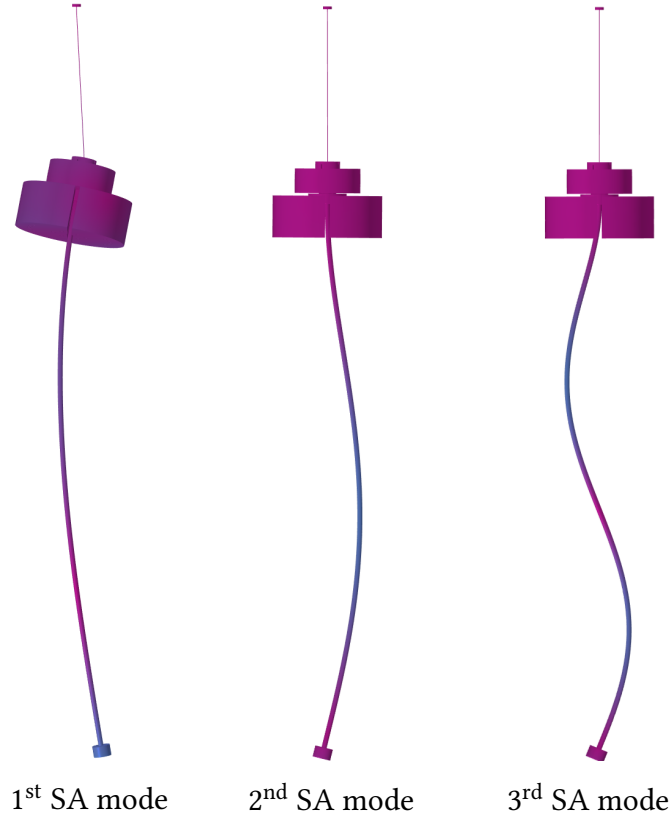


Figure 4.6: Response contours of the SSS at the three natural frequencies, relevant to the Q -measurement

expected loss angle are expected to be low as well. These estimations require detailed validation, presented in the following section.

4.1.5 Energetic Evaluation

As figure 4.3 depicted, after the definition of a suitable SSS candidate design, with regards to MA and FRA, the next step is an energetic evaluation of the system. The energetic evaluation includes the calculation of the integral strain energy of each component, as shown in eq. 2.14 and the strain weighted loss angle of each component, eq. 2.15.

The energetic evaluation process is visualised in figure 4.7. The SA is actuated at relevant frequencies f_{SA} for the Q -measurement. The integral strain ratios of the SSS components are calculated via the FEM model. The SSS achievable loss angle can be calculated by summation of the strain weighted loss angles, as presented in eq. 4.1.

$$\underbrace{\phi_{SA} U_{SA/SSS}}_{\hat{\phi}_{intrinsic}} + \underbrace{D\phi_{SHS} U_{SHS/SSS} + \phi_{SH} U_{SH/SSS}}_{\hat{\phi}_{extrinsic}} = \phi_{SSS} \quad (4.1)$$

Table 4.6 shows the integral strain ratios $U_{i/SSS}$ of each component for each sample types and both HV geometries investigated in this work. From table 4.6 it can be seen that $U_{SH,UB}$

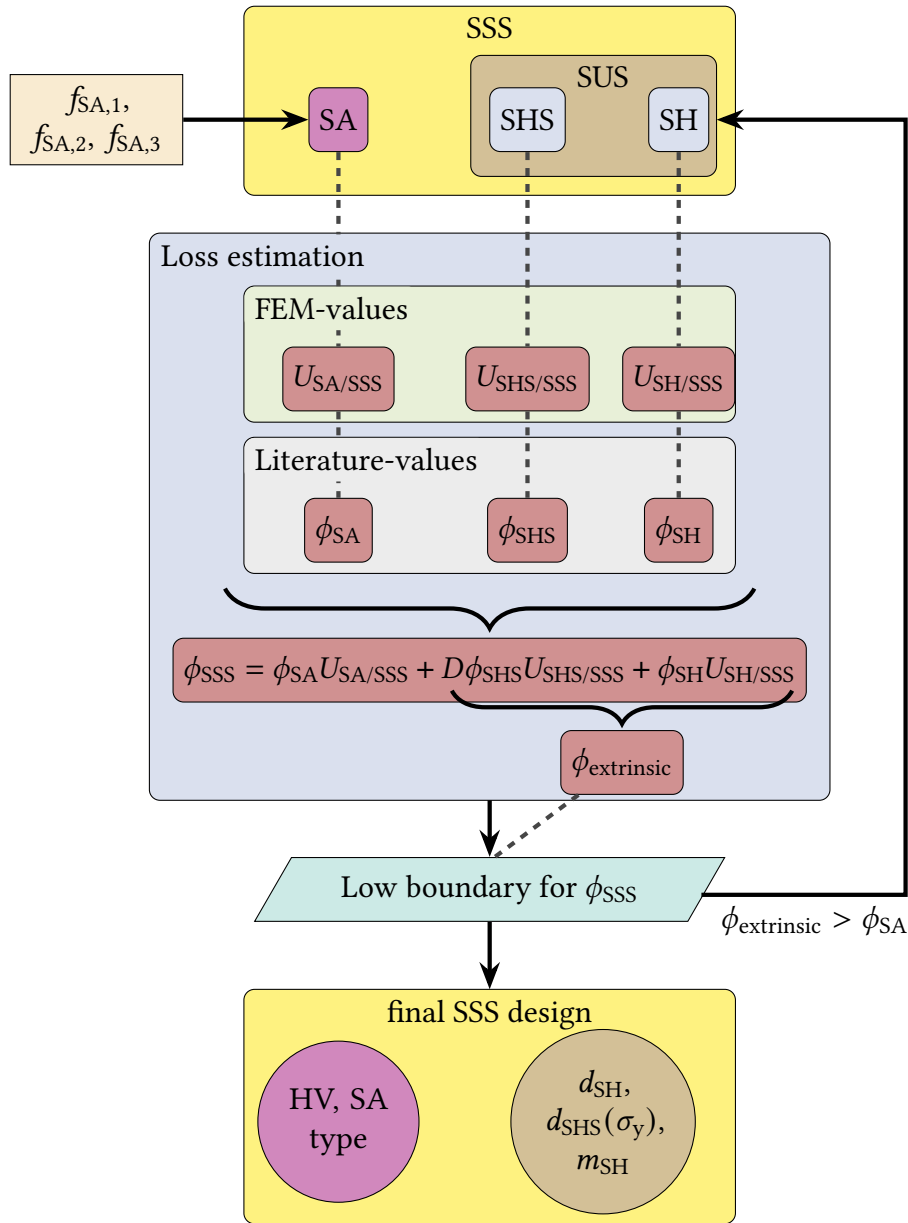


Figure 4.7: Flowchart of the followed steps for the energetic evaluation

is one order of magnitude lower, for the SSS designs using HV2 compared to SSS designs using HV1. This relation is true for all sample types included in this work. This large difference can be explained by investigating the strain density in both HV geometries. Figure 4.8 shows the strain density at $f_{SA,3}$ for both HV designs. For comparability, the samples were actuated to yield the same displacement of $x_{SA} = 1 \mu\text{m}$. It can be seen, that strain density is highly concentrated around areas, where high elastic deformation of the SA occurs. Zooming in on the sample heads in figure 4.8, it can be seen that strain density is highly concentrated around the area where the sample body attaches to the sample head. The HV1 geometry exhibits a higher strain density at the saddle, compared to the HV2 geometry. The increase in strain, for the HV1 SA facilitates energy transfer from the SA

Table 4.6: Integral strain energy ratios for the SSS components.

SA natural frequency / Hz	$U_{SHS/SSS}$	$U_{SH,UB/SSS}$	$U_{SH,LB/SSS}$	$U_{SA/SSS}$
Silicon (HV1)				
11 ($f_{SA,1}$)	0.23 %	0.03 %	6×10^{-3} %	99.74 %
51 ($f_{SA,2}$)	1×10^{-3} %	0.04 %	7×10^{-3} %	99.95 %
141 ($f_{SA,3}$)	1×10^{-4} %	0.04 %	7×10^{-3} %	99.95 %
Silicon (HV2)				
11 ($f_{SA,1}$)	0.39 %	1×10^{-3} %	2×10^{-3} %	99.61 %
41 ($f_{SA,2}$)	2×10^{-3} %	1×10^{-3} %	3×10^{-3} %	99.99 %
121 ($f_{SA,3}$)	3×10^{-5} %	1×10^{-3} %	4×10^{-3} %	99.99 %
Sapphire sample (HV1)				
17 ($f_{SA,1}$)	0.1 %	0.12 %	0.01 %	98.78 %
73 ($f_{SA,2}$)	1×10^{-3} %	0.16 %	0.01 %	99.83 %
203 ($f_{SA,3}$)	3×10^{-4} %	0.15 %	0.01 %	99.84 %
Sapphire sample (HV2)				
17 ($f_{SA,1}$)	0.15 %	0.01 %	4×10^{-3} %	99.84 %
61 ($f_{SA,2}$)	1×10^{-3} %	0.01 %	7×10^{-3} %	99.98 %
176 ($f_{SA,3}$)	1×10^{-4} %	0.01 %	8×10^{-3} %	99.98 %
Suspension Tube (HV1)				
9 ($f_{SA,1}$)	0.23 %	0.02 %	4×10^{-3} %	98.74 %
49 ($f_{SA,2}$)	3×10^{-4} %	0.02 %	4×10^{-3} %	99.98 %
137 ($f_{SA,3}$)	4×10^{-5} %	0.02 %	4×10^{-3} %	99.97 %
Suspension Tube (HV2)				
7 ($f_{SA,1}$)	0.42 %	3×10^{-4} %	2×10^{-4} %	98.58 %
39 ($f_{SA,2}$)	1×10^{-3} %	2×10^{-3} %	1×10^{-3} %	99.99 %
121 ($f_{SA,3}$)	2×10^{-5} %	2×10^{-3} %	1×10^{-3} %	99.99 %

Table 4.7: Bulk losses for each component in the SSS assumed in this work.

Material	ϕ_{bulk}	Material	ϕ_{bulk}
Sapphire	1×10^{-8} [46]	Ti-6Al-4V	1×10^{-4} [47]
Silicon	1×10^{-8} [6]	Al-6061	1×10^{-6} [48]
Titanium	1×10^{-6} [6]	Tungsten	1×10^{-6} [49]

to the SH. This causes $U_{SH,UB}$ to be elevated in SSS design utilising the HV1 SA, compared to HV2 SA.

Using the integral strain ratio values presented in table 4.6 the strain weighted loss angle for each component of the SSS can be calculated. Eq. 4.1 shows the summation of all

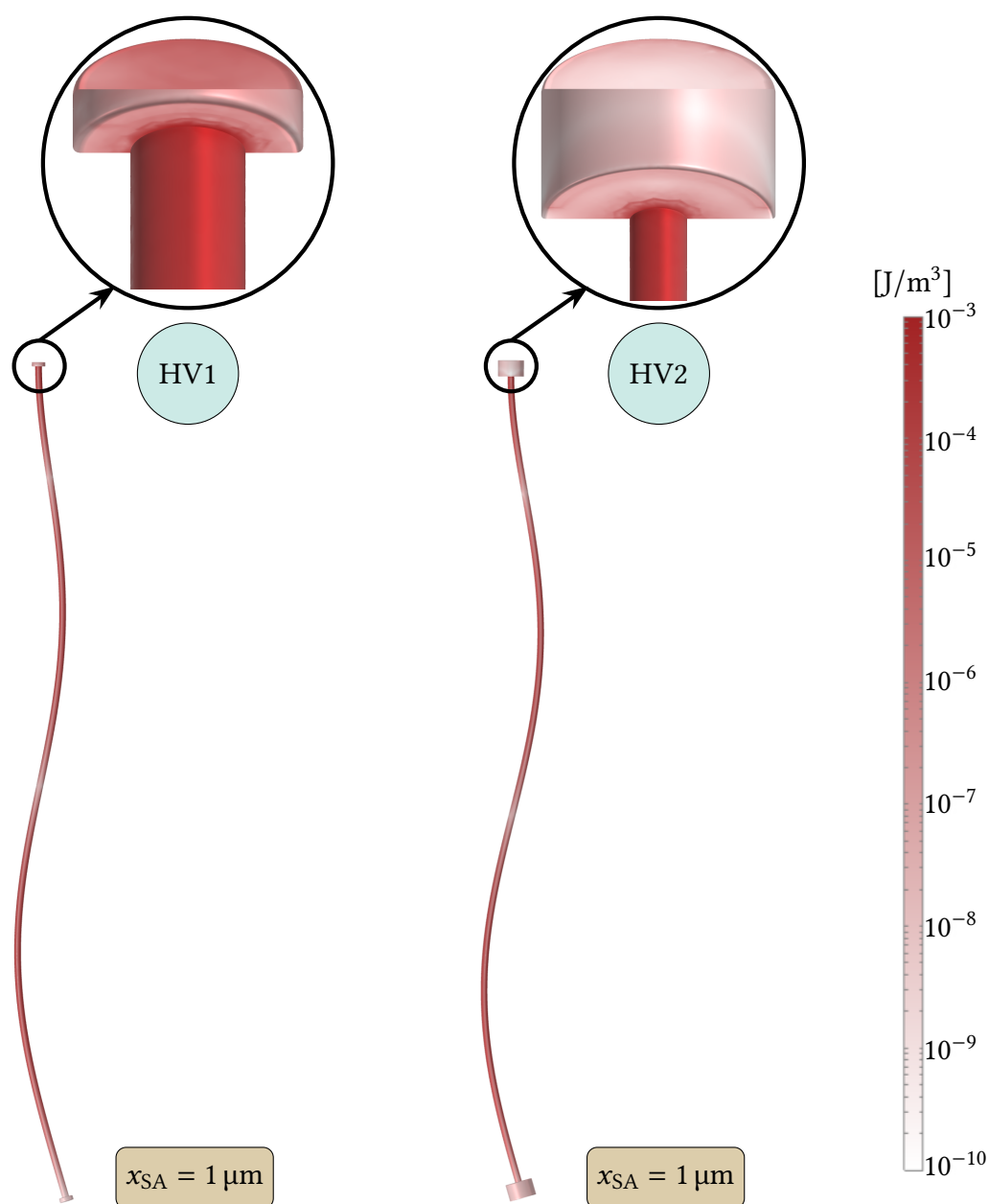


Figure 4.8: Strain density distribution along the SA HV1 and HV2 at $f_{SA,3}$. The zoomed in portion, shows a section view of the inner surface of the head, in order to visualise the strain density gradient at the saddle.

strain weighted loss angles yields the loss angle of the SSS ϕ_{SSS} . The bulk losses for each material deployed in the SSS are presented in table 4.7.

Certain extrinsic factors cannot be modeled and are therefore not included in the model. These include the loss angle contributions to the overall extrinsic losses, such as losses caused by joining, friction or pretension cause by bolts in the SH.

Eq. 2.8 shows contributing factors to the intrinsic loss angle of a component. For the SH the surface and thermoelastic contributions are not expected to be the major contributor.

Therefore the calculation of strain weighted loss angle, is limited to measured values of bulk losses. For the SH upper block, table 4.6 shows an elevated integral strain ratio. Meaning a low loss material should be deployed for this component. Tungsten was chosen for the SH upper block, due to its low bulk loss angle. Tungsten has a reported bulk loss angle of $\phi_{\text{Tungsten}} \approx 1 \times 10^{-7}$ [49]. However due to relatively large uncertainties in the measurements, a conservative $\phi_{\text{Tungsten}} = 1 \times 10^{-6}$ is used to calculate the strain weighted loss angles. The aluminium SH lower block is also a low loss material reflected in its $\phi_{\text{bulk}} = 1 \times 10^{-6}$.

For the SA the surface contribution to the loss angle are expected to be relevant. However these cannot be sufficiently modeled as they are not fully understood [50] and are therefore excluded from the model. The thermoelastic contribution to the loss angle, is excluded

Table 4.8: Strain weighted loss angles for each component and low boundary of SSS loss angles.

SA natural frequency / Hz	$D\hat{\phi}_{\text{SHS}}$	$\hat{\phi}_{\text{SH}}$	$\hat{\phi}_{\text{SA}}$	$\Sigma\phi_{\text{SSS}}$
Silicon (HV1)				
11 ($f_{\text{SA},1}$)	1.6×10^{-8}	3.6×10^{-10}	1.0×10^{-8}	3.3×10^{-8}
51 ($f_{\text{SA},2}$)	3.2×10^{-10}	5.0×10^{-10}	1.0×10^{-8}	1.0×10^{-8}
141 ($f_{\text{SA},3}$)	8.9×10^{-11}	4.7×10^{-10}	1×10^{-8}	1.0×10^{-8}
Silicon (HV2)				
11 ($f_{\text{SA},1}$)	7.9×10^{-9}	3.0×10^{-11}	1.0×10^{-8}	1.8×10^{-8}
41 ($f_{\text{SA},2}$)	1.8×10^{-10}	4.0×10^{-11}	1.0×10^{-8}	1.0×10^{-8}
121 ($f_{\text{SA},3}$)	7.9×10^{-12}	5.0×10^{-11}	1.0×10^{-8}	1.0×10^{-8}
Sapphire (HV1)				
17 ($f_{\text{SA},1}$)	1.1×10^{-8}	1.3×10^{-9}	1.0×10^{-8}	2.2×10^{-8}
73 ($f_{\text{SA},2}$)	4.1×10^{-10}	1.7×10^{-9}	1.0×10^{-8}	1.4×10^{-8}
203 ($f_{\text{SA},3}$)	3.4×10^{-10}	1.6×10^{-9}	1.0×10^{-8}	1.0×10^{-8}
Sapphire (HV2)				
17 ($f_{\text{SA},1}$)	1.6×10^{-8}	1.4×10^{-10}	1.0×10^{-8}	2.6×10^{-8}
61 ($f_{\text{SA},2}$)	3.7×10^{-10}	2.0×10^{-10}	1.0×10^{-8}	1.0×10^{-8}
176 ($f_{\text{SA},3}$)	1.1×10^{-10}	2.0×10^{-10}	1.0×10^{-8}	1.0×10^{-8}
Suspension Tube (HV1)				
9 ($f_{\text{SA},1}$)	1.3×10^{-8}	2.4×10^{-10}	1.0×10^{-6}	1.0×10^{-6}
49 ($f_{\text{SA},2}$)	2.5×10^{-10}	2.4×10^{-10}	1.0×10^{-6}	1.0×10^{-6}
137 ($f_{\text{SA},3}$)	3.4×10^{-11}	2.4×10^{-10}	1.0×10^{-6}	1.0×10^{-6}
Suspension Tube (HV2)				
7 ($f_{\text{SA},1}$)	1.8×10^{-8}	5.0×10^{-12}	1.0×10^{-6}	1.0×10^{-6}
39 ($f_{\text{SA},2}$)	2.5×10^{-9}	3.0×10^{-11}	1.0×10^{-6}	1.0×10^{-6}
121 ($f_{\text{SA},3}$)	1.6×10^{-10}	3.0×10^{-11}	1.0×10^{-6}	1.0×10^{-6}

from this investigation, due to the lack of tension in the SA. Assuming only the bulk losses gives a conservative specification for the ϕ_{SA} .

As described in section 2.2 the thermoelastic loss can be modeled for circular suspensions by eq. 2.9 and eq. 2.10. Hence the thermoelastic contribution to the loss angle of the SHS $\phi_{\text{therm,SHS}}$ have been considered to the strain weighted loss calculation. The thermoelastic loss have been calculated via eq. 2.9 and 2.10. The relevant material data to calculate the $\phi_{\text{therm,SHS}}$ are given in table A.7 and the values for $\phi_{\text{therm,SHS}}$ are listed in table A.8. Furthermore as the SUS is configured as a pendulum system the dilution factor $D = 0.016$ is taken in to account via eq. 2.21. This reduces the effective loss angle caused by the SHS material.

Table 4.8 presents the strain weighted loss angles $\hat{\phi}$ of each component and the lower bound loss angle achievable of the system ϕ_{SSS} . Using the lower bound of ϕ_{SSS} conclusions of the SSS design can be drawn. As the objective of the measurement campaign is to measure the loss angle of the sample, the systems $\phi_{\text{extrinsic}}$ should not exceed ϕ_{SA} . Certain loss angle measurements might be excluded of the measurement campaign, due to $\phi_{\text{extrinsic}}$ exceeding ϕ_{SA} .

For the suspension tube sample (HV1 and HV2), table 4.8 shows that loss measurement for all f_{SA} , are possible. This is due to $\phi_{\text{extrinsic}}$ being two orders of magnitude lower than $\phi_{SA, \text{Suspension tube}}$ at $f_{SA,1}$ and four orders of magnitudes lower at $f_{SA,3}$.

For the monolithic suspension fibre samples (HV1 and HV2) at $f_{SA,1}$ summation of the strain weighted loss angle has shown, $\phi_{\text{extrinsic}}$ being in the same order of magnitude as ϕ_{SA} . This is attributed to the strain weighted loss angle for the SHS dominating the systems loss angle. Which is reflected in the FRA. The figures 4.5 and 4.6, showing $f_{SUS, \text{rocking}}$ overlapping with $f_{SA,1}$.

For HV1 monolithic suspension fibres, at $f_{SA,2}$, it can be seen that the strain weighted loss angles for SH are by a factor of two higher than the strain weighted loss angles of the SHS. For HV2 monolithic suspension fibres it can be seen that the strain weighted loss angles of the SH become one order of magnitude lower than the SHS. Thus $\phi_{\text{extrinsic}}$ are limited by the SHS strain weighted loss angles for HV2 based SSS designs.

For $f_{SA,3}$ utilising HV1 based SSS designs for a silicon SA $\phi_{\text{extrinsic}}$ are by two orders of magnitude lower than the ϕ_{SA} . For sapphire SA $\phi_{\text{extrinsic}}$ are by one order of magnitude lower than ϕ_{SA} . Utilising the HV 2 designs, the silicon SA are three orders of magnitude lower than ϕ_{SA} and sapphire SA $\phi_{\text{extrinsic}}$ are two order of magnitude lower than ϕ_{SA} .

Concluding the loss estimation of the entire system, via the proposed method by eq. 4.1, shows for suspension tube samples all modes in all configuration are not limited by the dissipation of the SSS. For monolithic suspension fibres, it can be concluded that the Q -measurements cannot be conducted for $f_{SA,1}$. Due to $\phi_{\text{extrinsic}}$ being in the same order of magnitude as ϕ_{SA} . For both head variants monolithic suspension fibres, the second and third mode can be measured. With $\phi_{\text{extrinsic, HV1}}$ being one order of magnitude lower than ϕ_{SA} and $\phi_{\text{extrinsic, HV2}}$ being two orders of magnitude lower compared to ϕ_{SA} . Therefore the HV2 SA based SSS design proposes a design with a larger safety margin. The clamping losses cannot be sufficiently modeled and are reported to be the main limiting factor for Q -measurements [8, 24]. Therefore the transfer of strain energy can be minimised by deploying a larger head.

4.1.6 Improving Extrinsic Loss Angle for Low Frequency Measurements

In the scope of this work efforts have been made to improve the measurability of the first sample mode. This is accomplished by attaching the cage, which is housing instrumentation relevant for the Q -measurement, directly to the SH, as depicted in figure 4.9. This causes the centre of mass of the SUS to shift down in the z -axis, resulting in a stabilising effect on the SUS. This prevents the SUS rocking mode overlapping with the first SA mode. The cage is made of aluminium and adds an additional 14 kg to the SH ($m_{SH} = 10$ kg). The SHS diameter is adjusted to $d_{SHS} = 1.6$ mm. The investigation has been limited to a silicon HV2 SA.

The performance of the SSS composition depicted in figure 4.9 is judged by energetic evaluation and loss estimation of ϕ_{SSS} . The integral strain ratios at $f_{SA,1}$, $f_{SA,2}$ and $f_{SA,3}$ of each component are presented in table 4.9.

It can be seen that attaching the cage to the SH, decreases the integral strain energy ratio $U_{SHS/SSS}$, by two orders of magnitude compared to the values presented in table 4.6, for the case where the cage is not attached to the SH. Additionally $U_{SHS/SSS}$ is reduced by two orders of magnitude at $f_{SA,2}$ and $f_{SA,3}$. This is attributed to the cage absorbing parts of the energy, preventing energy transferred from the SA to the SHS.

For the component SH at $f_{SA,2}$ and $f_{SA,3}$ the addition of the cage increases the ratio $U_{SH/SSS}$ by a factor of ca. 6, compared to the SSS composition without the cage attached shown in table 4.6. The additional energetic contribution arises from the pretension caused by the cage, pulling on the SH. The static load leads to initial elastic deformation of the SH. This increases when the SA is vibrating at f_{SA} .

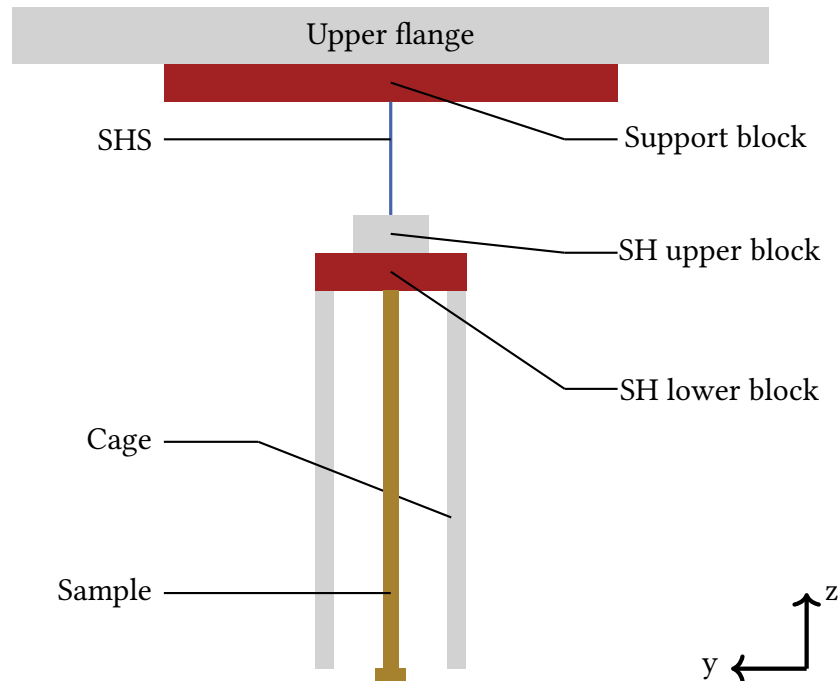


Figure 4.9: Detailed schematic of the general SSS geometry, with cage attached to the SUS

Table 4.9: Integral strain energy ratios in Silicon HV2 samples with the cage attached to the SH.

f_{SA} / Hz	$U_{SHS/SSS}$	$U_{SH,UB/SSS}$	$U_{SH,LB/SSS}$	$U_{cage/SSS}$	$U_{SA/SSS}$
6	$7 \times 10^{-4} \%$	$3 \times 10^{-3} \%$	$6 \times 10^{-3} \%$	0.01 %	99.98 %
41	$2 \times 10^{-5} \%$	$2 \times 10^{-3} \%$	$5 \times 10^{-3} \%$	0.01 %	99.98 %
121	$1 \times 10^{-5} \%$	$1 \times 10^{-3} \%$	$5 \times 10^{-3} \%$	0.01 %	99.98 %

Table 4.10: strain weighted loss angles for a HV2 silicon sample with cage attached to the SH

f_{SA} / Hz	$D\hat{\phi}_{SHS}$	$\hat{\phi}_{SH}$	$\hat{\phi}_{cage}$	$\hat{\phi}_{SA}$	$\Sigma\phi_{SSS}$
6	3×10^{-10}	9×10^{-11}	1×10^{-10}	1×10^{-8}	1×10^{-8}
41	4×10^{-11}	7×10^{-11}	1×10^{-10}	1×10^{-8}	1×10^{-8}
121	2×10^{-11}	6×10^{-11}	1×10^{-10}	1×10^{-8}	1×10^{-8}

For the cage, becomes the main contributor to the integral strain ratio of the system, besides the SA. Therefore deploying a material, which has a low bulk loss angle, such as aluminium $\phi_{Al-6061} = 1 \times 10^{-6}$, is beneficial, keeping the strain weighted losses low.

By calculating the strain weighted loss angles of each component a lower bound for the systems loss angle ϕ_{SSS} is estimated. By summation of the strain weighted loss angles of all components, as shown in eq. 4.8 with an additional term including the strain weighted loss angle of the cage. For the components SA, SH and cage the bulk loss angles presented in table 4.7 are assumed. For the SHS $\phi_{therm,SHS}$ have been modeled as well. The values for $\phi_{therm,SHS}$ are presented in table 4.10. Additionally the dilution factor of $D = 0.02$ has been deployed, as the SUS is a pendulum system.

From table 4.10 it can be seen attaching the cage to the SH for $f_{SA,1}$, $\phi_{extrinsic}$ being two orders of magnitude lower than ϕ_{SA} . This proposes a reduction of $\phi_{extrinsic}$ of two orders of magnitude, compared to the $\phi_{extrinsic}$ presented in table 4.8.

At the frequencies $f_{SA,2}$ and $f_{SA,3}$, it can be seen, that the $\phi_{extrinsic}$ are dominated by the cage. This is attributed to the relatively high integral strain energy ratio of the cage. The $\phi_{extrinsic}$ are by two orders of magnitude lower, compared to the SA. Comparing this, to the $\phi_{extrinsic}$ of the previously SSS design, presented table 4.8. The lowest achievable $\phi_{extrinsic}$ is 3 orders of magnitudes lower than ϕ_{SA} . Hence the cage increases $\phi_{extrinsic}$ unnecessarily for $f_{SA,2}$ and $f_{SA,3}$.

Concluding the efforts to improve the measurability of the first mode, has shown, attaching the cage to the SH reduces the lower bound of loss angle of the system at $f_{SA,1}$. For the Q -measurements conducted at $f_{SA,2}$ and $f_{SA,3}$, the addition of the cage increases $\phi_{extrinsic}$. Therefore the design will include holes on the outer part of the SH, allowing to attach the cage to the SH when measurements at $f_{SA,1}$, are conducted.

The determined design parameters of the entire SSS for supporting an unloaded SA is summarised in table A.4.

4.2 Setup Design for Loaded Sample Case

As described in section 3, one of the stated objectives of the test facility is, to investigate the Q -factor under mechanical load. The goal for the SSS design hereby is, to maximise comparability of measurements conducted without a mechanical load applied to the SA, presented in section 4.1 to measurements conducted with a mechanical load applied to the SA. Consequently the same SH design as used for the unloaded case, presented in subsection 4.1 to the sample is implemented. The SHS diameter d_{SHS} is adjusted for each load case. Due to the increase in d_{SHS} the SHS violin modes $f_{\text{SHS-violin}}$ shift towards higher values, which could be seen in figure 4.4.

The investigation of different load cases have been limited to HV2 samples and follows the key steps of MA, FRA, energetic evaluation and subsequent loss estimation for the total system. The investigated masses are 10 kg, 100 kg and 400 kg. A tungsten mass is suspended from the SA. The SSS results in being a double pendulum system. The SHS and SH compose the first pendulum stage and the SA and load mass, compose the second pendulum stage. The suspension of mass from the SA implies additional characteristic modes, which are depicted in figure A.11.

Relevant for the Q -factor measurements are the violin modes of the sample. Due to being the modes, where the majority of the energy is dissipated via the sample alone. Table 4.11 presents the values of the first two $f_{\text{SA,violin}}$ under the applied mechanical loads of 10 kg, 100 kg and 400 kg. It can be seen, the tension increasing in the SA, the $f_{\text{SA,violin}}$ shift to higher values.

The mode shapes of the first $f_{\text{SA,violin}}$ are presented in figure 4.10. Analysing the mode shapes, the placement of the BL BC and the frequency response evaluation point for the FRA can be decided. The placement is chosen in a point, where the displacement of the SA, is sufficiently large, across all modes. This is found at ca. 0.7 m along the samples length.

The SSS FRA is conducted to define, which the relevant natural frequencies are for the Q -measurement. This is decided on the basis of the assumed sensitivity, of the detection sensor being 1 μm . The actuation sinusoidal force for the FRA is the aforementioned F_{el} ,

Table 4.11: SA violin modes for the different SA types

Mode number	Silicon	Sapphire	Suspension Tube
$m_{\text{suspended}} = 10 \text{ kg}, d_{\text{SHS}} = 1.5 \text{ mm}$			
1 st / Hz	57	82	62
2 nd / Hz	149	213	160
$m_{\text{suspended}} = 100 \text{ kg}, d_{\text{SHS}} = 3.5 \text{ mm}$			
1 st / Hz	73	87	99
2 nd / Hz	176	223	221
$m_{\text{suspended}} = 400 \text{ kg}, d_{\text{SHS}} = 6.8 \text{ mm}$			
1 st / Hz	113	110	170
2 nd / Hz	243	258	352

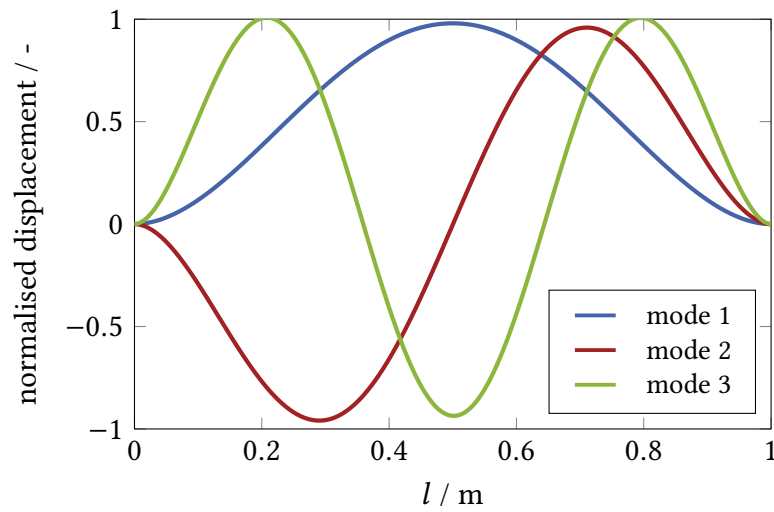


Figure 4.10: SA-violin mode shapes under load

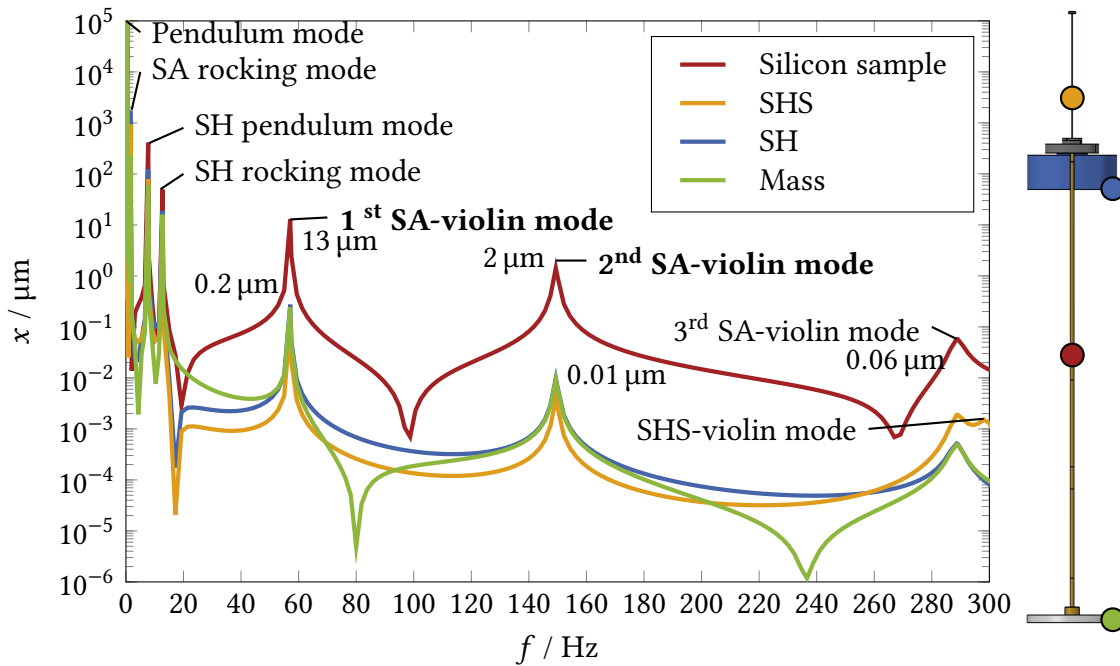


Figure 4.11: FRA of a SSS with the mechanical load suspended for a silicon sample:10 kg

which is calculated with the values, given in table 3.4 and implemented as the BL BC. The FRA for a silicon SA with a load mass of 10 kg, is depicted in figure 4.11. Highlighted are the evaluated point for each component of the SSS.

The displacement response investigation concludes, the samples first two violin modes are relevant to Q - measurements. At $f_{SA,violin,1}$ and $f_{SA,violin,2}$ it can be seen that the SUS and load mass have a displacement response, which is two orders of magnitude lower, compared to the SA displacement response. Investigation of the higher load masses have shown similar relations.

On the basis of the MA and FRA, an energetic evaluation of the SSS with the different load masses is conducted. The integral strain ratios of each component of the system are presented in table 4.12, for all load cases for a HV2 silicon sample. For the suspension tube and sapphire SA the integral strain ratios of each SSS component are presented in A.6 and A.5, respectively.

Table 4.12 shows the mass being the main contributor to the elastic energy in the SSS, besides the SA. In order to prevent a high dissipation at the clamping point of the mass, the material chosen is tungsten, which has a relatively low bulk loss value, of $\phi_{\text{Tungsten}} = 1 \times 10^{-6}$. Furthermore it can be seen that $U_{\text{SH,UB/SSS}}$ increase toward higher masses. The tension in the SA caused by the load mass, causes the sample to have an initial elastic deformation. The strain accumulates at the two end of the SA, which leads to a higher energy transfer to the SH, raising the value of $U_{\text{SH,UB/SSS}}$.

The strain weighted loss angles are calculated assuming bulk losses for the components SA, SH and load mass. The values are presented in table 4.7. Using the bulk loss mass for the SA, serves as a conservative estimation. Due to the tension caused by the load mass, the thermoelastic contribution of the SA is expected to increase. However this is not included in this model, as optimising in regards to bulk losses, presents a conservative design approach.

For the SHS $\phi_{\text{therm,SHS}}$ is taken into account, using the values presented in table A.9. For the SUS, which is the first pendulum stage of the double pendulum system, the dilution factors depend on the load of the system and are multiplied to the strain weighted losses with, $D(10 \text{ kg}) = 0.02$, $D(100 \text{ kg}) = 0.05$ and $D(400 \text{ kg}) = 0.1$. Summation of the strain weighted loss angles of each component yields the lower bound of ϕ_{SSS} . By determining the $\phi_{\text{extrinsic}}$, load cases for which $\phi_{\text{extrinsic}}$ exceed ϕ_{SA} are omitted.

From table 4.13 it can be seen, that for higher mechanical loads $\phi_{\text{extrinsic}}$ increases. The main contributor to $\phi_{\text{extrinsic}}$, is the SHS of the system. This is attributed to two reasons. First, the energy contribution $U_{\text{SHS/SSS}}$ of the SHS increases at higher loads, reflected in table 4.12. The second reason being the $\phi_{\text{therm,SHS}}$ increasing at higher loads. Eq. 2.9 shows

Table 4.12: Integral strain energy ratios in Silicon HV2 samples under the mechanical load of 10 kg, 100 kg and 400 kg.

$f_{\text{SA}} / \text{Hz}$	$U_{\text{SHS/SSS}}$	$U_{\text{SH,UB/SSS}}$	$U_{\text{SH,LB/SSS}}$	$U_{\text{mass/SSS}}$	$U_{\text{SA/SSS}}$
10kg					
57 Hz	$1 \times 10^{-3} \%$	$3 \times 10^{-3} \%$	$4 \times 10^{-3} \%$	0.02 %	99.98 %
149 Hz	$3 \times 10^{-5} \%$	$2 \times 10^{-3} \%$	$4 \times 10^{-3} \%$	0.02 %	99.97 %
100kg					
73 Hz	$9 \times 10^{-3} \%$	$3 \times 10^{-3} \%$	$6 \times 10^{-3} \%$	0.01 %	99.98 %
175 Hz	$2 \times 10^{-4} \%$	$2 \times 10^{-3} \%$	$5 \times 10^{-3} \%$	0.01 %	99.98 %
400kg					
112 Hz	0.02 %	$6 \times 10^{-3} \%$	0.01 %	0.02 %	99.94 %
243 Hz	$7 \times 10^{-4} \%$	$4 \times 10^{-3} \%$	$9 \times 10^{-4} \%$	0.02 %	99.97 %

Table 4.13: Strain weighted loss angles for all SA types, with the investigated load masses, 10 kg, 100 kg and 400 kg

f_{SA} / Hz	$D\hat{\phi}_{SHS}$	$\hat{\phi}_{SH}$	$\hat{\phi}_{mass}$	$\hat{\phi}_{SA}$	$\Sigma\phi_{SSS}$
Silicon					
10kg					
57	1×10^{-9}	7×10^{-11}	2×10^{-10}	1×10^{-8}	1.1×10^{-8}
149	6×10^{-11}	7×10^{-11}	2×10^{-10}	1×10^{-8}	1×10^{-8}
100kg					
73	1×10^{-7}	9×10^{-11}	9×10^{-11}	1×10^{-8}	1×10^{-7}
175	6×10^{-9}	7×10^{-11}	9×10^{-11}	1×10^{-8}	1.6×10^{-8}
400kg					
112	3×10^{-6}	2×10^{-10}	2×10^{-10}	1×10^{-8}	3×10^{-6}
243	1×10^{-7}	5×10^{-11}	1×10^{-10}	1×10^{-8}	1.1×10^{-7}
Sapphire					
10kg					
82	1×10^{-9}	2×10^{-10}	5×10^{-10}	1×10^{-8}	1.1×10^{-8}
212	2×10^{-10}	2×10^{-10}	6×10^{-10}	1×10^{-8}	1×10^{-8}
100kg					
87	2×10^{-7}	2×10^{-10}	2×10^{-10}	1×10^{-8}	2.3×10^{-7}
223	1×10^{-8}	2×10^{-10}	3×10^{-10}	1×10^{-8}	2×10^{-8}
400kg					
109	9×10^{-6}	3×10^{-10}	3×10^{-10}	1×10^{-8}	9×10^{-6}
258	2×10^{-7}	2×10^{-10}	3×10^{-10}	1×10^{-8}	2×10^{-7}
Suspension tube					
10kg					
62	3×10^{-10}	3×10^{-11}	7×10^{-11}	1×10^{-6}	1×10^{-6}
161	2×10^{-7}	3×10^{-11}	3×10^{-10}	1×10^{-6}	1×10^{-6}
100kg					
99	3×10^{-8}	7×10^{-11}	7×10^{-10}	1×10^{-6}	1×10^{-6}
221	2×10^{-9}	5×10^{-11}	5×10^{-11}	1×10^{-6}	1×10^{-6}
400kg					
170	4×10^{-7}	2×10^{-10}	2×10^{-10}	1×10^{-6}	1.4×10^{-6}
352	1×10^{-8}	2×10^{-10}	1×10^{-10}	1×10^{-6}	1×10^{-6}

$\phi_{therm,SHS}$ being a function of tension, frequency and diameter. Due to adjusting d_{SHS} to the mechanical load, the tension in the SHS remains constant, when applying different loads. However with an increasing diameter, the thermal diffusion time τ_{therm} , in eq. 2.10, increases as well. In addition to this effect, the natural frequency $f_{SA,violin}$ increases with

higher tension in the SA. Actuating the SA at $f_{SA,violin}$ causes the SHS to vibrate at the same frequency, with a smaller displacement. Thus the SHS is vibrating at higher frequencies for higher load cases. Eq. 2.9 shows $\phi_{therm,SHS}$ increasing with higher frequencies in the evaluated frequency range, reflected in table A.9.

The extrinsic losses caused by the SH increase by ca. one order of magnitude from 10 kg to 400 kg. This is attributed to the increase in $U_{SH,LB/SSS}$ toward higher masses. The extrinsic losses caused by the mass remain relatively constant across all load cases.

For the monolithic suspension fibres it can be seen, that at low mechanical load, $\phi_{extrinsic}$ is one order of magnitude lower compared to ϕ_{SA} . For higher loads such as 100.400 kg the extrinsic losses, are one and two orders of magnitude larger than ϕ_{SA} respectively, with the SHS as the main contributor.

For the suspension tube, table 4.13 shows a mechanical load of 10 kg the associated $\phi_{extrinsic}$ are four orders of magnitude lower, compared to ϕ_{SA} . For a load of 100 kg the extrinsic losses are two orders of magnitude lower than ϕ_{SA} . For a load of 400 kg the extrinsic losses are one order of magnitude lower than ϕ_{SA} .

Concluding the energetic evaluation of the SSS design, with a sample under load, certain load cases can be ruled out. Due to the low intrinsic loss characteristics of the the monolithic suspension fibres, $\phi_{extrinsic}$ rise over ϕ_{SA} by one order of magnitude for applied loads of 100 kg and 400 kg. Therefore measuring the Q -factor of the monolithic suspension fibre sample under mechanical load, can only be accomplished at small load values.

For the suspension tube the loss estimation has shown that the measurement of higher mechanical loads is possible. As all load cases have $\phi_{extrinsic}$ being at least one order of magnituded lower than ϕ_{SA} .

However as certain contributions to loss cannot be modeled beforehand, such as the clamping loses at the SH and load mass. The extrinsic losses are highly dependent on the setup, so that only the experimental investigation can show the actual losses. In the scope of this work is these extrinsic losses are reduced as much as possible by prior FEM analysis.

5 Adaption of an Existing Setup Design

A cryogenic gravitational wave detector called KAGRA has been built and commissioned in the year 2017 [51, 52]. The GW detector uses monolithic sapphire suspensions with a diameter of 1.6 mm to suspend the 23 kg monolithic sapphire mirrors [52]. The operating temperature of the mirrors is at 20 K [52].

Research and development prior to building the KAGRA facility included measuring Q -factors of monolithic sapphire suspensions. One of these research and development facilities included the test setup measuring the Q -factors of monolithic sapphire fibres, presented in [8]. The test set up and sample geometry, as well as measured Q -factors of monolithic sapphire suspensions are published in [8].

Within the scope of this work the SSS of this Q - measurement facility has been modelled. This is used as a validation example for the modelling tool and design approach developed in this work. Therefore a MA, FRA and subsequent energetic evaluation and loss estimation on the existing test setup is conducted. The results are used to validate the design approach. This is done by comparing the resulting strain weighted loss angles of the system to the measured loss angles published in [8].

5.1 Geometry Adaption

The geometry of the sample is published in [8]. The values are presented in table 5.1. The sample and SH design of the GRAVITHELIUM test facility presented in section 4 were inspired by the test setup presented in [8]. Figure 3.4 shows the geometry of the sample used in [8], represented by the monolithic suspension fibre. The sample total length is 10 cm with a total mass of 4 g. The monolithic sapphire suspension fibre has a sample head-to-body ratio of ≈ 6 .

The cryostat, in which the Q -measurements were conducted is designed with two stages for vibration isolation. The cryostat first stage is suspended from the top flange of the vacuum chamber by three metal wires. The cryostat second stage is suspended from the first cryostat stage by three metal wires. [8]

Table 5.1: Sample geometry of the monolithic sapphire suspension measured in [8].

Quantity	l / mm	d / mm
Sample body	90.0	1.6
Head	5.0	10.0

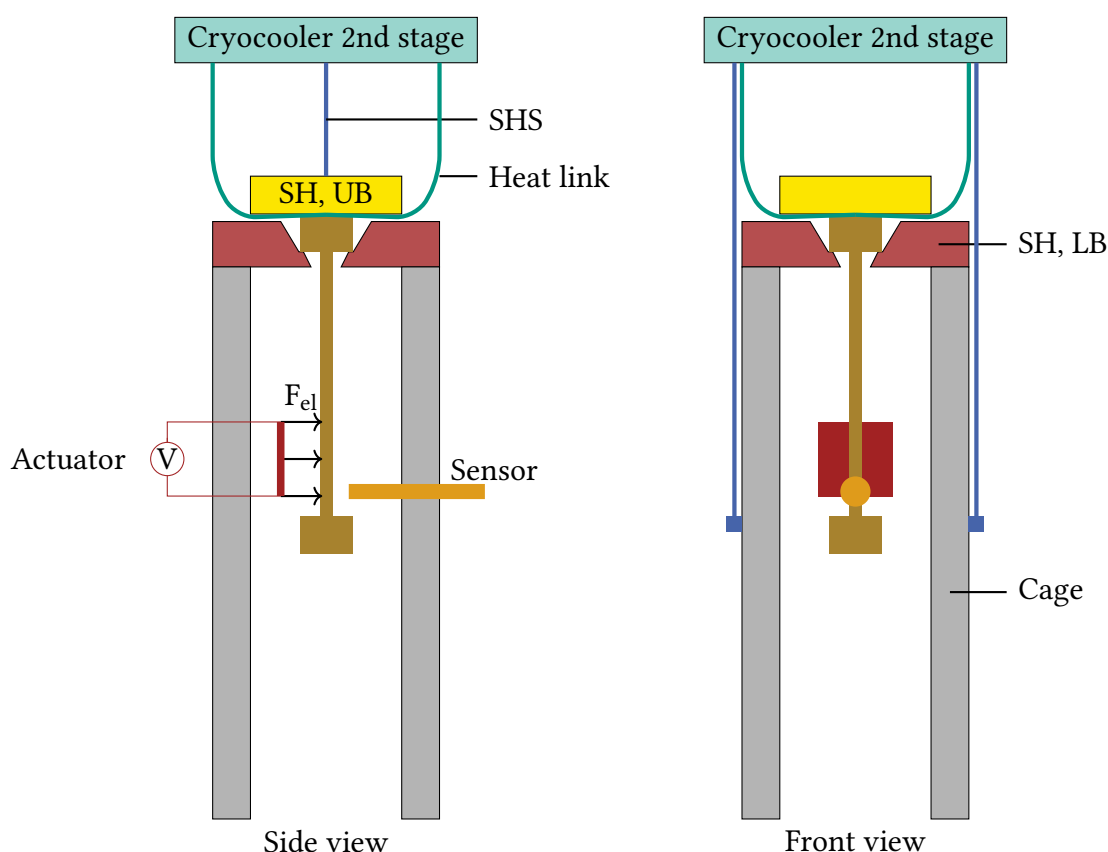


Figure 5.1: Schematic view of the SSS geometry of the set up adapted from [8, 53]

The SSS is suspended from the second cryostat stage by two wires. The SSS outlined design of the test facility is presented in figure 5.1. The dimensions of the SSS were not published. However photographed pictures showing the test set up with the sample being clamped in the SUS have been published in [8].

The dimensions of the SSS components were estimated, by comparing the known dimensions of the sample, to the SSS dimensions depicted in the photographed pictures presented in [8]. Figure 5.1 shows the SSS geometry of the test facility. The sample is clamped at one of its heads to the SH, consisting of a copper lower block and stainless steel upper block. The SSS is suspended from the cryostat second stage, by two stainless steel wires. In order to cool down the system, heat links to the cryocooler have been fixed between sapphire head and the SST SH upper block [8]. The aluminium cage is attached to the SH lower block and houses the actuator and detection sensor. The sample holder geometry is presented in figure 5.2.

The SH consists of a square copper lower block. Which has a cutout on one of its sides, in order to place the sample inside the saddle geometry. In figure 5.2 on the right a cross section of the SH is depicted. It can be seen that the sample is situated in a conical shaped saddle, with the sample protruding from below the SH. The dimensions of the SH are given in 5.2. The SH upper block is a square SST plate, with a width of 45 mm and a thickness of 5 mm.

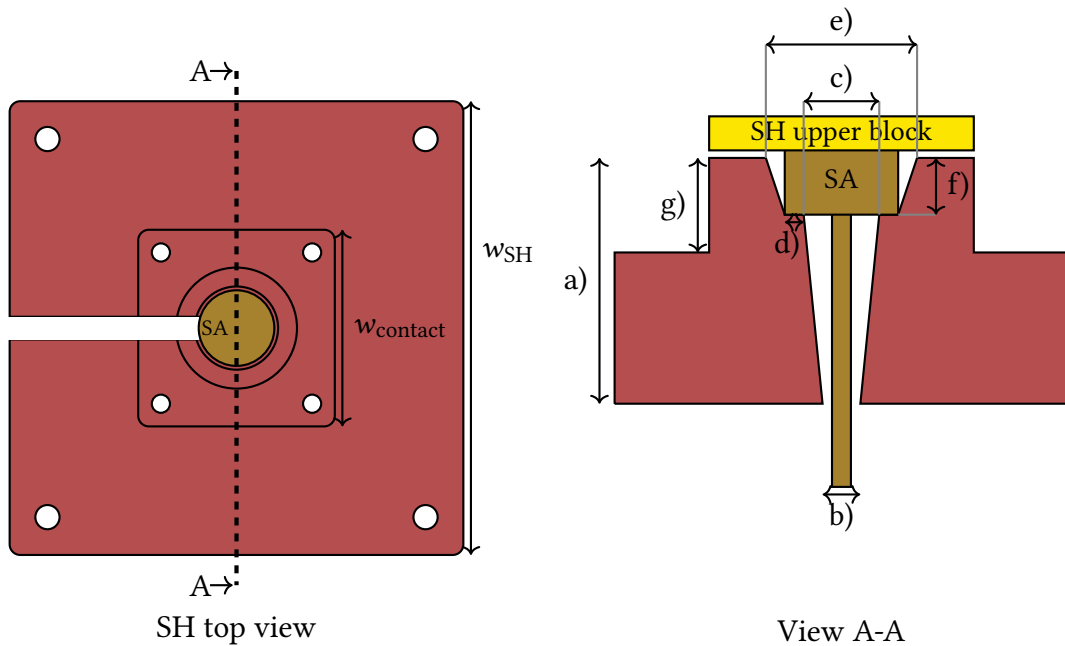


Figure 5.2: Schematic view of the geometry of the set up adapted from [8]

Table 5.2: Estimated SH geometry adapted from pictures published in [8, 53].

Symbol and Name	Dimension / mm
w_{SH} Width SH lower block	90
$w_{contact}$ Width of contact	45
a) Sample holder height	30
b) Lower cutout hole	4
c) Saddle inner diameter	6
d) Saddle width	2
e) Sample head cutout diameter	14
f) Sample head cutout height	4
g) Sample holder contact	15

The mass of the SH is ca. 1.5 kg. As can be seen in figure 5.1, two aluminium blocks, serving as the cage are attached to the SH. A single block has the length of 245 mm, a width of 20 mm and height of 95 mm, resulting in a mass of 1 kg per aluminium block. The total mass of the SSS is therefore 3.5 kg.

The dimensions of the C85 SHS wires, suspending the system from the cryostat, are not specified in [8]. The length is estimated to be $l_{SHS} = 200$ mm. The two SHS wires deployed in the adapted cases, are replaced by a single SHS, which is a steel wire, for comparability to the GRAVITHELIUM assembly. The diameter was calculated by eq. 2.6 with a deployed $SF = 3$, which yields $d_{SHS} = 0.5$ mm. The SUS in the system has a D -factor of $D = 1 \times 10^{-2}$.

5.2 Modal Analysis and Frequency Response Analysis

The MA conducted validates two aspects of the modelling tool. By comparing the simulated natural frequencies, to the measured natural frequencies [8]. The implemented elasticity coefficients for sapphire, taken from literature, are validated. And the accuracy of the deployed BC are validated. Conducting the FRA the response of the SSS of the remodelled setup can be investigated.

Setting up the geometry in the FEM model the boundary conditions relevant for the MA are assigned. Similar to the BC deployed to the model presented in section 4.1, the upper head of the SHS, connecting the SH to the second stage of the cryostat, is implemented as a fixed constraint, Dirchlet type BC. Meaning no motion of the SHS upper head is occurring in all three spacial directions. Furthermore the bolts attaching the SH upper block to the SH lower block and the aluminium block to the SH lower block are implemented as rigid connectors.

The MA yields the natural frequencies and mode shapes of the first three modes, relevant for the Q -measurements conducted in [8]. Table 5.3 presents the natural frequencies simulated in this work and the measured natural frequencies presented in [8]. The difference in simulated natural frequencies to the measured natural frequencies of the sample is maximally ca. 4 %, most likely arises from minor uncertainties of implemented elasticity coefficients for sapphire and errors arising from the use of the FEM software COMSOL[®].

Figure 5.3 shows the mode shape of the sapphire sample for $f_{SA,1}$, $f_{SA,2}$ and $f_{SA,3}$. The mode shapes are normalised to give a maximum dimensionless displacement of 1. Comparing the mode shapes in figure 5.3, to the published mode shapes in [8], a qualitative good agreement can be seen. Concluding from the MA it can be seen that the valid elasticity coefficients have been implemented from literature for monolithic sapphire. Furthermore the implementation of the BC for the SHS an activation of gravity is valid. Furthermore a result derived from the MA is the placement of the boundary load BC relevant for the FRA.

The actuator used in the remodelled set up is a 5 cm square electrostatic actuator, which is half the size of the sample (10 cm). From figure 5.3 it can be seen, that placing the BL BC to the lower half of the sample sufficiently actuates all three modes. The voltage used to actuate the sample was not stated by the author. Therefore the values presented in table 3.4 are used to calculate $F_{electric}$ via eq. A.1. Deploying these BCs yields the frequency response plot of the components of the SSS from 0 Hz to 3700 Hz in figure 5.4.

Table 5.3: Natural frequencies of the sapphire sample, measured from [8] and simulated values

Mode Number / Hz	Simulated	Measured
1 st	91	94 [8]
2 nd	1211	1260 [8]
3 rd	3581	3712 [8]

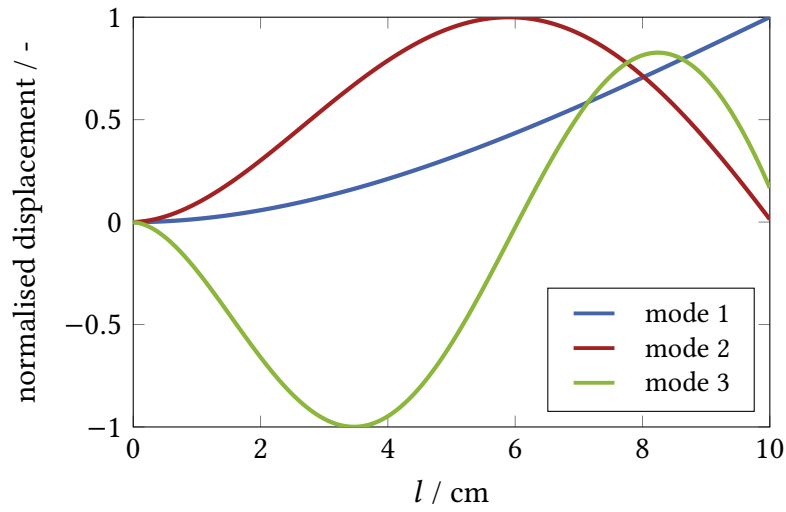


Figure 5.3: Mode shape of the sapphire sample from [8]

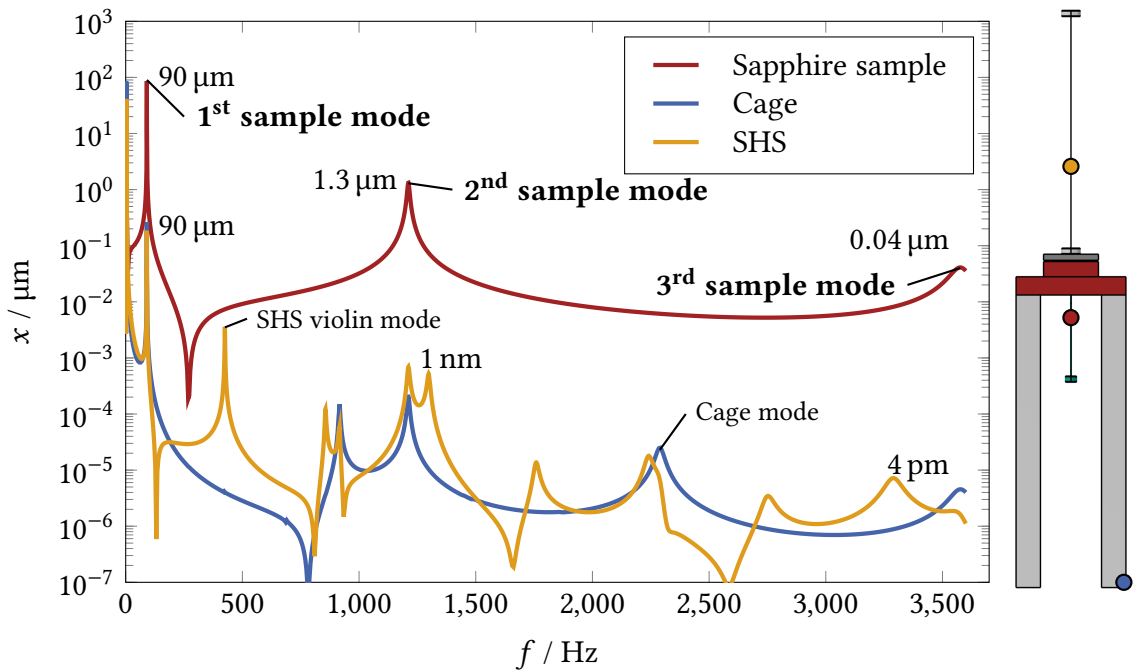


Figure 5.4: FRA of the adapted SSS

Figure 5.4 shows, that within the spectrum of 91 Hz to 3700 Hz in which the sample modes occur, several natural frequencies of the SSS occur as well. For GRAVITHELIUM the SSS is designed, with the aim of no SSS natural frequency occurring in the frequency range of 5 Hz to 205 Hz, in which f_{SA} are expected. However it should be noted that for GRAVITHELIUM the frequency span is $\Delta f = 200$ Hz and for the remodelled case the span in which f_{SA} occur is $\Delta f \approx 3500$ Hz. This difference is attributed to the longer length of the SA used for the GRAVITHELIUM. This shifts the natural frequencies to lower values.

In figure 5.4, it can be seen that the natural frequencies of the SSS, are at least 100 Hz apart from the sample modes. Therefore there is no risk of SSS modes overlapping with the sample modes. This would cause large displacements of the SSS, being associated with elevated integral strain ratio values.

For $f_{SA,3}$, it can be seen that the displacement of the sample is lower than the assumed $1 \mu\text{m}$ sensitivity of the detection system. This might be attributed to the voltage of the actuation being higher than the assumed 500 V. The response of $f_{SA,3}$ can be elevated to above $1 \mu\text{m}$ assuming a voltage 2 kV. An additional explanation might be the assumed sensitivity limit of the detection system.

At $f_{SA,1}$ it can be seen, that the displacement of the SSS is two orders of magnitudes lower, compared to the SA displacement. For $f_{SA,2}$ the displacement is three orders of magnitude lower, compared to the SA displacement. For $f_{SA,3}$ the displacement of the SSS is four orders of magnitude lower compared to the SA displacement. The FRA of GRAVITHELIUM SSS design, presented in figure 4.5, has shown higher displacements of the SSS at f_{SA} compared to the adapted case. An energetic evaluation of the adapted case is conducted and compared to the GRAVITHELIUM case.

5.3 Energetic Evaluation and Loss estimation

For the energetic evaluation of the adapted SSS, the natural frequencies of the SA are actuated. The integral strain ratios of each component are calculated and the strain weighted loss angle of each component are determined, as shown in equation 4.8. Summation of the strain weighted loss angles yields the systems $\phi_{SSS,simulated}$ as shown in eq. 4.1.

The experimentally lowest loss angle achieved for the adapted are taken from SSS [8] and the $\phi_{SSS,measured}$, are compared to the $\phi_{SSS,simulated}$. The comparison serves to validate the approach of the energetic evaluation of the system. The comparison further reveals information, on extrinsic losses, as clamping losses cannot be sufficiently modeled.

Table 5.4 presents the integral strain ratios of each component in the SSS of the remodelled test set up. In table 5.4 it can be seen, the largest contributing factor besides the SA is $U_{SH,LB/SSS}$. Hereby, the value of $U_{SH,LB/SSS}$ is larger than $U_{SH,UB/SSS}$ by a factor of 1.5. Meaning the energy contribution is higher in the SH lower block compared to the upper block. The energetic contribution to the total system of the SHS is the smallest for all modes.

The strain weighted loss angles have been calculated considering the bulk loss angles for the components SH, cage and sapphire SA. The values for the bulk losses are presented in table 5.5. For the steel SHS the thermoelastic contribution to the loss angle $\phi_{therm,SHS}$

Table 5.4: Integral strain ratio of the remodelled components of [8]

f_{SA} / Hz	$U_{SHS/SSS}$	$U_{SH,UB/SSS}$	$U_{SH,LB/SSS}$	$U_{cage/SSS}$	$U_{SA/SSS}$
91 ($f_{SA,1}$)	$3 \times 10^{-4} \%$	$6 \times 10^{-3} \%$	$7 \times 10^{-3} \%$	$1 \times 10^{-3} \%$	99.99 %
1211 ($f_{SA,2}$)	$4 \times 10^{-4} \%$	$7 \times 10^{-3} \%$	0.01 %	$1 \times 10^{-3} \%$	99.98 %
3581 ($f_{SA,3}$)	$4 \times 10^{-4} \%$	$7 \times 10^{-3} \%$	0.01 %	$2 \times 10^{-3} \%$	99.98 %

has been taken into account as well, presented in table A.11. The material data used to model $\phi_{\text{therm,SHS}}$ is presented in table A.7. Table 5.6 shows the resulting loss angles for each component of the adapted SSS.

In general it can be seen that the extrinsic losses $\phi_{\text{extrinsic}}$ are dominated by $\hat{\phi}_{\text{SH}}$. These losses are approximately one order of magnitude higher compared to ϕ_{SA} . The relatively high strain weighted loss angle of the SH is attributed to the relatively high bulk losses of copper $\phi_{\text{copper}} = 1 \times 10^{-3}$, additionally to the high integral strain ratio of $U_{\text{SH,LB/SSS}}$.

Table A.11 shows a strong dependency on frequency for $\hat{\phi}_{\text{SHS}}$, increasing by one order of magnitude from $f_{\text{SA},1}$ to $f_{\text{SA},2}$, even though $U_{\text{SHS/SSS}}$ remains quasi constant. Eq. 2.9 shows $\phi_{\text{thermoelastic}}$ is dependent on frequency. At $f_{\text{SA},2}$ the frequency at which the SHS is vibrating increases by ca. 1000 Hz compared to $f_{\text{SA},1}$. Hence the $\phi_{\text{thermoelastic}}$ from $\phi_{\text{therm,SHS}}(f_{\text{SA},1}) = 0.2$ to $\phi_{\text{therm,SHS}}(f_{\text{SA},2}) = 1.8$. Eq. 2.9 shows that $\phi_{\text{thermoelastic}}$ decline beyond a frequency of 1640 Hz, for the steel SHS of the adapted SSS. This explains $\phi_{\text{therm,SHS}}(f_{\text{SA},3}) = 1.4$ being lower compared to $\phi_{\text{therm,SHS}}(f_{\text{SA},2}) = 1.8$.

The values of the simulated $\phi_{\text{SSS, simulated}}$ and the lowest measured $\phi_{\text{SSS, measured}}$ are presented in table 5.7. The authors reports the high ϕ_{SSS} are attributed to the loss at the clamping point of the sample [8]. Comparing the simulated values to the measured lowest values presented in table 5.7, for $f_{\text{SA},1}$, relatively good agreement for the simulated and measured SSS loss angles can be seen, roughly being in the same order of magnitude. Comparing the simulated and measured system loss angles at $f_{\text{SA},2}$ and $f_{\text{SA},3}$ table 5.7 shows the simulation underestimates the losses by one order of magnitude.

The relatively good agreement at low frequency, but not at higher frequencies might be attributed to the fact, that only bulk losses are taken in to account to the model. Thermoelastic losses in the copper SH might have a noticeable dependency on frequency. For lower frequencies $f_{\text{SA},1}$ the thermoelastic contribution might be small and rises at higher frequencies. Additionally the effect of pre tension caused by fastening the bolts, which cannot be modelled, in the SH bulk material might have a dependency on frequency subsequently increasing $\phi_{\text{extrinsic}}$.

Table 5.6 shows the strain weighted loss angle of the SHS, is in the same order of magnitude as ϕ_{SA} . The specific d_{SHS} is not published and might be larger compared to

Table 5.5: Bulk losses for each component in the SSS.

Material	ϕ_{bulk}	Material	ϕ_{bulk}
Sapphire	1×10^{-8} [46]	Copper	1×10^{-3} [54]
SST	1×10^{-4} [55]	Al-6061	1×10^{-6} [48]

Table 5.6: Integral strain energy ratios in Silicon HV2 samples

$f_{\text{SA}} / \text{Hz}$	$D\hat{\phi}_{\text{SHS}}$	$\hat{\phi}_{\text{SHS}}$	$\hat{\phi}_{\text{cage}}$	$\hat{\phi}_{\text{SA}}$	$\Sigma\phi_{\text{SSS}}$
91 ($f_{\text{SA},1}$)	6×10^{-9}	8×10^{-8}	7×10^{-12}	1×10^{-8}	8×10^{-8}
1211 ($f_{\text{SA},2}$)	7×10^{-8}	1×10^{-7}	1×10^{-11}	1×10^{-8}	2×10^{-7}
3581 ($f_{\text{SA},3}$)	6×10^{-8}	1×10^{-7}	2×10^{-11}	1×10^{-8}	2×10^{-7}

Table 5.7: Lowest reported experimentally achieved loss angle of the SUS design reported in [8].

Mode Number	$\phi_{\text{SSS,measured}}$	$\phi_{\text{SSS, simulated}}$
91 Hz ($f_{\text{SA},1}$)	1×10^{-7}	8×10^{-8}
1211 Hz ($f_{\text{SA},2}$)	1×10^{-6}	2×10^{-7}
3581 Hz ($f_{\text{SA},3}$)	1×10^{-6}	2×10^{-7}

the deployed $d_{\text{SHS}} = 0.5$ mm. Increasing the diameter of the SHS would result in a higher $\phi_{\text{therm,SHS}}$ contribution, potentially becoming a limiting factor.

5.3.1 Comparison of Adapted and GRAVITHELIUM Sample Support Structures

Comparing the cases of the adapted $\text{SSS}_{\text{adapted}}$ and the designed $\text{SSS}_{\text{GRAVITHELIUM}}$ presented in section 4.1, with a deployed HV2 sapphire sample, offers a high comparability of the two setup designs.

Table 4.8 shows the simulated lower bound for $\phi_{\text{SSS,GRAVITHELIUM}}$ and table 5.6 shows the lower bound for $\phi_{\text{SSS,adapted}}$. Comparing the strain weighted loss angles of both SSS, it can be seen that $\phi_{\text{SH,GRAVITHELIUM}}$ is by three orders of magnitude lower compared to the $\phi_{\text{SH,adapted}}$. The large difference, in modelled strain weighted loss angle, is due to the difference in deployed materials. The SH of the adapted case, consists of copper with $\phi_{\text{Cu}} = 1 \times 10^{-3}$ [54] and stainless steel with $\phi_{\text{SST}} = 1 \times 10^{-4}$ [55]. Whereas the SH designed for GRAVITHELIUM, consists of aluminium with $\phi_{\text{Al-6061}} = 1 \times 10^{-6}$ [48] and tungsten with $\phi_{\text{Tungsten}} = 1 \times 10^{-6}$ [49]. The bulk loss angles of the less lossy materials deployed material to the SH in GRAVITHELIUM, are at least two orders of magnitudes lower compared to the deployed materials in the adapted SH. Thus explaining the large improvement of ϕ_{SH} . The clamping losses are reported as the critical extrinsic contribution, limiting the systems achievable lower ϕ_{SSS} [24, 8]. Therefore the reduction of the losses cause by the SH, by about three orders of magnitude serve as a first improvement to the adapted case. This relation needs to be experimentally validated.

Table A.8 shows $\phi_{\text{therm,SHS,GRAVITHELIUM}}$ and table A.11 shows $\phi_{\text{therm,SHS,adapted}}$. Comparing the values for the thermoelastic contribution to the loss angle to the SHS at $f_{\text{SA},2,\text{GRAVITHELIUM}} = 61$ Hz and $f_{\text{SA},1,\text{adapted}} = 91$ Hz, it can be seen deploying Ti-6Al-4V as the SHS material significantly reduces thermoelastic losses by a two orders of magnitude.

6 Sample Support Structure Design

Phase-II

As described in chapter 3, one of the objectives of the test facility is to measure the dissipative mechanisms of superfluid helium. Hereby, a measurement, of the influence of He-II, on the suspension tubes Q -factor is conducted. This measurement campaign, involves the investigations of mechanical dissipation mechanism of the He-II phase. Hence phase-II constitutes a new field of research.

This section presents the design process and a potential design of a SSS for the measurement campaign conducted in phase II. Hereby special focus was placed in, maximising the SSS design comparability to the measurements conducted under phase-I. In contrast to phase-I, the phase-II measurement campaigns will not contain Q -measurements with mechanical load applied to the SA .

General Geometry

Figure 6.1, shows the general geometry of the SSS used to conduct the phase-II measurement campaign. The key components of the SSS are left constant compared to phase-I, including the SHS, cage, support block and test chamber flange. To the SSS the components,

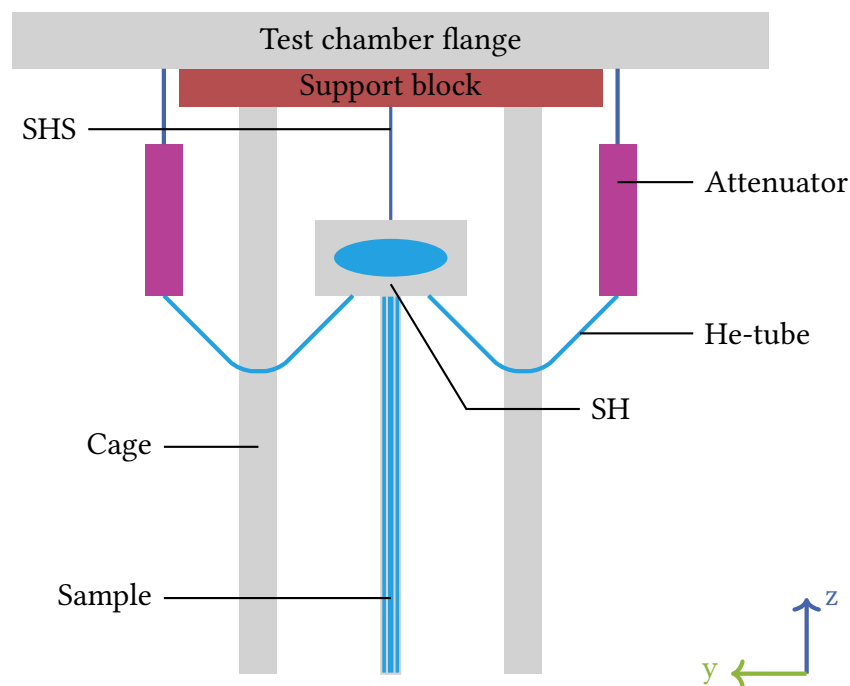


Figure 6.1: General SSS geometry for phase II measurements

He-tubes (HT) and a vibration attenuation (VA) system are added. Phase-II includes a He-supply cryostat, which supplies the suspension tube with helium at a temperature of ca. 1.8 K [35]. The suspension tube is provided with liquid helium via He-supply and return tubes. These HT are connected to the SH. A VA system attenuates vibrations stemming from the He-supply cryostat. The design of such a VA system exceeds the scope of this work.

The design in this work for phase-II is a preliminary design. This is mainly attributed to the fact, that the VA system is still in the research and development phase and does not have a conclusive design. The specific design of the VA system, influences decisive design parameters for the HT. Hence, the presented design mainly focuses on clarifying certain influences of the HT geometry, in order to assess the SSS design more accurately once the VA design is set.

The design process for the SSS of phase II, follows the key steps of MA, FRA, energetic evaluation and loss estimation of the total system outlined in figures 3.3, 4.3 and 4.7. The sample investigated in this case is the suspension tube, with the same body dimensions as presented in table 3.3. The following investigations: MA, FRA and loss estimation of the total system are conducted on the suspension OT only, as described in chapter 3.

In figure 6.2, the components of the SH have been denoted by letters. The a) supply interface (SI) is connected to the IT of the suspension tube. The b) return interface (RI) is connected to the suspension tube OT. The HT supplying / returning the He to the He-supply cryostat connect to the c) connection holes drilled to the SH. The OT is rigidly jointed to a d) insert block, which is jointed to the SH. The insert joining the OT has a conical support underneath the joint. The larger diameter of the cone is $d_{\text{cone}} = 10$ mm

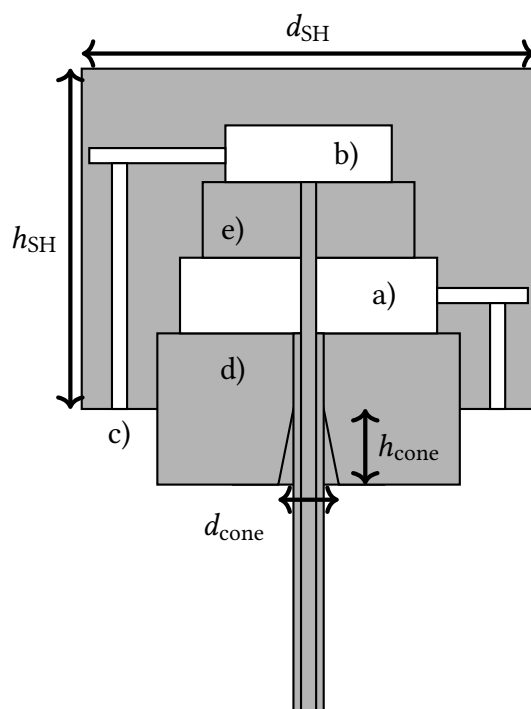


Figure 6.2: Cross section of the phase-II SH design, without the HT (courtesy of M. Stamm)

and the height of the conical cutout is $h_{\text{cone}} = 20$ mm. The IT is rigidly joined to the e) insert block, which is jointed to the SH.

The SH and SA form a single body in which the suspension tube IT is connected to the SI and the OT is connected to the RI. This requires the SH to be made of the same material as the suspension tube, being titanium [7]. Figure 6.2 shows the outlined design of the SH. The SH design has a conical cutout support under the joint between SH and suspension OT. This was inspired by the design of the phase-I SH having a conical shape supporting the samples head, depicted in figure 4.2. The use of the design of the conical shape under the joint of the sample has been found to be energetically beneficial, reducing large accumulation of strain density at the joint of SA to the insert. This has shown to decrease the $U_{\text{SHS/SSS}}$ by 50 %.

In order to maximise comparability between measurements conducted under phase-I and phase-II $d_{\text{SH,phase-II}} = 200$ mm has been deployed. Furthermore the mass of the SH for phase-II is also left constant $m_{\text{SH,phase-II}} = 10$ kg. Due to the mass of the SH of both experimental campaigns being constant, the same Ti-6AL-4V SHS with $d_{\text{SHS}} = 1.1$ mm and $l_{\text{SHS}} = 300$ mm is deployed.

The SH connects to the He supply cryostat via four titanium He tubes (HT). Figure 6.3 shows the general geometry of the HT. The HT have an outer diameter of $d_{\text{HT,o}} = 7.1$ mm and an inner diameter of $d_{\text{HT,i}} = 4.3$ mm, which were set by the preliminary design by Koroveshi et al. The height to the attenuation system was assumed to be constant, with $h_{\text{HT,AT}} = 100$ mm. Both the height to the SH $h_{\text{HT,SH}}$ and length l_{HT} of the HT were part of the design study conducted in this work. The dimension l_{HT} is limited by the distance between SH and cage as the attenuation system can only be placed outside the cage. The distance between perimeter of the SH and cage is assumed 190 mm.

Two different HT geometries have been considered in the scope of this work. Where one case represents a short HT at minimal $h_{\text{HT,SH}}$ and the other case represents twice the value for $h_{\text{HT,SH}}$ of the HT. Table 6.1 presents the design parameters chosen for the two cases investigated in this work.

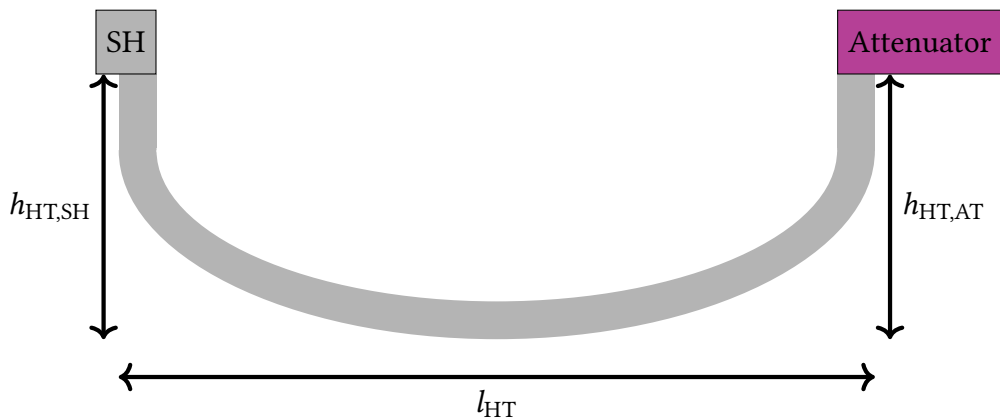


Figure 6.3: HT preliminary design by Koroveshi et al.

Table 6.1: Design parameters used for the two investigated He-tubes

Component	Dimension / mm
HT variant 1	
l_{HT}	200
$h_{HT,SH}$	200
$h_{HT,AT}$	100
HT variant 2	
l_{HT}	200
$h_{HT,SH}$	100
$h_{HT,AT}$	100

Boundary conditions

Similar to phase-I the SUS is suspended from the same 300 mm long SHS with its upper head connected to the support block. The boundary condition deployed for the SHS upper head is the Dirichlet type boundary condition, FC. Furthermore the addition of the HT requires additional sets of boundary condition deployed to the FEM model. The HT are connected to the VA system. The systems mass is assumed to be 5 kg. Therefore the boundary condition added mass is deployed to the end of the HT, connecting to the VA system. Furthermore as the VA system is rigidly joined to the HT, limits its displacement in z-direction. Therefore the Dirichlet type BC called roller has been set in the model, preventing the displacement in z-direction.

Deploying these sets of BC, a MA can be conducted, which conclude natural frequencies and mode shapes of the sample. The addition of the HT to the SSS are associated with their natural frequencies, increasing the complexity of the design.

6.1 Modal analysis and Frequency Response Analysis

The natural frequency values of the SA have been found to be the same, as for HV1 empty suspension tubes, presented in section 3.2. The natural frequencies of the suspension tube are presented in table 3.6. The mode shapes of the suspension tube in phase-II are the same as the mode shapes for presented for the HV1 suspension tube in figure 3.6. Concluding the MA of the SA, the modes relevant for the Q -measurements are in the range of 9 Hz to 150 Hz and the natural frequencies of the HT should not interfere the SA within this range.

The natural frequencies of the HT are presented in table 6.2. It can be seen the shorter HT variant 1 geometry has three natural frequencies in the range of 0 Hz to 250 Hz, whereas the longer He-tube has four natural frequencies in this range. This is attributed to the first mode occurring at lower frequencies, for longer geometries. Causing the higher order modes to shift to lower frequencies as well. Both He-tube configurations have one natural frequency in the range of 9 Hz to 150 Hz.

The effect of the HT is further investigated by a FRA, conducted in the frequency range of 0 Hz to 200 Hz. The mode shapes of the SA conclude the maximal displacement

occurring at the free end of the sample for all three relevant f_{SA} , hence the BL BC is placed at that point. The actuation of the sample is conducted in the same way as presented in section 4. The values are presented in table 3.4. A FRA of both HT geometry cases is conducted. Figure 6.4 shows the frequency response plot of the SSS utilising HT variant 1 and figure A.12 shows the frequency response plot of the SSS utilising HT variant 2.

The FRA shows, that the inclusion of the HT introduces multiple SSS natural frequencies to the system due to increased complexity. Most notable is the inclusion of the system rocking mode, which is occurring due to the added mass of 5 kg at the end of each HT. At

Table 6.2: Natural frequencies of HT geometric evaluation.

He tube Mode Number	Frequency / Hz
HT variant 1	
$f_{HT1,1}$	3
$f_{HT1,2}$	13
$f_{HT1,3}$	194
HT variant 2	
$f_{HT2,1}$	2
$f_{HT2,2}$	4
$f_{HT2,3}$	59
$f_{HT2,4}$	230

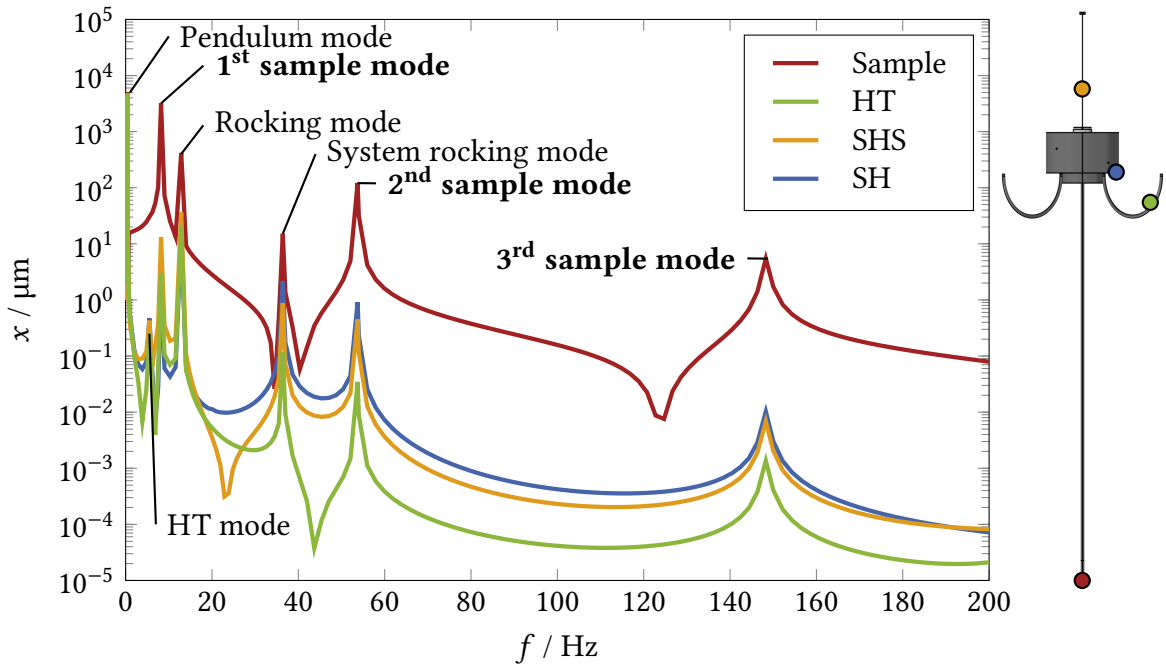


Figure 6.4: FRA of set up design utilising He-tubes variant 1

the system rocking mode the HT and the added mass, are rocking together with the SSS. This is contrary to the SUS rocking mode where the He-tubes are still. For The HT variant 1 geometry the system rocking mode occurs at ca. 35 Hz and for HT variant 2 geometry the system rocking mode occurs at ca. 15 Hz. Furthermore for HT variant 2 geometry the proximity of $f_{HT2,3} = 59$ Hz to the $f_{SA,2} = 50$ Hz causes the response of the HT at $f_{SA,2}$ to be relatively large. This causes large elastic displacements of the HT, which are associated to an increased energetic contribution of the HT to the total system dissipation.

6.2 Energetic Evaluation and Loss Estimation

Subsequently to the FRA, an energetic evaluation and a lower bound for the loss angle ϕ_{SSS} is calculated, as shown in eq. 4.1. Table 6.3 shows the simulated integral strain ratios of each component of the SSS. At $f_{SA,1}$ it can be seen that $U_{HT/SSS}$ is the highest contributor to strain energy, besides the SA, for both HT geometries. This is attributed to the proximity of $f_{SA,1}$ to $f_{HT1,2}$ and $f_{HT2,2}$, causing a high response at the slightly higher frequency $f_{SA,1} = 9$ Hz.

Table 6.3: Integral strain energy ratios of the phase-II SSS

f_{SA} / Hz	$U_{SHS/SSS}$	$U_{SH/SSS}$	$U_{HT/SSS}$	$U_{SA/SSS}$
HT variant 1				
7 ($f_{SA,1}$)	0.03 %	0.1 %	18.3 %	81.3 %
54 ($f_{SA,2}$)	2×10^{-4} %	0.2 %	0.6 %	99.2 %
148 ($f_{SA,3}$)	1×10^{-6} %	0.2 %	0.003 %	99.8 %
HT variant 2				
7 ($f_{SA,1}$)	0.1 %	0.1 %	37.4 %	62 %
54 ($f_{SA,2}$)	1×10^{-3} %	0.2 %	2.1 %	97.6 %
148 ($f_{SA,3}$)	1×10^{-5} %	0.2 %	0.03 %	99.8 %

Table 6.4: Strain weighted loss angle for the components of the phase-II SSS

f_{SA} / Hz	$D\hat{\phi}_{SHS}$	$\hat{\phi}_{SH}$	$\hat{\phi}_{HT}$	$\hat{\phi}_{SA}$	ϕ_{SSS}
HT variant 1					
7 ($f_{SA,1}$)	4×10^{-9}	2×10^{-9}	2×10^{-7}	1×10^{-6}	1.2×10^{-6}
54 ($f_{SA,2}$)	3×10^{-10}	2×10^{-9}	6×10^{-9}	1×10^{-6}	1×10^{-6}
148 ($f_{SA,3}$)	4×10^{-12}	2×10^{-9}	3×10^{-11}	1×10^{-6}	1×10^{-6}
HT variant 2					
7 ($f_{SA,1}$)	4×10^{-9}	1×10^{-9}	4×10^{-7}	1×10^{-6}	1.4×10^{-6}
54 ($f_{SA,2}$)	3×10^{-10}	2×10^{-9}	2×10^{-8}	1×10^{-6}	1×10^{-6}
148 ($f_{SA,3}$)	6×10^{-12}	2×10^{-9}	3×10^{-10}	1×10^{-6}	1×10^{-6}

From table 6.3 it can be seen, that for the SSS with HT variant 2 deployed, the energetic contribution of the HT to the total system is elevated compared to HT variant 1. This is reflected in figure A.12, which depicts the frequency response of the HT variant 2 at $f_{SA,2}$ being elevated. This is attributed to the proximity of $f_{HT2,3} = 59$ Hz to $f_{SA,2} = 50$ Hz. As the HT variant 1 geometry does not have any natural frequencies occurring close to $f_{SA,2}$ the $U_{HT1/SSS}$ is a factor of ca. 2 smaller compared to $U_{HT2/SSS}$. For $f_{SA,3}$ the largest energy contribution besides the SA stems from the SH. At this sample frequency, it can be seen that $U_{HT1/SSS}$ is lower by one order of magnitude compared to $U_{HT2/SSS}$.

A lower bound of the systems loss angle ϕ_{SSS} can be estimated by calculating the strain weighted loss angles. For the components SA, SH and HT the bulk losses are taken into account. For titanium bulk losses are $\phi_{Ti} = 1 \times 10^{-6}$ [6]. For the SHS the thermoelastic contribution to the loss angle $\phi_{therm,SHS}$ is taken into account. The calculated values of $\phi_{therm,SHS}$ are presented in table A.14.

As described earlier, the OT and IT are rigidly joined to insert blocks, which are then joined to the SH. These joints are associated with additional loss, attributed to stresses in the joint. This effect has been shown for fused silica [56] and for sapphire [8]. Additionally these losses depend on the manufacturing process [8]. The jointing losses for titanium, require experimental validation and cannot be modeled and are therefore excluded from this investigation. The strain weighted loss angles of each component and the lower bound of the total system loss angle ϕ_{SSS} , are presented in table 6.4.

From table 6.4 it can be seen at $f_{SA,1}$ the extrinsic losses $\phi_{extrinsic}$ are one order of magnitude lower than ϕ_{SA} . The extrinsic loss angle is hereby dominated by the HT, attributed to their very large values of $U_{HT/SSS} > 15\%$. At $f_{SA,2}$ it can be seen, that $\phi_{extrinsic}$ is dominated by the loss angle in the HT. For the HT variant 1 based SSS design the $\phi_{extrinsic}$ is three orders of magnitude lower, compared to ϕ_{SA} . Whereas for the HT variant 2 SSS based design the $\phi_{extrinsic}$ are two orders of magnitude lower compared to ϕ_{SA} . This is reflected in the relative high displacement response of the HT variant 2 design, shown in figure A.12.

At $f_{SA,3}$, it can be seen that $\phi_{extrinsic}$ is limited by the SH for both HT variants, $\phi_{extrinsic}$ are 3 orders of magnitude lower compared to ϕ_{SA} . Noticeable is the strain weighted loss angle of the HT component, with HT variant 1 shows $\phi_{HT1} = 3 \times 10^{-11}$ and HT variant 2 exhibits $\phi_{HT2} = 3 \times 10^{-10}$. This is attributed to the lower integral strain energy ratio for the HT variant 1, which is one order of magnitude lower compared to that of the HT variant 2.

Concluding the energetic evaluation of the SSS phase-II, it has been shown that the first mode is associated with high strain weighted loss angles, due to higher elastic deformation of the HT. For $f_{SA,2}$ and $f_{SA,3}$ it is concluded, that the HT is not expected to be a limiting factor to the Q -measurement. Furthermore it has been shown, that an overall shorter He tube, with the presented diameter configuration is energetically beneficial, to the overall losses. This is attributed to the fact that longer HT geometries have a higher number of modes in a given frequency range. This increases the probability of HT modes overlapping with SA modes. This causes a higher response of the HT, subsequently increasing strain weighted loss angle, due to strain.

7 Impact of Cryocooler Vibration on the Test Setup Design

For the phase-I experimental campaign, the largest environmental influence on vibration is expected to stem from the cryocooler. The 2nd stage of the cryocooler is attached to the test chamber flange via thin metal ribbons. Figure 7.1 shows the schematic of the investigated geometry for this analysis.

The cryocooler cooling the test chamber is set to be a Pulse Tube (PT) Cryomech PT-425 cryocooler, with a remote motor option [7]. The cryocooler reaches a minimum temperature of 2.8 K at 0 W heat load and at a temperature of 4.2 K the cooling capacity is 2.7 W [57]. Vibration analysis of the cryomech PT-425 are not available in literature to date, at which this work has been conducted.

In the context of the KAGRA research and development phase, a "vibration free (meaning limited to seismic vibrations) pulse tube cryocooler system" for GW detector applications, has been developed [58, 34, 59, 60]. In the scope of the development of such a cryostat, vibration analysis of different cryocooler types have been conducted in [34]. These

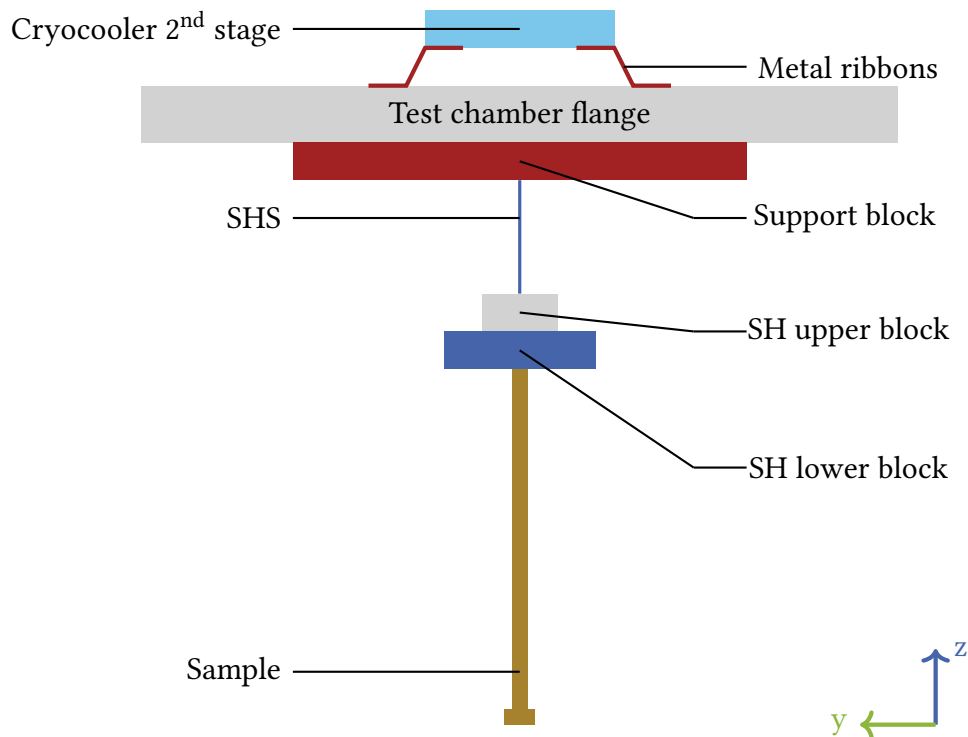


Figure 7.1: Detailed schematic of the general SUS geometry

Table 7.1: Comparable parameters of the PT cryocooler SRP-052A and PT425.

Quantity	SRP-052A	PT-425
Base temperature/ K	2.3 [60]	2.8 [61]
Cooling capacity at 4.2 K / W	0.9 [60]	2.7 [61]
Filling pressure / MPa	1.8 [60]	1.8 [61]

investigations included the analysis of three different cryocooler types. A 4 K 2 stage Gifford McMahon cryocooler, a 40 K single stage PT cryocooler and a 4 K 2 stage PT cryocooler. The former being the Sumitomo SRP-052A remote motor PT cryocooler, which has been found to be optimal for the requirements of the cryostat with minimal vibration. The minimum temperature of the cryocooler is 2.3 K at 0 W and the cooling capacity of the cryocooler 2nd stage at a temperature of 4.2 K is specified at 0.9 W [60].

The vibration analysis of cryocoolers conducted in the scope of the research and development campaigns, has concluded two main sources of vibrations. The first being an overall cold head vibration, caused by the movement of compressor, rotary valve unit and working gas flow [58, 34]. The second source of vibration is the vibration at the 2nd stage of the cryocooler. The latter vibrations are caused by the elastic deformation of the pulse and regenerator tubes, due to the helium pressure oscillation inside the cryocooler [58, 34].

Comparing the dimensions of the SRP-052A and PT-425 cryocoolers themselves is not possible, as Sumitomo does not list the SRP-052A cryocooler in the product catalog anymore. Therefore the only available comparable values of capacity, base temperature and filling pressure are presented in table 7.1.

Since extensive investigation on the SRP-052 PT cryocooler has been conducted, the cryocoolers vibration characteristics have been implemented in the FEM model. This serves as an initial assumption, investigating the effect of the cryocooler second stage vibration could potentially have to the test setup conducted under phase-I.

The analysis presented in this section is a random vibration analysis. The vibrations stemming from the cold head of the cryocooler neglected in this study, as the cryocooler second stage vibration occur closer to the SSS. Attributed to the nature of the vibrations created by a cryocooler are random, as defined in section 2.4. In addition to the SSS the model includes the support block, test chamber flange and the copper ribbons. The evaluated quantity is the displacement of the sample due to the displacement of the metal ribbons, which are experiencing the same displacement as the cryocooler 2nd stage. The metal ribbons are assumed to be copper ribbons in the scope of this investigation. Figure 2.7 in chapter 2 shows the measured displacement PSD of the cryocoolers SRP-052A second stage. The RMS displacement of the second cold stage is reported to be $x_{RMS} = 15 \mu\text{m}$. These data were integrated as an input for the random vibration analysis.

The outer perimeter of the test chamber flange was implemented as a FC BC, which keeps the flange locked in place, however allowing the transmission of vibrations. Implementing the displacement PSD as a boundary condition to the random vibration analysis is not possible directly. This is purely attributed to COMSOL[®] not supporting displacement

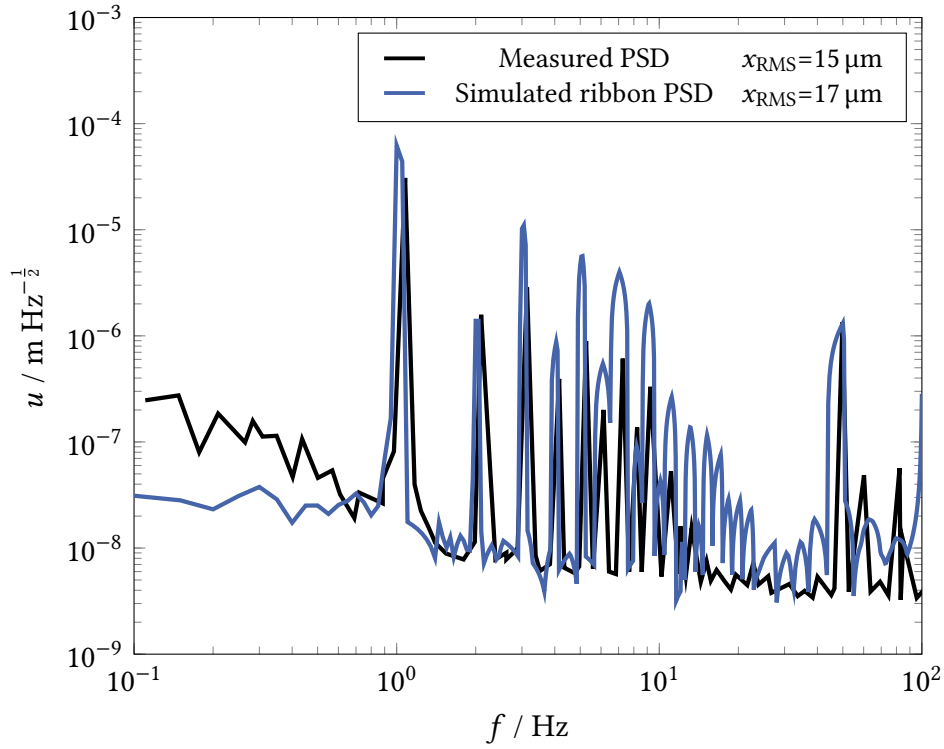


Figure 7.2: Measured displacement PSD of the Cryocooler 2nd stage and simulated displacement PSD of the Cu-ribbons

PSDs as boundary conditions, for random vibration analysis [62]. As discussed earlier, the pressure oscillation is the main contributor to vibrations at the second cold stage, caused by elastic deformation of the pulse and regenerator tubes [58]. This has been measured and validated in [34], by measuring a pressure PSD in the helium tubing and relating it to the displacement PSD of the cryocooler 2nd stage [34]. The measurement of the pressure PSD is published in the frequency range of 0.1 Hz to 100 Hz [34].

Therefore the pressure PSD is implemented as a Neumann type BC to the random vibration analysis. The copper ribbons are rigidly connected to the cryocooler 2nd stage. Hence the pressure PSD is applied to the upper surfaces of the copper ribbons. Since the specific dimensions of the cryocoolers 2nd stage are unknown, it has been excluded from the model. Therefore the aim of the pressure PSD is to replicate the displacement PSD of the cryocooler at the copper ribbons. This is accomplished by scaling the pressure PSD a constant scaling factor, across the entire frequency band width. The aim of this factor is to yield a resulting RMS value $x_{\text{RMS,ribbons}} = 15 \mu\text{m}$, as stated by [34]. Therefore assuming the ribbons follow the displacement of the cryocooler 2nd stage. Figure shows the comparison between the measured displacement of the cryocooler second stage and the simulated displacement PSD of the copper ribbons.

Comparing the measured displacement PSD of the cryocoolers 2nd stage and the simulated displacement PSD of the copper ribbons, it can be seen that the RMS values of the displacement only differ by $2 \mu\text{m}$. Further more it can be seen, that the simulated displacement PSD correspond well to the majority of the characteristic frequencies exhibited by

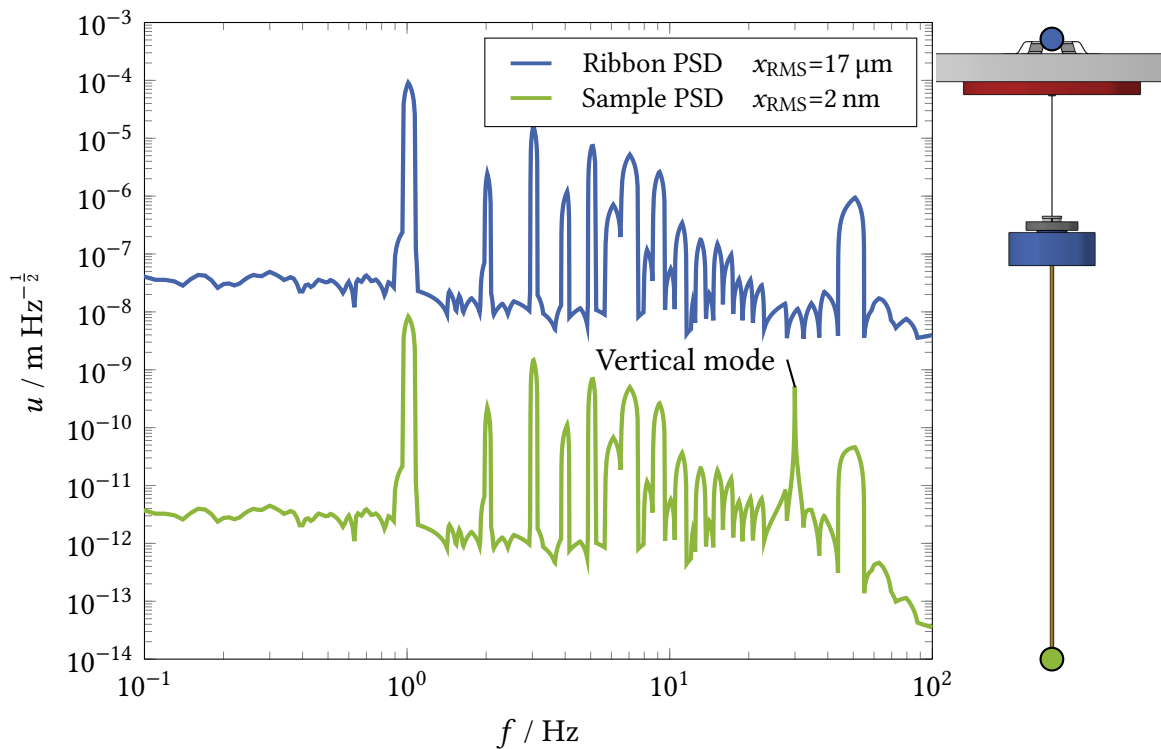


Figure 7.3: Ribbon displacement PSD and Sample displacement in vertical direction

the cryocooler. In the frequency range of 0.1 Hz to 1 Hz the simulation underestimates the measured displacement PSD by a factor of ca. 10. The relatively high discrepancies at lower frequencies might be attributed to the pressure oscillation not contributing to vibration within this frequency range. The source for vibration might be dominated by the type 1 vibrations transmitting to the 2nd stage of the cryocooler. In the frequency range of 5 Hz to 20 Hz the ribbon displacement PSD overshoots the measured cryocooler 2nd stage displacement PSD values by a factor of ca. 4.

The copper ribbons displacement PSD overlaps with the measured displacement PSD of the 2nd stage of the cryocooler over the majority of the measured frequency displacement. Therefore the displacement PSD of the copper ribbons can be regraded as an input to the system. The sample PSD can be regarded as a response to the displacement experienced by the copper ribbons depicted in figure 7.2. The associated sample response displacement PSD in vertical direction is shown in figure 7.3.

Integrating eq. 2.41 over the entire frequency range yields the overall displacement of the sample. In figure 7.3, it can be seen that the overall sample vibration, caused by the cryocoolers 2nd stage, is at $x_{RMS} = 2$ nm, with a pronounced frequency of 1 Hz. In the frequency range of 0.1 Hz to 30 Hz the response of the sample, mirrors the displacement PSD of the cryocooler, shifted by four orders of magnitude lower. The vibrations are transmitted through the SSS to the sample. The largest response of the sample occurs at 1 Hz, which is attributed to the cryocooler having its largest displacement peak at that frequency.

At a frequency of ca. 30 Hz the SA displacement PSD has a peak with $x_{\text{RMS}} = 0.1$ nm. This peak represents the vertical mode of the SSS, being actuated by the vibrations of the cryocooler. It can be seen that the response of the SSS is below the peak of the response at 1 Hz. This means the over all vibration in vertical direction is mainly at 1 Hz. The response PSD of the sample declines beyond $f_{\text{SSS,vertical}} = 30$ Hz, except at a frequency of 50 Hz, which is the operating frequency of the cryocooler [34].

The decline of the response for frequencies above the vertical mode can be explained by eq. 2.39, which describes the frequency response of a system with a single degree of freedom. The response to frequencies above the natural frequency of the system declines, due to the denominator rising. As the SSS is a system with a mass suspend from the SHS, hence theoretically comparable to a single degree of freedom system, the effect of the response declining above the vertical mode can be explained as such.

8 Conclusion and Outlook

In the scope of this work an approach to design a SSS has been developed. Design and evaluation parameters for the SSS have been defined and are summarised in the flowcharts depicted in figures 3.3, 4.3 and 4.7. The design approach contains the following key steps: MA, FRA and energetic evaluation of the resulting SSS.

These design take into account the definition of the relevant frequencies for the Q -measurement of the various SA types. The sample analysis has concluded that the relevant sample modes are in the frequency range of 5 Hz to 205 Hz. The ET-LF frequency sensitivity is set to be at 3 Hz to 30 Hz. The sample modes are within or very close to the sensitivity frequency range. Hence a more accurate dissipation value of the ET-LF cryogenic payload can be modelled, by measuring the loss angles of the different SA types.

The MA serves to validate the defined design parameters do not cause the SSS to have overlapping natural frequencies with the investigated SA. The FRA serves as a validation, that no component of the SSS has a particularly increased displacement response close to the f_{SA} . Since this might cause high elastic deformation of the component, which scales with a higher dissipation. The energetic evaluation of the SSS, serves to estimate the lower bound of the loss angle value. The results of this analysis are, the decisive factor for a SSS design candidate.

Certain factors, which influence the dissipative behaviour, cannot be modeled. These factors include dissipation caused by e.g. jointing components, friction between components, pretension caused by fastened bolts, etc. To estimate how high these additional losses are, this work included the adaption of an existing SSS design presented in [8] to the modelling tool. The calculated lower bound values for $\phi_{SSS,FEM}$ have been compared to the measured values for $\phi_{SSS,measured}$. The comparison has concluded, that the model underestimated the $\phi_{extrinsic}$ by a factor of 10. Hence a correction factor of 10 is taken into account, to conclude which design cases are measurable for each SA type, in each investigation, for the designed SSS of GRAVITHELIUM.

The correction factor is multiplied to the $\phi_{extrinsic}$ and the corrected $\phi_{extrinsic,corrected}$ is compared to the ϕ_{SA} . If the the corrected extrinsic loss factor stay below ϕ_{SA} , the Q -factor is very likely to be measurable, meaning the dissipation of energy is not limited by the SSS.

Considering this correction factor for the SSS design, conducted for the unloaded SA, concludes the following. For the suspension tube are both HV geometries and all modes are measurable. For the sapphire SA, it is concluded that the second and third mode of the HV2 design are measurable, whereas the HV1 design, is limited by the strain weighted loss contribution of the SH. Measurable for the silicon SA, are the second and third mode for both HV SSS design. The measurements conducted for the first mode have to be omitted, in this configuration, as extrinsic losses due to the clamping exceed the dissipation of the SA.

Efforts have been made to increase the measurability of the first mode of a silicon HV2 sample. The correction factor is also implemented in this case. It can be seen, when attaching the cage to the SH directly, the measurement of the first mode becomes possible. However the investigation on effects of a PT SRP-052A cryocooler vibrations to the measurement setup, have concluded, that the noise introduced by the cryocooler is expected to be high at low frequencies. The noise is expected to be around 2 nm with a pronounced frequency of 1 Hz. As the first mode occurs at ca. 6 Hz, the noise level might be a limiting factor. Hence the measurement of the samples higher modes might conclude be sufficient.

The correction factor is also applied to the $\phi_{\text{extrinsic}}$, for the investigation conducted for a loaded SA. For the suspension tube, it can be concluded that Q -measurements can be conducted, for load masses up to 100 kg, under the assumption, the suspension tube only experiences bulk losses. This is most likely not the case, since the tension increases in the SA with applied loads, the thermoelastic contribution to the intrinsic loss angle of the suspension tube, are expected to increase. Hence the overall acceptable $\phi_{\text{extrinsic}}$ is expected to rise. For the monolithic suspension fibres the thermoelastic losses, are not expected to increase at higher load, due to their low dissipative behaviour [6]. For the sapphire SA it can be seen, that the applied loads must be below 10 kg. The specific acceptable load applied to the sapphire suspension has to be investigated in a future work. For the silicon SA it is concluded, that measuring the second violin mode, with an applied load mass of 10 kg is possible. However the correction factor of 10, might be set too low, due to the fact that additional clamping losses arise, from clamping a load mass to the SA. Hence future investigations on the extrinsic loss angle, introduced by clamping the load mass to the SA, have to be experimentally conducted.

In general it can be said, that if the correction factor of 10 multiplied to $\phi_{\text{extrinsic}}$ is potentially found to be too low, the measured lowest loss angle of the setup can be compared to the loss angles presented in this work. By doing so a more appropriate correction factor can be deployed as an input to the design approach developed. This would therefore give a more appropriate design, provided if the correction factor 10 is set to be too low, for the specific SSS design. For the test setup in phase-I it can be concluded that the design process, has been applied and has been shown to yield a design which is theoretically possible to conduct Q -measurements even for the low dissipation samples of silicon and sapphire.

Deploying the correction factor to the phase-II SSS design, it can be seen, that the measurement for the second and third mode are possible. Further more, it has been shown that a shorter HT is beneficial, due to the number of modes reducing, in a given frequency spectrum. However the effect of reduction on outer diameter, has not been investigated in the scope of this work. A reduction in outer diameter of the HT, might cause the effective spring constant of the HT to decrease [63], which might result in a softer design of the HT. This might result in a lower displacement response compared to the HT with the diameter configuration included in this work. The investigation on variation of wall thickness needs to be conducted in a future work. Additionally an investigation on the loss angle caused by the jointing at the phase II SH, needs to be investigated experimentally. For fused silica, the jointing methods have been reported, to be a limiting factor of overall loss angle [56]. Therefore an experimental validation needs to be conducted for the titanium jointing

methods.

A conclusive design for the phase-II SSS cannot be given, as done for phase-I. Due to many factors of the design still being unknown. However, these outside factors, can be used as inputs to the developed design approach in future works, i order to design a conclusive SSS design for phase-II.

Bibliography

- [1] A. Einstein. “Die Grundlagen der allgemeinen”. In: *Annale der Physik* 49 (1916), p. 769.
- [2] B. P. Abbott et al. “Observation of Gravitational Waves from a Binary Black Hole Merger”. In: *Phys. Rev. Lett.* 116 (6 2016), p. 061102. DOI: 10.1103/PhysRevLett.116.061102.
- [3] S. Dwyer et al. “Gravitational wave detector with cosmological reach”. In: *Phys. Rev. D* 91 (8 2015), p. 082001. DOI: 10.1103/PhysRevD.91.082001.
- [4] M. Punturo et al. “The Einstein Telescope: a third-generation gravitational wave observatory”. In: *Classical and Quantum Gravity* 27.19 (2010), p. 194002. DOI: 10.1088/0264-9381/27/19/194002.
- [5] M. Branchesi et al. “Science with the Einstein Telescope: a comparison of different designs”. In: *Journal of Cosmology and Astroparticle Physics* 2023.07 (2023), p. 068. DOI: 10.1088/1475-7516/2023/07/068.
- [6] X. Korovesi et al. “Cryogenic payloads for the Einstein Telescope: Baseline design with heat extraction, suspension thermal noise modeling, and sensitivity analyses”. In: *Phys. Rev. D* 108 (2023), p. 123009. DOI: 10.1103/PhysRevD.108.123009.
- [7] X. Korovesi et al. “Conceptual cryostat design for cryogenic payload suspension studies for the Einstein Telescope”. In: *IOP Conference Series: Materials Science and Engineering* 1301.1 (2024), p. 012011. DOI: 10.1088/1757-899X/1301/1/012011.
- [8] D. Chen. *Study of a cryogenic suspension system for the gravitational wave telescope KAGRA*. 2015.
- [9] R. Nawrodt et al. “Investigation of mechanical losses of thin silicon flexures at low temperatures”. In: *Classical and Quantum Gravity* 30.11 (2013), p. 115008. DOI: 10.1088/0264-9381/30/11/115008.
- [10] A. M. Gretarsson and G. M. Harry. “Dissipation of mechanical energy in fused silica fibers”. In: *Review of Scientific Instruments* 70.10 (1999), pp. 4081–4087. DOI: 10.1063/1.1150040.
- [11] J. Ekin. *Experimental techniques for low-temperature measurements: cryostat design, material properties and superconductor critical-current testing*. Oxford: Oxford university press, 2006, pp. 255–266.
- [12] P. Duthil. *Material Properties at Low Temperature*. en. 2014. DOI: 10.5170/CERN-2014-005.77.

- [13] W. E. Tefft. “Elastic constants of synthetic single crystal corundum”. In: *Journal of Research of the National Bureau of Standards. Section A, Physics and Chemistry* 70.4 (1966), pp. 277–280. DOI: 10.6028/jres.070A.024.
- [14] E. J. Boyd and D. Uttamchandani. “Measurement of the Anisotropy of Young’s Modulus in Single-Crystal Silicon”. In: *Journal of Microelectromechanical Systems* 21.1 (2012), pp. 243–249. DOI: 10.1109/JMEMS.2011.2174415.
- [15] Z. Liu. “Temperature-dependent elastic constants and Young’s modulus of silicon single crystal”. In: *Young* 4 (2021), pp. 324–326. DOI: doi:10.18429/JACoW-MEDSI2020-WEPC09.
- [16] E. Dobrovinskaya, L. Lytvynov, and V. Pishchik. “Sapphire: Material, Manufacturing, Applications”. In: Springer US, 2009, pp. 55–176. ISBN: 978-0-387-85694-0.
- [17] A. V. Cumming et al. “Silicon mirror suspensions for gravitational wave detectors”. In: *Classical and Quantum Gravity* 31.2 (2013), p. 025017. DOI: 10.1088/0264-9381/31/2/025017.
- [18] A. S. Nowick and B.S. Berry. *Anelastic relaxation in crystalline solids*. New York: Academic Press, 1972.
- [19] G. Cagnoli et al. “Damping dilution factor for a pendulum in an interferometric gravitational waves detector”. In: *Physics Letters A* 272.1 (2000), pp. 39–45. DOI: [https://doi.org/10.1016/S0375-9601\(00\)00411-4](https://doi.org/10.1016/S0375-9601(00)00411-4).
- [20] P. R. Saulson. “Thermal noise in mechanical experiments”. In: *Phys. Rev. D* 42 (8 1990), pp. 2437–2445. DOI: 10.1103/PhysRevD.42.2437.
- [21] E. Coccia and T. O. Niinikoski. “Acoustic quality factor of an aluminium alloy for gravitational wave antennae below 1 K”. In: *Lettere al Nuovo Cimento (1971-1985)* 41.7 (1984), pp. 242–246. DOI: 10.1007/BF02747011.
- [22] A. Brandt. *Noise and Vibration Analysis: Signal Analysis and Experimental Procedures*. 2nd ed. John Wiley & Sons, 2023.
- [23] Y. Levin. “Internal thermal noise in the LIGO test masses: A direct approach”. In: *Phys. Rev. D* 57 (2 1998), pp. 659–663. DOI: 10.1103/PhysRevD.57.659.
- [24] R. Nawrodt et al. “High mechanical Q-factor measurements on silicon bulk samples”. In: *Journal of Physics: Conference Series* 122.1 (2008), p. 012008. DOI: 10.1088/1742-6596/122/1/012008.
- [25] M. Alshourbagy et al. “Measurement of the thermoelastic properties of crystalline Si fibres”. In: *Classical and Quantum Gravity* 23.8 (2006), S277. DOI: 10.1088/0264-9381/23/8/S35. URL: <https://dx.doi.org/10.1088/0264-9381/23/8/S35>.
- [26] W. Duffy. “Acoustic quality factor of titanium from 50 mK to 300 K”. In: *Cryogenics* 40.6 (2000), pp. 417–420. ISSN: 0011-2275. DOI: doi.org/10.1016/S0011-2275(00)00053-9.
- [27] A. Amato. “Low Thermal Noise Coating for New Generation Gravitational-Wave Detectors”. Theses. Université de Lyon, 2019. URL: <https://theses.hal.science/tel-02475821>.

-
- [28] W. Seto. *Theory and Problems of Mechanical Vibrations*. McGraw-Hill Book Co., 1964.
- [29] G.I. Gonzalez and P. R. Saulson. “Brownian motion of a mass suspended by an anelastic wire”. In: *Journal of the Acoustical Society of America* 96.1 (1994), pp. 207–212. DOI: [10.1121/1.410467](https://doi.org/10.1121/1.410467).
- [30] K. Hjelmstad. *Fundamentals of Structural Dynamics*. 1st ed. Springer Cham, 2022. DOI: <https://doi.org/10.1007/978-3-030-89944-8>.
- [31] J.N. Reddy. *Introduction to the Finite Element Method*. 4th ed. New York: McGraw-Hill, 2019.
- [32] R.B. Lehoucq, D. C. Sorensen, and C. Yang. *ARPACK users’ guide: solution of large-scale eigenvalue problems with implicitly restarted Arnoldi methods*. SIAM, 1998.
- [33] J. Bendat and A. G. Piersol. *Random data: analysis and measurement procedures*. John Wiley & Sons, 2011.
- [34] T. Tomaru et al. “Vibration analysis of cryocoolers”. In: *Cryogenics* 44.5 (2004), pp. 309–317. ISSN: 0011-2275. DOI: <https://doi.org/10.1016/j.cryogenics.2004.02.003>.
- [35] T. Weckerle. *Helium supply unit design for the experimental investigation of cryogenic mirror suspensions in gravitational-wave detectors*. Thesis for M.Sc. degree. 2024.
- [36] X. Korovesi and F. Travasso. Personal communication, within the Monthly ET-ISB Suspension meeting. June 12, 2024.
- [37] C. T. Sun and D. F. Xue. “Single crystal growth mechanism of sapphire”. In: *Materials Technology* 28.5 (2013), pp. 286–289. DOI: [10.1179/1753555713Y.0000000060](https://doi.org/10.1179/1753555713Y.0000000060).
- [38] X. Korovesi et al. Poster Presentation, Design status of GRAVITHELIUM cryostat for cryogenic payload suspension studies for the Einstein Telescope. May 5, 2024. URL: <https://apps.et-gw.eu/tds/?r=18875>.
- [39] Y. Noh et al. “Effect of strain rate on the deformation of 6061-T6 aluminum alloy at cryogenic temperature”. In: *Materials Characterization* 206 (2023), p. 113403. DOI: <https://doi.org/10.1016/j.matchar.2023.113403>.
- [40] C. Chen et al. “Effect of grain size and temperature on deformation mechanism of commercially pure titanium”. In: *Transactions of Nonferrous Metals Society of China* 33.11 (2023), pp. 3332–3347. DOI: [https://doi.org/10.1016/S1003-6326\(23\)66337-X](https://doi.org/10.1016/S1003-6326(23)66337-X).
- [41] R. L. Tobler, R. P. Reed, and R. E. Schramm. “Cryogenic Tensile, Fatigue, and Fracture Parameters for a Solution-Annealed 18 Percent Nickel Maraging Steel”. In: *Journal of Engineering Materials and Technology* 100.2 (1978), pp. 189–194. DOI: [10.1115/1.3443470](https://doi.org/10.1115/1.3443470).
- [42] H. M. Ledbetter and D. T. Read. “Low-temperature elastic properties of a 300-grade maraging steel”. In: *Metallurgical Transactions A* 8.11 (1977), pp. 1805–1808. DOI: [10.1007/BF02646886](https://doi.org/10.1007/BF02646886).

- [43] P. Willems and M. Thattai. “Increased thermal noise in nonuniform fiber suspensions”. In: *Physics Letters A* 253.1 (1999), pp. 16–20. DOI: doi.org/10.1016/S0375-9601(99)00017-1.
- [44] M. Barsanti et al. “Experimental study of hydrogen embrittlement in Maraging steels”. In: *Procedia Structural Integrity* 8 (2018). AIAS2017 - 46th Conference on Stress Analysis and Mechanical Engineering Design, 6-9 September 2017, Pisa, Italy, pp. 501–508. DOI: https://doi.org/10.1016/j.prostr.2017.12.049.
- [45] F. Piergiovanni, M. Punturo, and P. Puppo. *The thermal noise of the Virgo+ and Virgo Advanced Last Stage Suspension (The PPP effect)*. Internal note VIR-015C-09. Apr. 14, 2009.
- [46] J. Kovalik and P. R. Saulson. “Mechanical loss in fibers for low noise pendulums”. In: *Review of Scientific Instruments* 64.10 (1993), pp. 2942–2946. DOI: 10.1063/1.1144388.
- [47] S. Amadori et al. “Low temperature anelasticity in Ti6Al4V alloy and Ti6Al4V–SiCf composite”. In: *Materials Science and Engineering: A* 521-522 (2009). 15th International Conference on Internal Friction and Mechanical Spectroscopy, pp. 340–342. DOI: https://doi.org/10.1016/j.msea.2008.09.156.
- [48] W. Duffy. “Acoustic quality factor of aluminum alloys from 50 mK to 300 K”. In: *Journal of Applied Physics* 68.11 (1990), pp. 5601–5609. DOI: 10.1063/1.346971.
- [49] W. Duffy. “Acoustic quality factor of molybdenum and tungsten at low temperatures”. In: *Journal of Applied Physics* 72.12 (1992), pp. 5628–5634. DOI: 10.1063/1.352324.
- [50] V. B. Braginski, Valerij Pavlovič Mitrofanov, and Vladimir Ivanovich Panov. *Systems with small dissipation*. University of Chicago Press, 1985.
- [51] T. Akutsu et al. “KAGRA: 2.5 generation interferometric gravitational wave detector”. In: *Nature Astronomy* 3.1 (2019), pp. 35–40. DOI: 10.1038/s41550-018-0658-y.
- [52] Y. Aso et al. “Interferometer design of the KAGRA gravitational wave detector”. In: *Phys. Rev. D* 88 (4 2013), p. 043007. DOI: 10.1103/PhysRevD.88.043007.
- [53] X. Korovesi and D. Chen. Personal communication. Jan. 2024.
- [54] W. Duffy. “Acoustic quality factor of copper, brass and beryllium copper from 50 mK to 300 K”. In: *Cryogenics* 32.12 (1992), pp. 1121–1124. DOI: https://doi.org/10.1016/0011-2275(92)90325-5.
- [55] I. Tkalcec. “Mechanical properties and microstructure of a high carbon steel”. en. PhD Thesis. Lausanne: EPFL, 2004. DOI: 10.5075/epfl-thesis-3089. URL: https://infoscience.epfl.ch/handle/20.500.14299/212410.
- [56] A. V. Cumming et al. “Design and development of the advanced LIGO monolithic fused silica suspension”. In: *Classical and Quantum Gravity* 29.3 (2012), p. 035003. DOI: 10.1088/0264-9381/29/3/035003.
- [57] X. Hao et al. “Development of High Cooling Capacity and High Efficiency 4.2 K Pulse Tube Cryocoolers”. In: *Cryocooler* (2022).

-
- [58] R. Li et al. "Vibration-Free Pulse Tube Cryocooler System for Gravitational Wave Detectors, Part II: Cooling Performance and Vibration". In: *Cryocoolers 13*. Ed. by Ronald G. Ross. Boston, MA: Springer US, 2005, pp. 703–710. ISBN: 978-0-387-27533-8.
- [59] S. Caparrelli et al. "Vibration-free cryostat for low-noise applications of a pulse tube cryocooler". In: *Review of Scientific Instruments* 77.9 (2006), p. 095102. DOI: 10.1063/1.2349609.
- [60] K. Nakano et al. "Development of high efficiency 4 K two-stage pulse tube cryocoolers with split valve unit". In: *AIP Conference Proceedings* 1434.1 (2012), pp. 532–539. DOI: 10.1063/1.4706961.
- [61] Y. Shiroyanagi et al. "Thermal analysis of a FEL SCU cryostat". In: *IOP Conference Series: Materials Science and Engineering* 1301.1 (2024), p. 012045. DOI: 10.1088/1757-899X/1301/1/012045.
- [62] COMSOL Inc. *COMSOL*. 2020. URL: <http://www.comsol.com/products/multiphysics/>.
- [63] T. Yamada et al. "High performance thermal link with small spring constant for cryogenic applications". In: *Cryogenics* 116 (2021), p. 103280. ISSN: 0011-2275. DOI: <https://doi.org/10.1016/j.cryogenics.2021.103280>.
- [64] G. Welsch, R. Boyer, and E.W. Collings. *Materials Properties Handbook: Titanium Alloys*. Materials properties handbook. ASM International, 1993. ISBN: 9780871704818.
- [65] Y. S. Touloukian et al. *Thermophysical Properties of Matter - the TPRC Data Series. Volume 12. Thermal Expansion Metallic Elements and Alloys*. English. Ft. Belvoir: Defense Technical Information Center, 1975.
- [66] H. M. Ledbetter, W. F. Weston, and E. R. Naimon. "Low-temperature elastic properties of four austenitic stainless steels". In: *Journal of Applied Physics* 46.9 (1975), pp. 3855–3860. DOI: 10.1063/1.322182.
- [67] M. Fukuhara and A. Sanpei. "Elastic moduli and internal frictions of Inconel 718 and Ti-6Al-4V as a function of temperature". In: *Journal of Materials Science Letters* 12.14 (1993), pp. 1122–1124. DOI: 10.1007/BF00420541.
- [68] Ziegler W. T., Mullins J. C., and Hwa S. C. P. "Specific Heat and Thermal Conductivity of Four Commercial Titanium Alloys from 20° to 300°K". In: *DavAdvnces in Cryogenic Engineering*. 1963. URL: <https://api.semanticscholar.org/CorpusID:138995380>.

List of Figures

1.1	Conceptual design of the GRAVITHELIUM cryostat for the first experimental campaign, with a sample under mechanical load courtesy of X. Korovesi	2
2.1	Arbitrary stress strain curve, based on [11]	5
2.2	Temperature dependency of <Si100> [12] and Titanium [13]	6
2.3	Pendulum system mode shapes adapted from [29]	11
2.4	Beam mode shapes for arbitrary frequencies and lengths for both boundary condition cases	13
2.5	Signal types with the respective mathematical description of the signals, highlighted are the signal types relevant to this work	15
2.6	Arbitrary Frequency response of a single degree of freedom system . . .	17
2.7	Displacement PSD, where $\sqrt{S_{xx}(f)} = \hat{u}_{\text{PSD}}$, of a Sumitomo cryocooler [34]	18
3.1	Helium test chamber in Phase-I, adapted from [7]	20
3.2	Helium test chamber in Phase-II adapted from [7]	21
3.3	Flowchart of how the relevant natural frequencies are defined. This section is limited to the steps to determine f_{SA}	23
3.4	SA geometry nomenclature	24
3.5	Schematic view of the sample Q -measurement actuation and detection set up. The actuator and sensor are fixed at the cage, adapted from [8] . . .	26
3.6	Mode shapes of the first four modes of HV1 SA	28
3.7	Frequency response of the HV1 SA. The cyan mark on the SA geometry represents the actuation and evaluation point for the displacement response.	30
4.1	General SSS geometry, without load suspended from the sample	31
4.2	Detailed schematic of the SH geometry, with the according nomenclature presented in table 4.1	32
4.3	Flowchart of the design steps taken for SUS and SSS. Relevant design parameters to the SH and SHS components are depicted in the green circles. The red circles denote the evaluation parameters.	34
4.4	Parametric investigation on the violin frequency for various l_{SHS} and different m_{SHS}	38
4.5	FRA of SSS with as HV2 silicon SA actuated at the highlighted red spot. .	40
4.6	Response contours of the SSS at the three natural frequencies, relevant to the Q -measurement	41
4.7	Flowchart of the followed steps for the energetic evaluation	42

4.8	Strain density distribution along the SA HV1 and HV2 at $f_{SA,3}$. The zoomed in portion, shows a section view of the inner surface of the head, in order to visualise the strain density gradient at the saddle.	44
4.9	Detailed schematic of the general SSS geometry, with cage attached to the SUS	47
4.10	SA-violin mode shapes under load	50
4.11	FRA of a SSS with the mechanical load suspended for a silicon sample:10 kg	50
5.1	Schematic view of the SSS geometry of the set up adapted from [8, 53]	56
5.2	Schematic view of the geometry of the set up adapted from [8]	57
5.3	Mode shape of the sapphire sample from [8]	59
5.4	FRA of the adapted SSS	59
6.1	General SSS geometry for phase II measurements	63
6.2	Cross section of the phase-II SH design, without the HT (courtesy of M. Stamm)	64
6.3	HT preliminary design by Korovesi et al.	65
6.4	FRA of set up design utilising He-tubes variant 1	67
7.1	Detailed schematic of the general SUS geometry	71
7.2	Measured displacement PSD of the Cryocooler 2 nd stage and simulated displacement PSD of the Cu-ribbons	73
7.3	Ribbon displacement PSD and Sample displacement in vertical direction	74
A.1	Mode shapes of the first three modes of the sample with Head Variant 2	97
A.2	Frequency response amplitude of Sapphire and Silicon sample Head Variant 2	97
A.3	Temperature dependency of Samples HV1,	98
A.4	Temperature dependency of Samples HV2	98
A.5	FRA of sample and SUS: Sapphire HV2	99
A.6	FRA of sample and SUS: Suspension Tube HV2	99
A.7	FRA of sample and SUS: Silicon HV1	100
A.8	FRA of sample and SUS: Sapphire HV1	100
A.9	FRA of sample and SUS: Suspension Tube HV1	101
A.10	Resopnse shapes of the first three Sa modes (HV1)	101
A.11	Two stage pendulum characteristic mode shapes, a) system pendulum mode, b) suspended mass rocking mode, c) SH rocking mode, d) SH pendulum mode, e) 1 st SA violin mode, f) 2 nd SA violin mode	102
A.12	FRA of set up design utilising He-tubes variant 2	103

List of Tables

2.1	Young's modulus, yield strength and density of sample material.	7
2.2	Q -factors for silicon, sapphire and Titanium at two different temperatures	9
3.1	Dimensions of GRAVITHELIUM vacuum and test chamber	22
3.2	Geometry variation of the monolithic suspension fibres	25
3.3	Geometry variation of the Suspension Tube.	25
3.4	Set boundary conditions	26
3.5	SA mesh parameters	27
3.6	Natural frequency of SA for both HV	28
4.1	SH geometry naming convention and values.	33
4.2	Candidate material characteristics at two different temperatures for the SHS	35
4.3	Resulting SHS diameters and dilution factor for potential SH mass cases and SHS lengths for the SHS candidate materials.	36
4.4	FEM and analytically calculated pendulum modes.	37
4.5	SUS f_{rock} , for various diameters for $m_{SH} = 10$ kg using Al and Cu as candidate materials	39
4.6	Integral strain energy ratios for the SSS components.	43
4.7	Bulk losses for each component in the SSS assumed in this work.	43
4.8	Strain weighted loss angles for each component and low boundary of SSS loss angles.	45
4.9	Integral strain energy ratios in Silicon HV2 samples with the cage attached to the SH.	48
4.10	strain weighted loss angles for a HV2 silicon sample with cage attached to the SH	48
4.11	SA violin modes for the different SA types	49
4.12	Integral strain energy ratios in Silicon HV2 samples under the mechanical load of 10 kg, 100 kg and 400 kg.	51
4.13	Strain weighted loss angles for all SA types, with the investigated load masses, 10 kg, 100 kg and 400 kg	52
5.1	Sample geometry of the monolithic sapphire suspension measured in [8].	55
5.2	Estimated SH geometry adapted from pictures published in [8, 53].	57
5.3	Natural frequencies of the sapphire sample, measured from [8] and simu- lated values	58
5.4	Integral strain ratio of the remodelled components of [8]	60
5.5	Bulk losses for each component in the SSS.	61
5.6	Integral strain energy ratios in Silicon HV2 samples	61

5.7	Lowest reported experimentally achieved loss angle of the SUS design reported in [8].	62
6.1	Design parameters used for the two investigated He-tubes	66
6.2	Natural frequencies of HT geometric evaluation.	67
6.3	Integral strain energy ratios of the phase-II SSS	68
6.4	Strain weighted loss angle for the components of the phase-II SSS	68
7.1	Comparable paramters of the PT cryocooler SRP-052A and PT425.	72
A.1	Natural frequency for head variation 1 model validation	91
A.2	SHS + Aluminium SH rocking modes with a set $d_{SH, LB} = 200$ mm and different masses	91
A.3	Dimensions of SSS by courtesey M. Stamm	92
A.4	Dimension summary SSS concluding from this work	93
A.5	Integral strain energy ratios of the SSS with a HV2 sapphire sample under load	94
A.6	Integral strain energy ratios of the SSS with a HV2 suspension tube under load	94
A.7	Material data necessary calculating $\phi_{thermo elastic}$	95
A.8	Thermoelastic loss contribution of Ti-6Al-4V SHS for samples with free end	95
A.9	Thermoelastic loss contribution of Ti-6Al-4V SHS for HV2 samples under load	95
A.10	Thermoelastic loss contribution of SHS of the case, where the cage is attached to the SH	96
A.11	Thermoelastic loss contribution of SST SHS for remodelled case of [8] . .	96
A.12	Natural frequencies of the Phase two suspension tubes.	96
A.13	Phase-II SH dimensions	96
A.14	Thermoelastic loss contribution of Ti-6Al-4V for measurements conducted in phase II	96

A Appendix

A.1 Appendix equations

$$F_{el} = \frac{\epsilon_0 A}{2a^2} V^2 \quad (\text{A.1})$$

$$E_{ijkl} = \begin{matrix} C_{11} & C_{12} & C_{13} & C_{14} & 0 & 0 \\ C_{12} & C_{11} & C_{13} & -C_{14} & 0 & 0 \\ C_{13} & C_{13} & C_{33} & 0 & 0 & 0 \\ C_{14} & -C_{14} & 0 & C_{44} & 0 & 0 \\ 0 & 0 & 0 & 0 & C_{44} & C_{14} \\ 0 & 0 & 0 & 0 & C_{14} & \frac{1}{2}(C_{11} - C_{12}) \end{matrix} \quad (\text{A.2})$$

A.2 Additional Tables

Table A.1: Natural frequency for head variation 1 model validation

Mode number	Si <100>		Sapphire		Suspension tube	
	FEM	Analytical	FEM	Analytical	FEM	Analytical
1 / Hz	8	8	11.5	12	7.5	7.4
2 / Hz	50	52	72.5	77	48.5	46.5
3 / Hz	140	146	203	215	138	130

Table A.2: SHS + Aluminium SH rocking modes with a set $d_{\text{SH, LB}} = 200$ mm and different masses

m / kg	10	12	15	20
h / mm	82	107	145	209
f_{rocking} / Hz	2.1	2.1	2.1	2.1

Table A.3: Dimensions of SSS by courtesy M. Stamm

Quantity	Value
Material upper flange	Aluminium
Diameter upper flange	1290 mm
Height upper flange	65 mm
Mass upper flange	230 kg
Material support block	Copper
Diameter support block	410 mm
Height support block	30 mm
Mass support block	35 kg
Material SHS	SST
Diameter SHS	4 mm
Length SHS	110 mm
Mass SHS	0.02 kg
Material SH upper block	SST
Diameter SH upper block	70 mm
Height SH upper block	25 mm
Mass SH upper block	0.7 kg
Material SH lower block	Copper
Diameter SH lower block	100 mm
Height SH lower block	49 mm
Mass SH lower block	3 kg

Table A.4: Dimension summary SSS concluding from this work

Quantity	Value
Sample	
$l_{SA-body}$	1000 mm
h_h	5 or 20
d_h	16 or 32
SHS	
Material SHS	Ti-6Al-4V
l_{SHS}	300 mm
$d_{SHS,SH}$	1.1 mm
$d_{SHS,SH,cage}$	1.6 mm
$D(d_{SHS,SH})$	0.016
$D(d_{SHS,SH,cage})$	0.02
SH, upper block	
Material SH upper block	Tungsten
$d_{SH,UB}$	120 mm
$h_{SH,UB}$	20 mm
$m_{SH,UB}$	4 kg
SH, lower block	
Material SH lower block	Al-6061
$d_{SH,LB}$	200 mm
$h_{SH,LB}$	82 mm
$m_{SH,LB}$	6 kg
Cage	
Material cage	Al-6061
$l_{SH,LB}$	1000 mm
$h_{SH,LB}$	20 mm
$w_{SH,LB}$	130 mm
$m_{SH,LB}$	14 kg

Table A.5: Integral strain energy ratios of the SSS with a HV2 sapphire sample under load

SA natural frequency	$U_{SHS/SSS}$	$U_{SH,UB/SSS}$	$U_{SH,LB/SSS}$	$U_{mass/SSS}$	$U_{SA/SSS}$
Sapphire					
10kg					
81 Hz	$1 \times 10^{-3} \%$	0.01 %	$7 \times 10^{-3} \%$	0.02 %	99.98 %
212 Hz	$7 \times 10^{-5} \%$	0.01 %	$8 \times 10^{-3} \%$	0.02 %	99.97 %
100kg					
87 Hz	0.01 %	0.01 %	$9 \times 10^{-3} \%$	0.02 %	99.94 %
232 Hz	$2 \times 10^{-4} \%$	0.01 %	$9 \times 10^{-3} \%$	0.02 %	99.95 %
400kg					
109 Hz	0.07 %	0.02 %	0.01 %	0.03 %	99.87 %
258 Hz	$1 \times 10^{-3} \%$	0.01 %	0.01 %	0.03 %	99.94 %

Table A.6: Integral strain energy ratios of the SSS with a HV2 suspension tube under load

SA natural frequency	$U_{SHS/SSS}$	$U_{SH,UB/SSS}$	$U_{SH,LB/SSS}$	$U_{mass/SSS}$	$U_{SA/SSS}$
Suspension tube					
10kg					
62 Hz	$3 \times 10^{-5} \%$	$2 \times 10^{-3} \%$	$1 \times 10^{-3} \%$	0.01 %	99.98 %
161 Hz	$2 \times 10^{-5} \%$	$2 \times 10^{-3} \%$	$1 \times 10^{-3} \%$	0.01 %	99.99 %
100kg					
99 Hz	$2 \times 10^{-3} \%$	$4 \times 10^{-3} \%$	$3 \times 10^{-3} \%$	0.01 %	99.98 %
221 Hz	$4 \times 10^{-5} \%$	$3 \times 10^{-3} \%$	$2 \times 10^{-3} \%$	0.01 %	99.99 %
400kg					
170 Hz	$2 \times 10^{-3} \%$	$9 \times 10^{-3} \%$	$7 \times 10^{-3} \%$	0.02 %	99.96 %
352 Hz	$1 \times 10^{-4} \%$	$7 \times 10^{-3} \%$	$5 \times 10^{-3} \%$	0.01 %	99.97 %

Table A.7: Material data necessary calculating $\phi_{\text{thermo elastic}}$.

Quantity	Ti-6Al-4V	SST
E / GPa	127 [11]	210 [11]
ρ / kg/m ³	4540 [64]	7850 [11]
α / 1/K	6.0×10^{-6} [65]	1.0×10^{-5} [66]
β / 1/K	-4.6×10^{-4} [67]	-4.65×10^{-4} [66]
c_p / J kg ⁻¹ K ⁻¹	1×10^{-2} [68]	2×10^{-3} [11]
λ / W m ⁻¹ K ⁻¹	0.22 [68]	3×10^{-3} [11]

Table A.8: Thermoelastic loss contribution of Ti-6Al-4V SHS for samples with free end

Silicon		Sapphire		Suspension tube	
f_{SA}	$\phi_{\text{therm,SHS}}$	f_{SA}	$\phi_{\text{therm,SHS}}$	f_{SA}	$\phi_{\text{therm,SHS}}$
HV1					
11 Hz	4.3×10^{-4}	17 Hz	6.7×10^{-4}	9 Hz	3.6×10^{-4}
51 Hz	2.0×10^{-3}	73 Hz	2.9×10^{-3}	49 Hz	1.9×10^{-3}
141 Hz	5.6×10^{-5}	203 Hz	8.0×10^{-3}	137 Hz	5.4×10^{-3}
HV2					
11 Hz	4.3×10^{-4}	17 Hz	6.7×10^{-4}	7 Hz	2.7×10^{-4}
41 Hz	1.6×10^{-3}	61 Hz	2.4×10^{-3}	39 Hz	1.5×10^{-3}
121 Hz	4.8×10^{-5}	176 Hz	6.9×10^{-3}	121 Hz	4.8×10^{-3}

Table A.9: Thermoelastic loss contribution of Ti-6Al-4V SHS for HV2 samples under load

Silicon		Sapphire		Suspension tube	
f_{SA}	$\phi_{\text{therm,SHS}}$	f_{SA}	$\phi_{\text{therm,SHS}}$	f_{SA}	$\phi_{\text{therm,SHS}}$
10 kg					
57 Hz	4.2×10^{-3}	81 Hz	5.9×10^{-3}	62 Hz	4.5×10^{-3}
149 Hz	1.1×10^{-3}	213 Hz	1.6×10^{-2}	160 Hz	1.2×10^{-2}
100 kg					
73 Hz	2.9×10^{-2}	87 Hz	3.5×10^{-2}	99 Hz	3.9×10^{-2}
243 Hz	6.7×10^{-2}	223 Hz	8.4×10^{-3}	221 Hz	8.3×10^{-2}
400 kg					
81 Hz	1.4×10^{-1}	109 Hz	1.3×10^{-1}	170 Hz	1.7×10^{-1}
213 Hz	1.7×10^{-1}	258 Hz	1.7×10^{-1}	352 Hz	1.6×10^{-1}

Table A.10: Thermoelastic loss contribution of SHS of the case, where the cage is attached to the SH

	$f_{SA,1} = 11 \text{ Hz}$	$f_{SA,2} = 41 \text{ Hz}$	$f_{SA,3} = 121 \text{ Hz}$
$\phi_{\text{therm,SHS}}$	9.3×10^{-4}	4.3×10^{-3}	1.1×10^{-2}

Table A.11: Thermoelastic loss contribution of SST SHS for remodelled case of [8]

	$f_{SA,1} = 91 \text{ Hz}$	$f_{SA,2} = 1211 \text{ Hz}$	$f_{SA,3} = 3581 \text{ Hz}$
$\phi_{\text{therm,SHS}}$	2.0×10^{-1}	1.8	1.4

Table A.12: Natural frequencies of the Phase two suspension tubes.

SA Mode Number	Frequency / Hz
$f_{SA,1}$ Mode	9
$f_{SA,2}$ Mode	54
$f_{SA,3}$ Mode	150

Table A.13: Phase-II SH dimensions

Component	Dimension / mm
d_{SH}	200
h_{SH}	100
$d_{\text{insert,OT}}$	100
$h_{\text{insert,OT}}$	15
d_{SI}	90
h_{SI}	20
$d_{\text{insert,IT}}$	70
$h_{\text{insert,IT}}$	14
d_{RI}	60
h_{RI}	20
d_{cone}	10
h_{cone}	20

Table A.14: Thermoelastic loss contribution of Ti-6Al-4V for measurements conducted in phase II

	$f_{SA,1} = 9 \text{ Hz}$	$f_{SA,2} = 54 \text{ Hz}$	$f_{SA,3} = 150 \text{ Hz}$
$\phi_{\text{therm,SHS}}$	3.0×10^{-4}	2.1×10^{-3}	5.8×10^{-3}

A.3 Additional figures

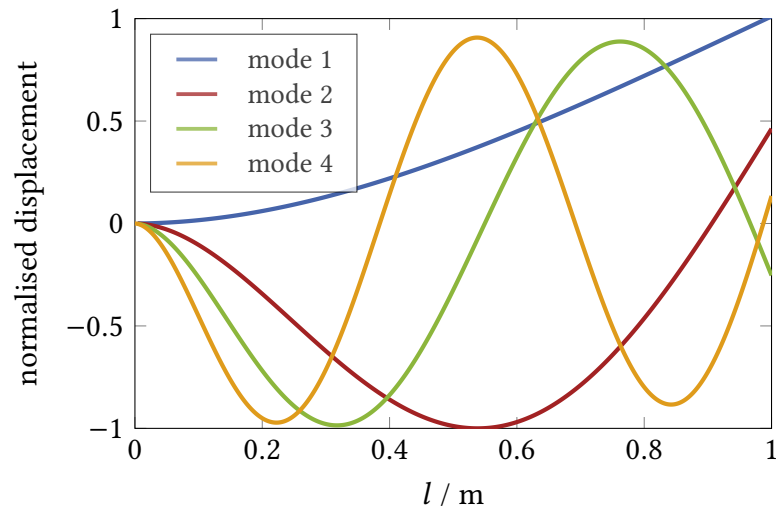


Figure A.1: Mode shapes of the first three modes of the sample with Head Variant 2

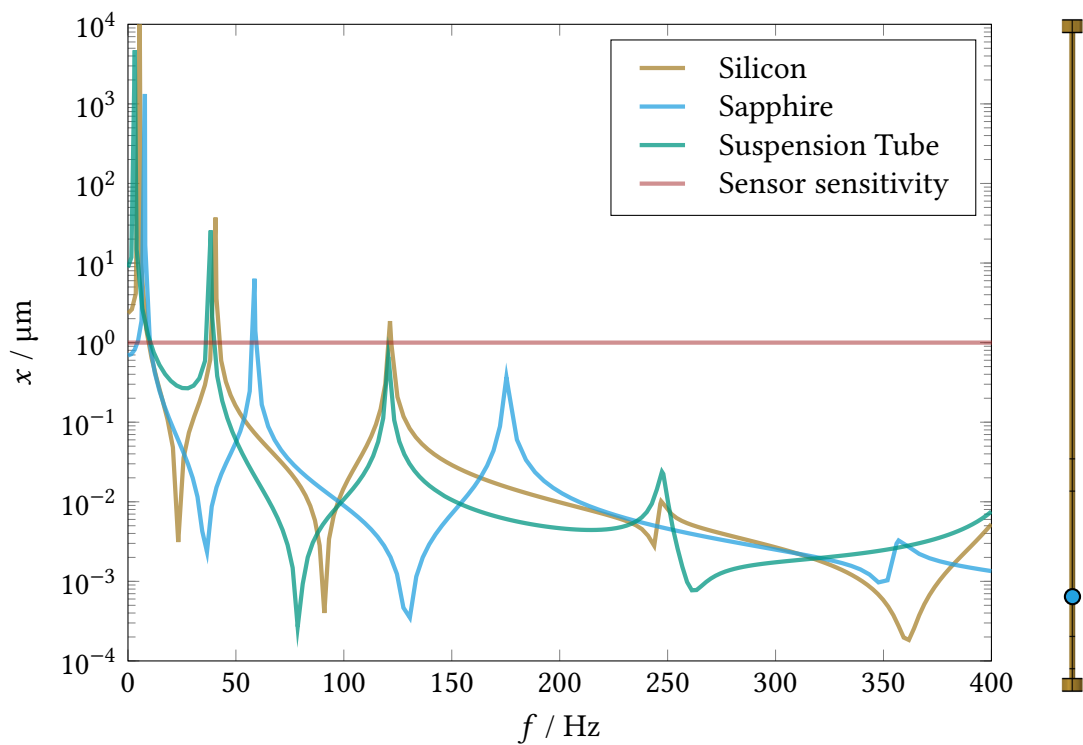


Figure A.2: Frequency response amplitude of Sapphire and Silicon sample Head Variant 2

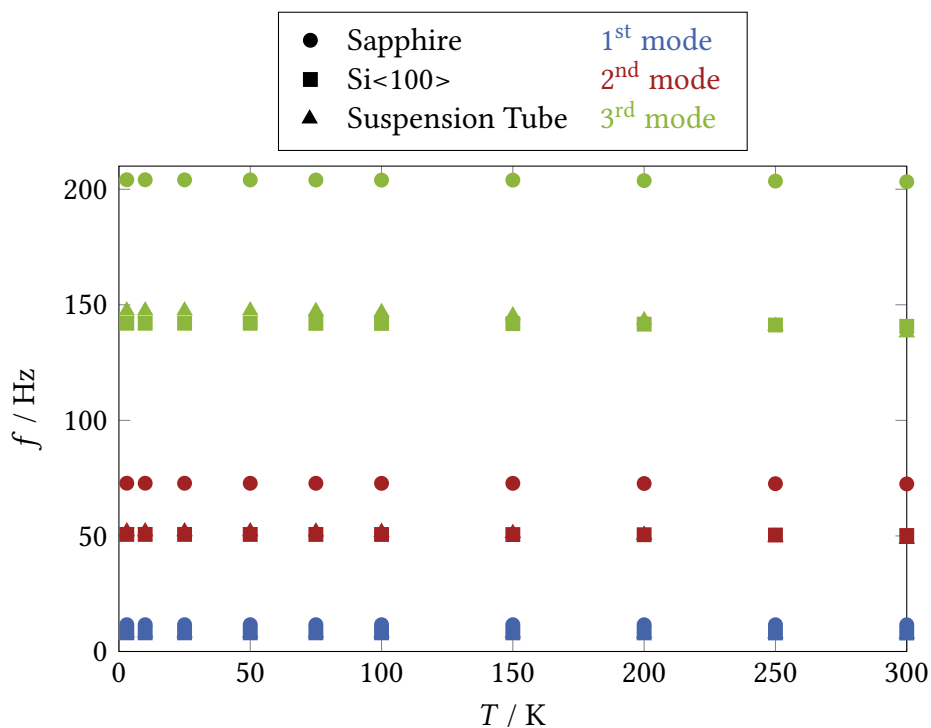


Figure A.3: Temperature dependency of Samples HV1,

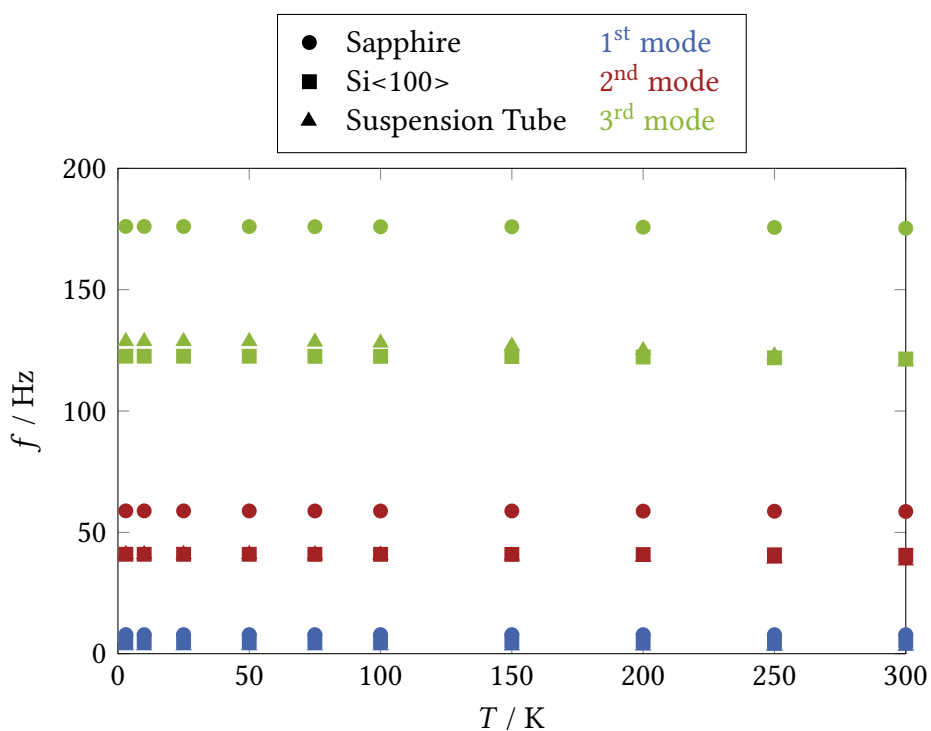


Figure A.4: Temperature dependency of Samples HV2

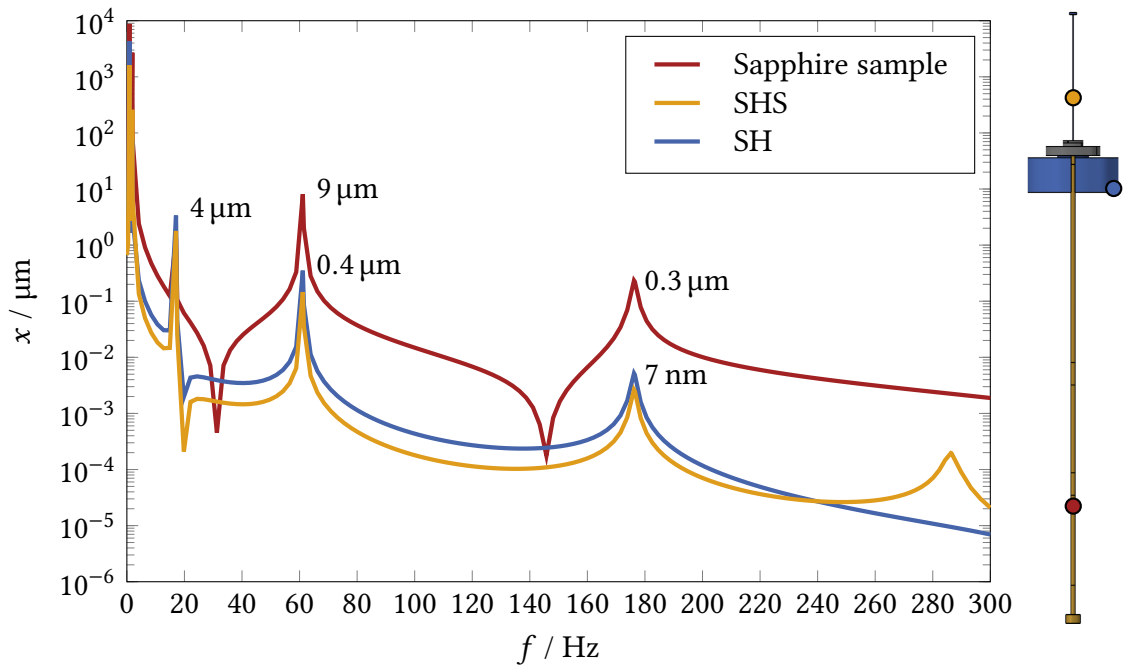


Figure A.5: FRA of sample and SUS: Sapphire HV2

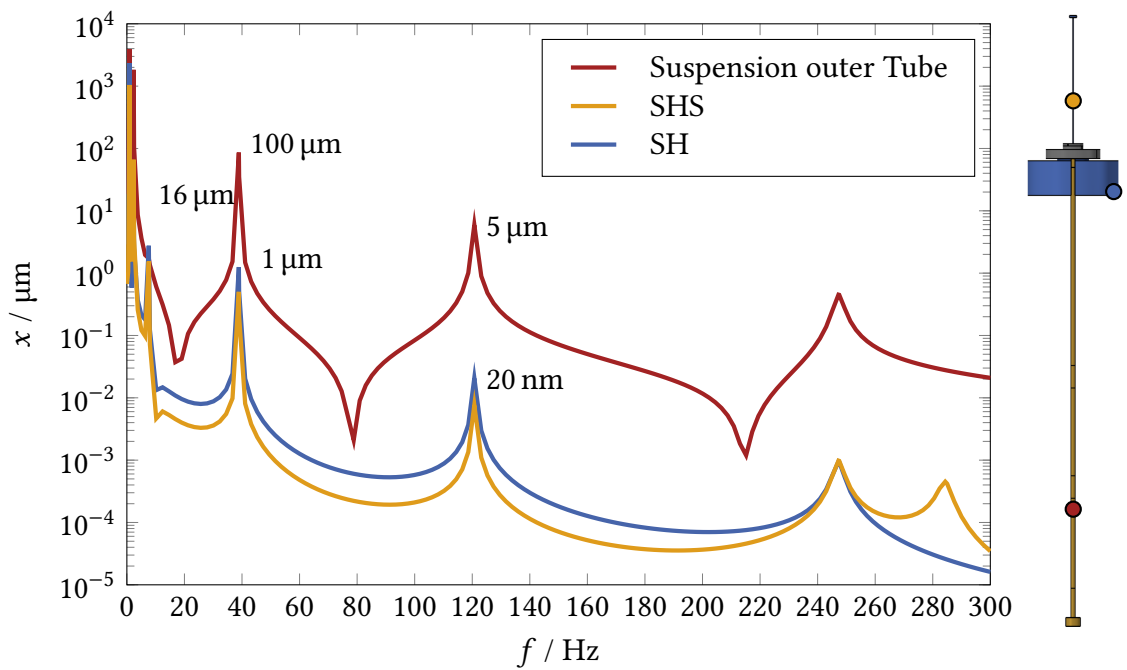


Figure A.6: FRA of sample and SUS: Suspension Tube HV2

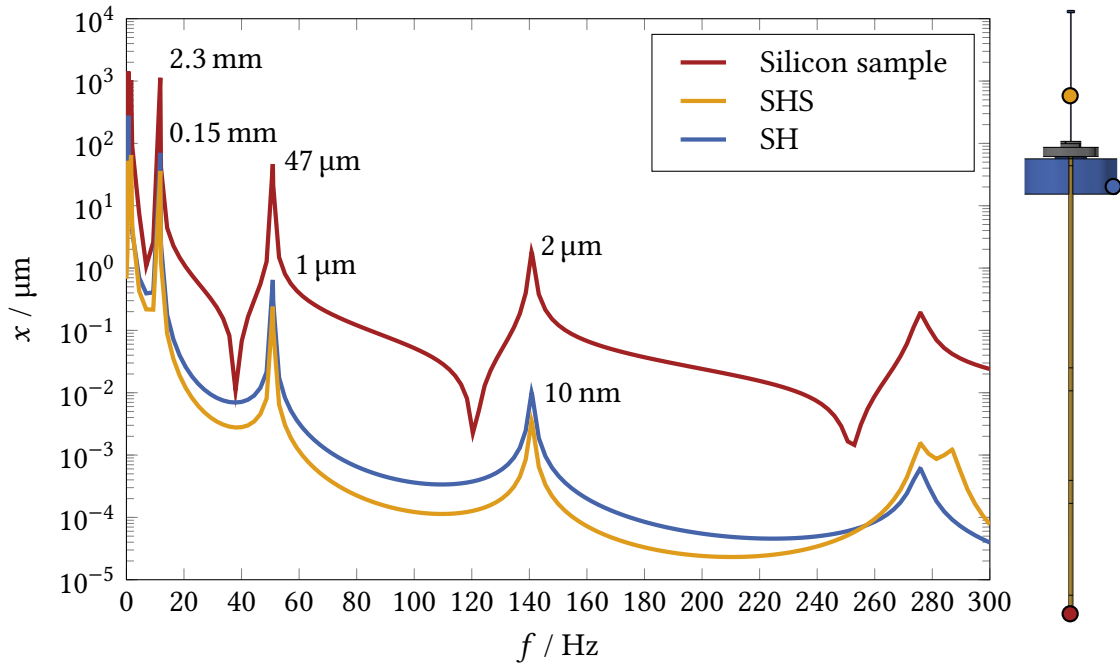


Figure A.7: FRA of sample and SUS: Silicon HV1

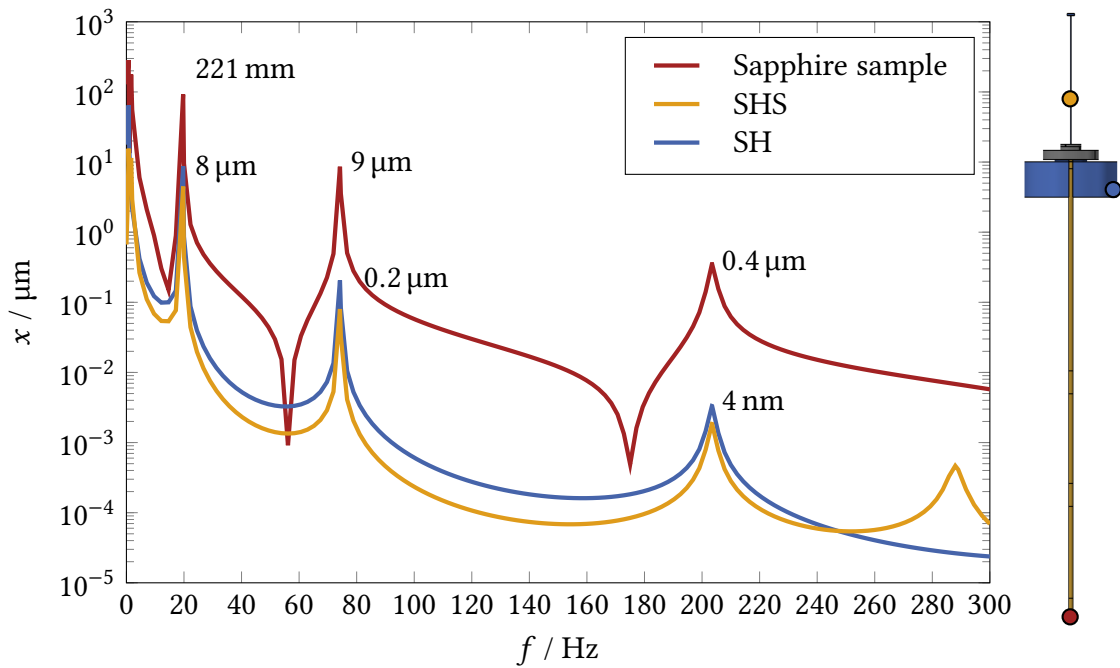


Figure A.8: FRA of sample and SUS: Sapphire HV1

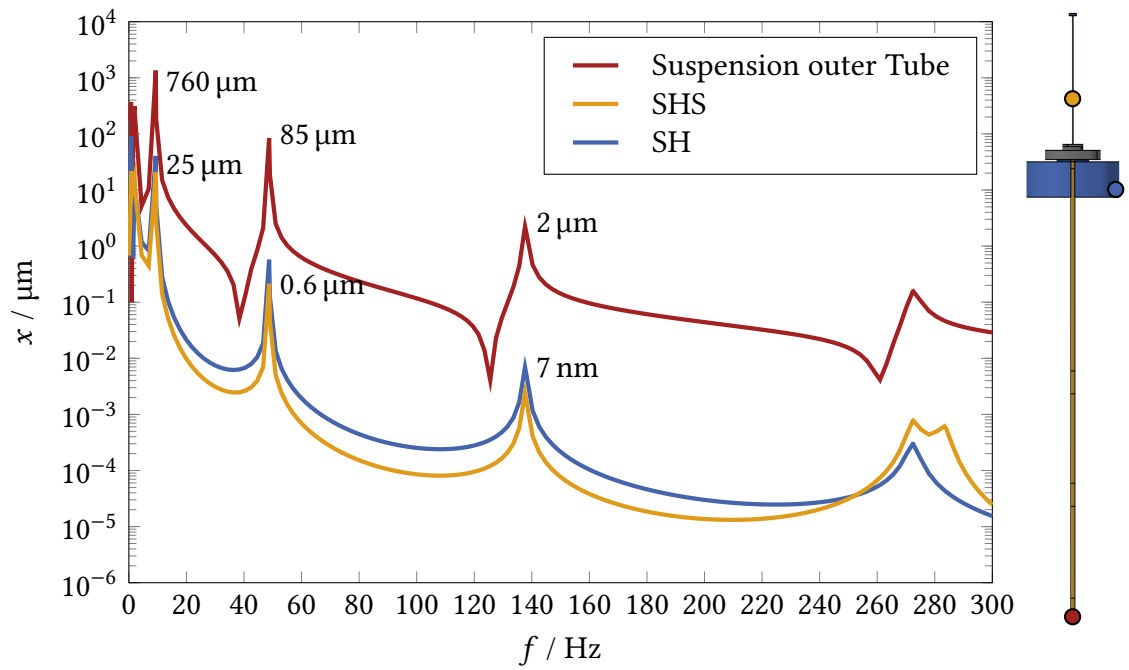


Figure A.9: FRA of sample and SUS: Suspension Tube HV1

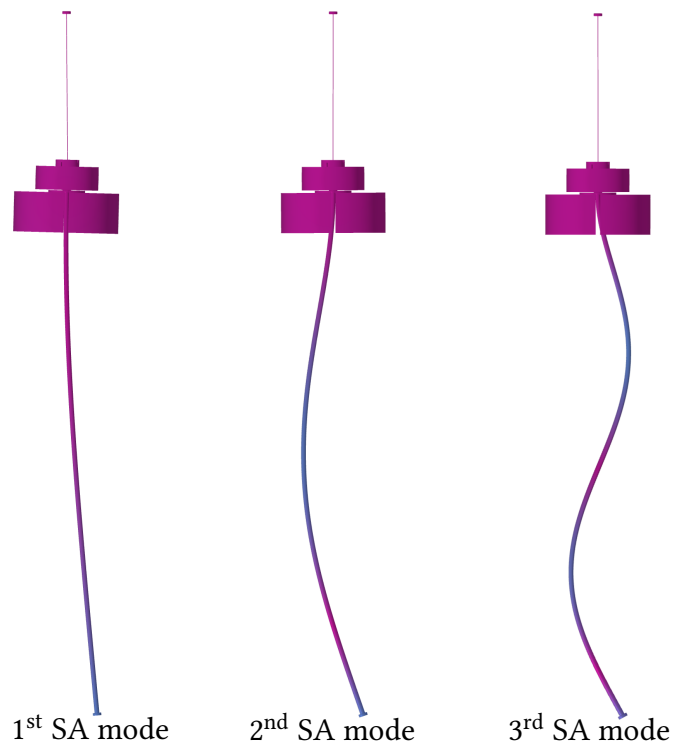


Figure A.10: Resonance shapes of the first three Sa modes (HV1)

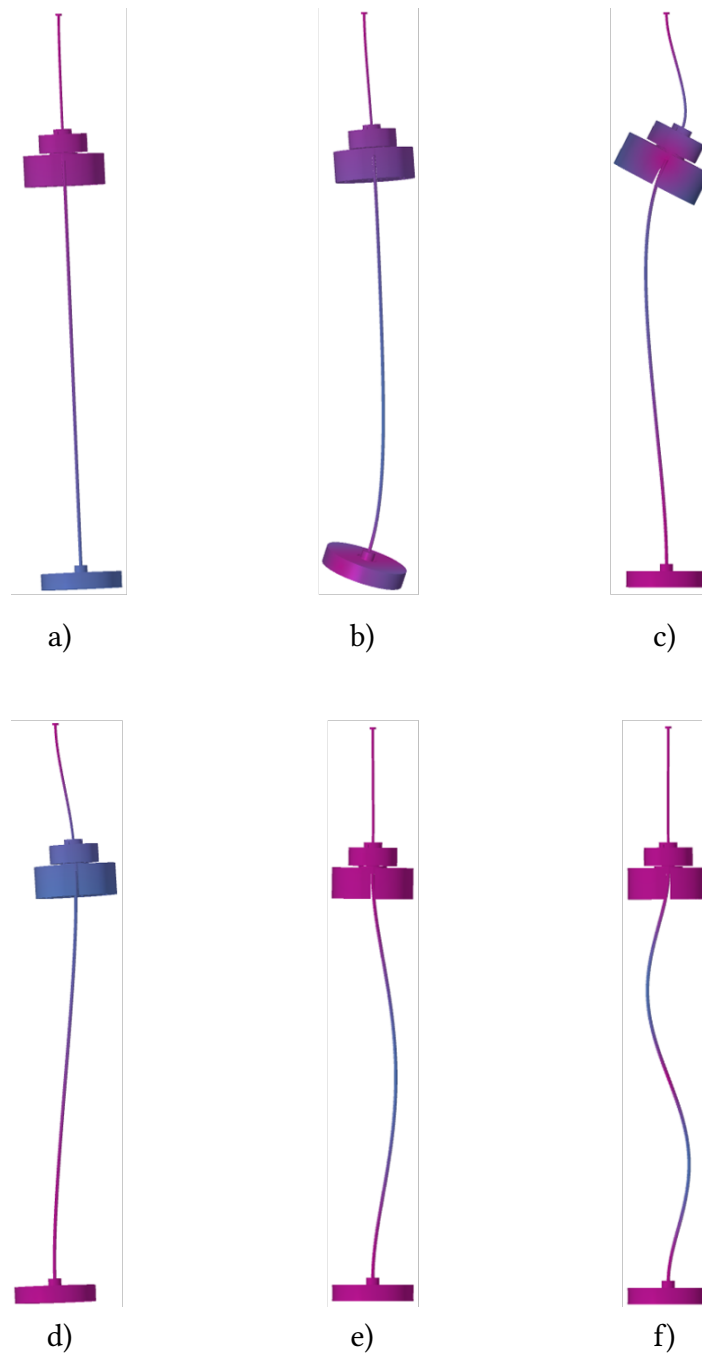


Figure A.11: Two stage pendulum characteristic mode shapes, a) system pendulum mode, b) suspended mass rocking mode, c) SH rocking mode, d) SH pendulum mode, e) 1st SA violin mode, f) 2nd SA violin mode

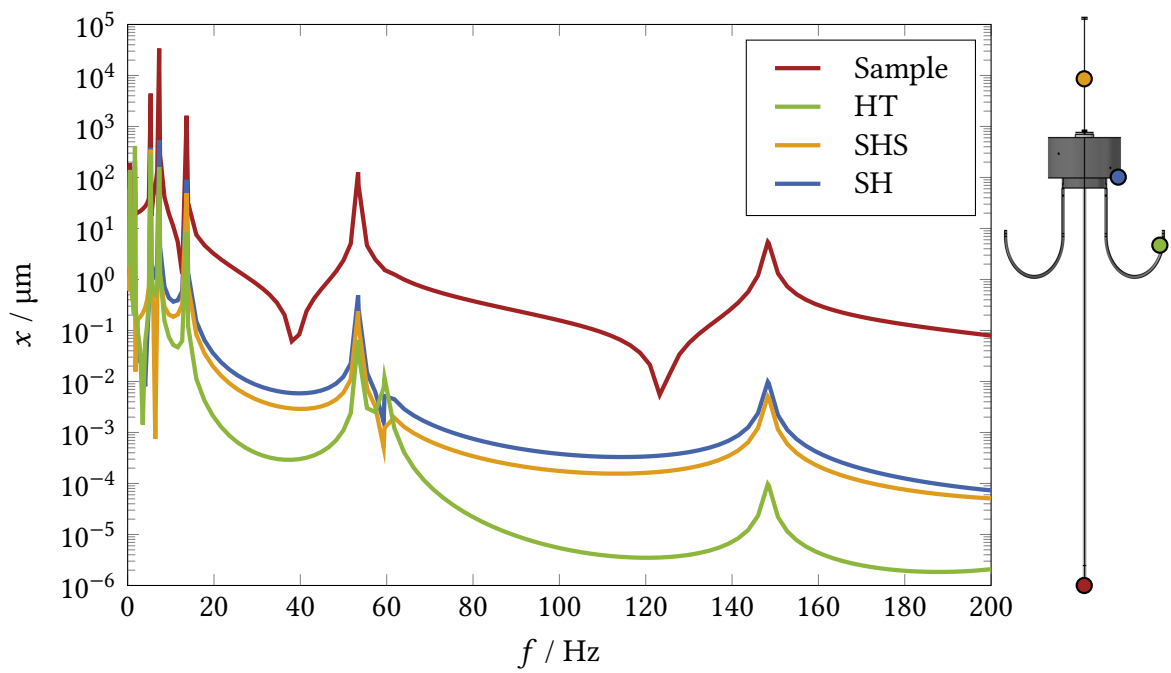


Figure A.12: FRA of set up design utilising He-tubes variant 2